EFFECTS OF SPECIMEN GEOMETRY AND COATING ON THE THERMO-MECHANICAL FATIGUE OF PWA 1484 SUPERALLOY

A Thesis
Presented to
The Academic Faculty

by

Matthew Daniel O'Rourke

In Partial Fulfillment
of the Requirements for the Degree
Master of Science in the
George W. Woodruff School of Mechanical Engineering

Georgia Institute of Technology

August, 2013

Copyright © 2013 by Matthew Daniel O'Rourke

EFFECTS OF SPECIMEN GEOMETRY AND COATING ON THE THERMO-MECHANICAL FATIGUE OF PWA 1484 SUPERALLOY

Approved by:

Dr. Stephen D. Antolovich, Advisor
School of Materials Science and Engineering,
George W. Woodruff School of Mechanical Engineering
Georgia Institute of Technology

Dr. Richard W. Neu
George W. Woodruff School of Mechanical Engineering,
School of Materials Science and Engineering
Georgia Institute of Technology

Dr. W. Steven Johnson
School of Materials Science and Engineering,
George W. Woodruff School of Mechanical Engineering
Georgia Institute of Technology

Date Approved: June 26, 2013

ACKNOWLEDGEMENTS

I wish to thank Dr. Steve Antolovich for his extensive guidance throughout the duration of this project, as well Dr. Rick Neu for his continual technical insight. I am also thankful to Dr. Steve Johnson for being a part of my reading committee and for his mentorship throughout my time as a graduate student. I have learned a great deal more than I expected from both classes and research due to all of their knowledge and experience.

I am also grateful for the supervision and insight provided by people at Pratt & Whitney, including Shawn Gregg, Dr. Alexander Staroselsky, and Keith Kersey, among others. In addition, without the financial support of Pratt & Whitney, this project would not have been possible.

I would also like to thank JD Huggins for his considerable assistance in keeping things working in the laboratory and with assorted tasks to keep my research flowing, in addition to Rick Brown for sharing his knowledge of the Mechanical Properties Research Laboratory. Machining help provided by Steven Sheffield and Louis Boulanger of the ME Machine Shop is also much appreciated.

The assistance provided by fellow graduate students Ben Adair, Mike Hirsch, Mike Kirka, and Matt Siopis has been enormous, and I am much indebted to them. Finally, I am extremely grateful to my family and friends, whose encouragement and support has been essential to help me though my graduate studies.

TABLE OF CONTENTS

LIST OF TABLES

Page

LIST OF FIGURES

Page

LIST OF SYMBOLS

A ..... Area of Grip Piston

C_R ..... Constant Value for Round Specimens

D ..... Specimen Diameter

$\Delta\varepsilon_{mech}$ ..... Mechanical Strain Range

δ_p ..... Decrease in Plug Radius

δ_r ..... Radial Interference

E ..... Elastic Modulus

E_p ..... Elastic Modulus of Plug

E_s ..... Elastic Modulus of Specimen

ε_{mech} ..... Mechanical Strain

$(\varepsilon_{mech})_{max}$ ..... Maximum Mechanical Strain

$(\varepsilon_{mech})_{min}$ ..... Minimum Mechanical Strain

ε_{th} ..... Thermal Strain

F_c ..... Clamping Force

φ ..... Phase Shift

L ..... Applied Axial Load

$\mu_{g\text{-}c}$ ..... Coefficient of Friction Between Grip and Collet

N_f ..... Cycles to Failure (Specimen Separation or Test Stoppage)

N_i ..... Cycles to Crack Initiation (1% Load Drop)

v ..... Poisson's Ratio

v_p ..... Poisson's Ratio of Plug

v_s ..... Poisson's Ratio of Specimen

P ..... Grip Supply Pressure

P_1 ..... Ideal Gas Pressure at State 1

P_2 ..... Ideal Gas Pressure at State 2

p ..... Contact Pressure from Shrink Fit

p_i ..... Internal Pressure

p_o ..... External Pressure

R_t ..... Nominal Transition Radius

R ..... R-Ratio

r ..... Radial Location within Specimen

r_i ..... Inner Radius of Specimen

r_o ..... Outer Radius of Specimen

r_p ..... Plug Radius

σ_1 ..... Principal Stress in Direction 1

σ_2 ..... Principal Stress in Direction 2

σ_3 ..... Principal Stress in Direction 3

σ_a ..... Alternating Stress

σ_c ..... Hoop Stress

σ_m ..... Mean Stress

σ_{max} ..... Maximum Stress

σ_{min} ..... Minimum Stress

σ_{VM} ..... Von Mises Stress

T ..... Applied Torque

T_1 ..... Ideal Gas Temperature at State 1

T_2 ..... Ideal Gas Temperature at State 2

T_{max} ..... Maximum Cyclic Temperature

T_{min} ..... Minimum Cyclic Temperature

LIST OF ABBREVIATIONS

BiF.....Bithermal Fatigue

FCC.....Face-Centered Cubic

FEA.....Finite Element Analysis

Georgia Tech.....Georgia Institute of Technology

HCF.....High-Cycle Fatigue

ID.....Inner Diameter

IP.....In-Phase

LCF.....Low-Cycle Fatigue

MPRL.....Mechanical Properties Research Laboratory

OP.....Out-of-Phase

PID.....Proportional-Integral-Derivative

SEM.....Scanning Electron Microscope

TC.....Thermocouple

TCP.....Topologically Close-Packed

TET.....Turbine Entry Temperature

TMF.....Thermo-Mechanical Fatigue

SUMMARY

The single crystal superalloy PWA 1484 is used in hot section turbine blade applications due to its performance at high temperatures. In practice, the turbine blades are often coated in order to protect them from environmental degradation. However, under repeated cyclic loading, the coating may serve as a site for crack initiation in the blades. Fundamental out-of-phase (OP) thermo-mechanical fatigue (TMF) studies, primarily using uncoated solid cylindrical test samples, have previously examined both crack initiation and propagation in PWA 1484. In this work, mechanical strain-controlled OP TMF tests were performed on coated and uncoated specimens of a hollow cylindrical geometry in order to study the effects of both geometry and coating on the TMF crack initiation behavior. To accomplish this, it was necessary to create and analyze a modified gripping mechanism due to the unique geometry of the test samples, and as predicted by hand calculations and finite element analysis, these modifications proved to be successful. The TMF test results for the uncoated material were compared to those from previous studies under the same testing conditions, and it was found that the differences in geometry had a minimal impact on fatigue life. Comparisons of the results for the coated and uncoated material suggested that the coating may have offered a slight improvement in life, although insufficient results were available to determine whether these differences were statistically significant. Damage mechanisms resulting from different test conditions were also observed through microscopy on failed specimens.

CHAPTER 1

INTRODUCTION

1.1: Motivation

Components of hot section gas turbine engines constantly undergo cycling of temperatures and mechanical loads. These cycles are caused by engine start-up, shut-down, vibrations, or changes in engine load demands, with additional loads induced by thermal gradients [1]. The concurrent and repeated thermal and mechanical cycling leading to material degradation in such applications is referred to as thermo-mechanical fatigue (TMF).

As engine performance has been increased, so too have temperatures in the turbines and therefore the requirements of the high temperature materials used for the components. Through the years, nickel-based superalloys have become the materials of choice for turbine discs and blades due to their superior ability to maintain their mechanical properties at temperatures near their melting points. Improvements in manufacturing methods have led to the production of conventionally cast, directionally solidified and then single-crystal superalloys, each leading to improved material performance [1]. However, directionally solidified and single-crystal materials exhibit extreme anisotropy [2]. Since the turbine blades experience the highest temperatures, single crystals are now used for these applications because the elimination of grain boundaries greatly reduced creep and environmental attack.

In practice, some type of coating is usually applied to the surface of turbine blades before they are put to use in gas turbine engines to protect them from environmental

attack. Without the coating, the alloy would not be able to survive the temperature demand placed on them by the current engine technology. However, the coatings are brittle and cracking may occur easily, and the cracks may propagate into the base metal [3]. Although many TMF tests have shown uncoated specimens to have a longer life than coated specimens under the same conditions, the coating is usually necessary to protect the alloys during operating conditions [4, 5].

Fundamental studies already have been conducted on the material behavior of PWA 1484, investigating low- and high-cycle fatigue, TMF, creep, and oxidation, as well as the microstructural effects of crystal orientation and dendrite spacing [2, 6-13]. In addition, a model is needed to accurately predict the service life of turbine components made of PWA 1484. Such a model would not only lead to increased safety but also reduce scheduled maintenance costs. Previous TMF testing was performed in the Mechanical Properties Research Laboratory (MPRL) at the Georgia Institute of Technology (Georgia Tech), and extensive work has been performed to create life prediction models based the work of Amaro and colleagues [14-19]. However, the validity of this model has been questioned due to life discrepancies between testing performed at Georgia Tech and Pratt & Whitney. There were several differences in the conditions of the tests, though; not only were the specimen geometries different, but so were the temperatures, cycle time, and waveform used for the testing. A summary of the differences in the TMF cycles can be found in Table 1.1. The reasons for the life discrepancies must be explored in order to validate the life model that has been created, starting with the specimen geometry.

Table 1.1: Georgia Tech and Pratt & Whitney TMF Cycle Comparison

	Georgia Tech	**Pratt & Whitney**
Minimum Temperature (°C)	550	427
Maximum Temperature (°C)	1050	1038
Cycle Time (sec)	180	60
Waveform	ramp	sine

1.2: Research Objectives

The primary objectives of this research were to determine the differences in TMF test results that may be caused by specimen geometry and to explore the influence of a coating on the life and damage mechanisms. It was also desired to show that test results obtained in the MPRL at Georgia Tech could be reproduced with different specimen geometries. To accomplish this, TMF tests under mechanical strain control were performed on hollow specimens of PWA 1484 of the geometry used at Pratt & Whitney with and without a coating. First, a method of gripping the unique specimens in the test frame was formulated, analyzed, and produced to allow testing to proceed without damaging the specimens or affecting the results. Then, the actual TMF tests were performed, duplicating the test conditions previously used on solid cylindrical specimens at Georgia Tech. After analysis of the stress history results, the crack initiation lives of the hollow specimens were compared to those from the solid specimens as well as Pratt & Whitney data. Any trends between the two geometries were identified that may explain the discrepancies in results between Georgia Tech and Pratt & Whitney. Finally, with the aid of a scanning electron microscope, the differences in crack initiation lives and damage mechanisms between the coated and uncoated specimens were compared.

1.3: Thesis Overview

The second chapter of this thesis provides relevant background information and a literature review of thermo-mechanical fatigue, superalloys, and coatings. Information is presented about the types of superalloys, their microstructures and compositions, material properties, their performance and behavior under different aspects of TMF loading, and the effects of coatings. An overview of the influence of several TMF testing variables is also included. The third chapter presents the experimental methods, including the design and modification of the test specimens and gripping method, the testing equipment and procedure, and the governing standard employed to ensure test validity. The fourth chapter includes the results of hand calculations and finite element analysis influencing the design process of the modified gripping mechanism to ensure its success. The results of the TMF tests on the hollow specimens are also presented here, including load drop data as well as stress-strain histories. A discussion of the results, comparisons to previous Georgia Tech and Pratt & Whitney data, and possible reasons for the discrepancies are provided. The fifth chapter is composed of the conclusions from this research and recommendations for future work.

CHAPTER 2

BACKGROUND

2.1: Thermo-Mechanical Fatigue

Fatigue is the damage caused to a material or structure due to the application of cyclic loading. Fatigue damage occurs in three stages: crack initiation or nucleation, crack propagation, and fracture [20]. An example of fatigue loading under force control can be found in Figure 2.1. In this case, σ_m refers to the mean stress, and σ_a refers to the alternating stress or stress amplitude, while σ_{max} and σ_{min} are the maximum and minimum cyclic stresses, respectively. The *R*-ratio (or stress ratio, in this case) is defined as the ratio of the minimum applied stress to the maximum applied stress. Fully-reversed fatigue, meaning that $\sigma_{min} = -\sigma_{max}$, corresponds to $R = -1$.

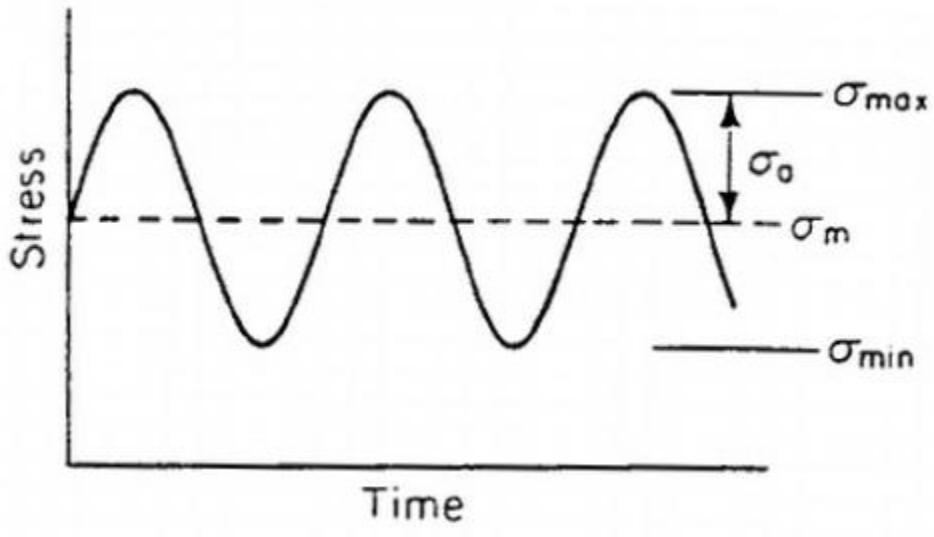

Figure 2.1: Plot Presenting the Terminology for Cyclic Loading [20]

In real world applications, fatigue initiation always occurs at sites of stress concentration, including casting pores or machining marks [1]. At high load levels that would result in low-cycle fatigue (LCF), fatigue is best modeled using a strain-life approach (with tests performed under strain control) as opposed to stress-life. Strain-life methods simulate fatigue at a notch tip in a component, and the results are considered fatigue initiation life estimates [20]. Basquin [21] discovered that stress-life data could be plotted linearly in log-log coordinates. Later and independently, Coffin [22] and Manson [23] each found that plastic strain vs. fatigue life is also linear on a log-log scale. Plastic strain is very important since it is the driver of damage and the deformation mode experienced at crack tips and sharp notches.

During thermo-mechanical fatigue (TMF), materials experience changing mechanical loads and temperatures simultaneously. Therefore, the total strain induced in the material can be separated into two distinct parts. The thermal strain, ε_{th}, results from a temperature change and depends on the material's coefficient of thermal expansion [24]. The mechanical strain, ε_{mech}, results purely from mechanical loading. TMF tests are most commonly conducted under mechanical strain control; for this situation, the *R*-ratio (or mechanical strain ratio, in this case) is defined below in Equation 2.1.

$$R = \frac{\left(\varepsilon_{mech}\right)_{min}}{\left(\varepsilon_{mech}\right)_{max}} \tag{2.1}$$

The phase angle φ refers to the phase shift between the thermal and mechanical cycles during TMF. Two specific cases are in-phase (IP) and out-of-phase (OP) TMF. Figure 2.2 shows an example of an IP TMF waveform, in which φ = 0°, and the maximum mechanical load occurs at the maximum temperature and vice versa. An

example of an OP TMF waveform is shown in Figure 2.3, where $\varphi = 180°$. In this case, the minimum mechanical load occurs at the maximum temperature and vice versa.

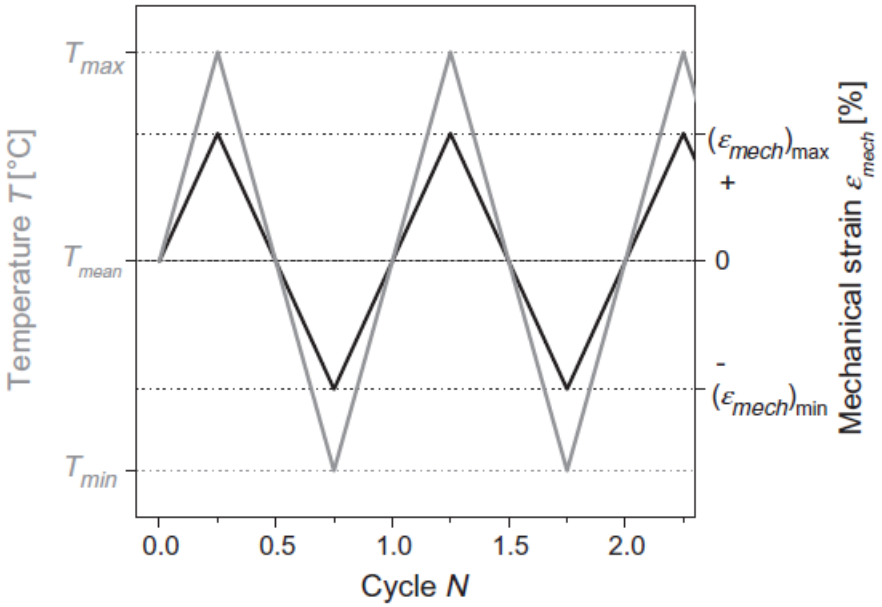

Figure 2.2: In-Phase Thermal-Mechanical Cycling [25]

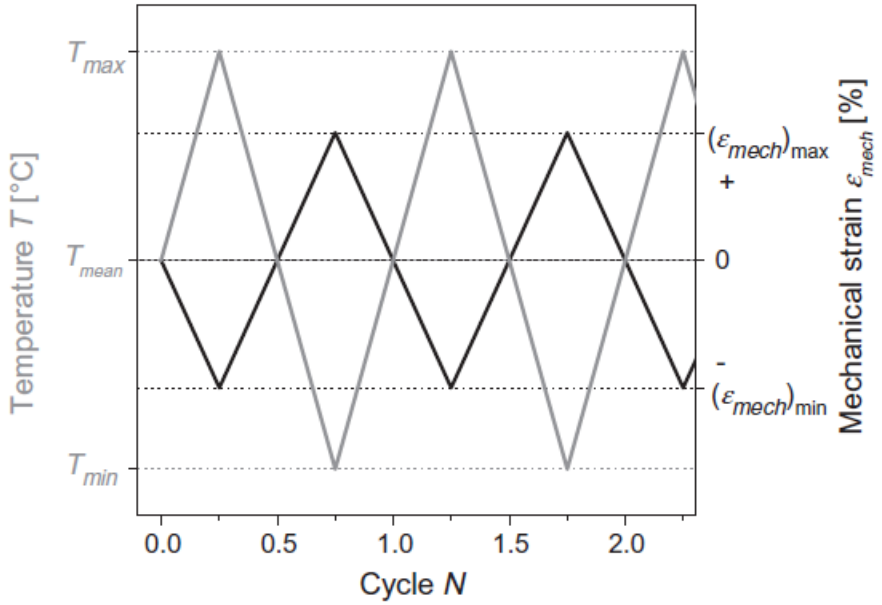

Figure 2.3: Out-of-Phase Thermal-Mechanical Cycling [25]

In addition to these waveforms, bithermal fatigue (BiF) tests are also occasionally performed [15, 26-28]. In these tests, all of the mechanical loading only occurs when the temperature is constant at either the minimum or maximum. Therefore, the interactions that may be introduced from concurrently changing load and temperature are eliminated. These tests were designed to bridge the gap between isothermal fatigue and the common TMF waveform while isolating the damage mechanisms that occur [27]. An example of an OP BiF waveform is shown in Figure 2.4.

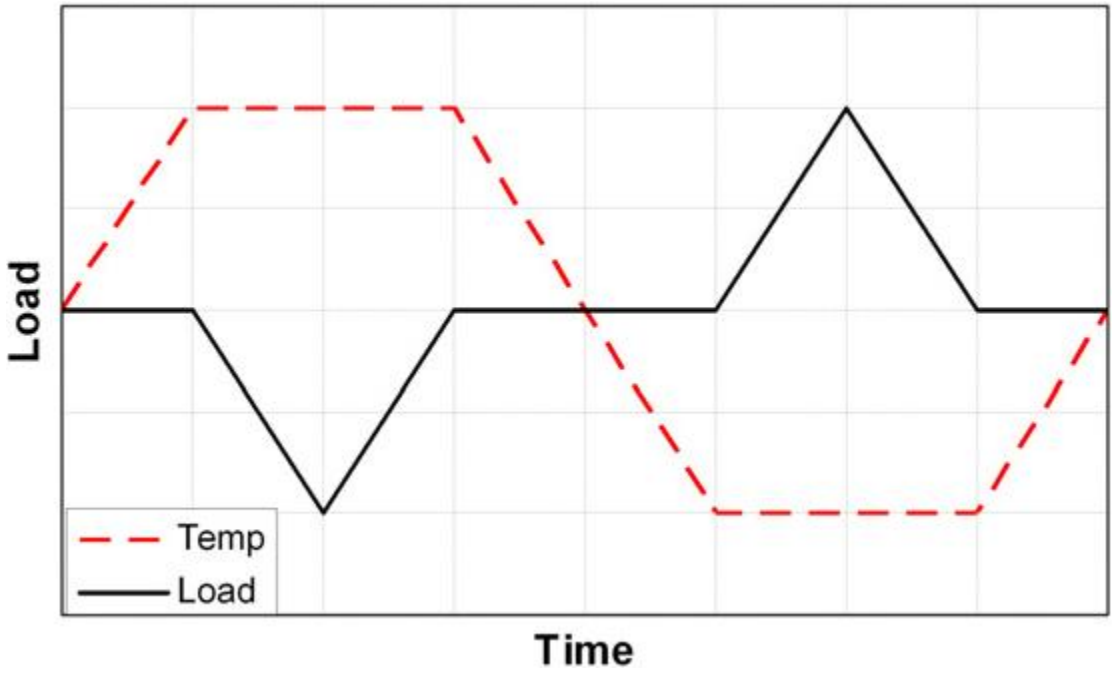

Figure 2.4: Out-of-Phase Bithermal Fatigue Waveform [15]

2.2: Superalloys

2.2.1: Introduction and History

High-temperature materials are used for applications such as turbines, rockets, and heat exchangers due to their ability to maintain their properties at elevated temperatures. This research focuses on those used in gas turbine engines. Two types of turbine-powered jet engines are displayed below. Figure 2.5 shows a turbojet engine. Air is compressed after the inlet, and then fuel is mixed with the air and combusted. The hot air passes through the turbine (which powers the compressor) and a nozzle before exiting as exhaust. A turbofan engine, as shown in Figure 2.6, operates in a similar manner, except a fan is included in the front that is also powered by the turbine. The fan accelerates a portion of the air that bypasses the gas generator portion of the engine before being exhausted by a nozzle. Regardless of the type of engine, the materials used for the turbine components must operate at high temperatures and experience both mechanical and thermal cyclic loading, resulting in TMF damage.

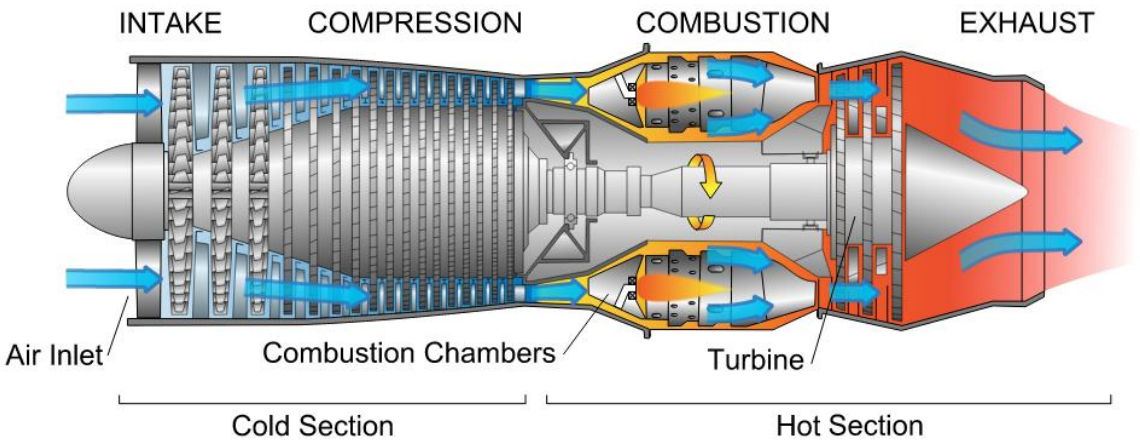

Figure 2.5: Schematic of a Turbojet Engine [29]

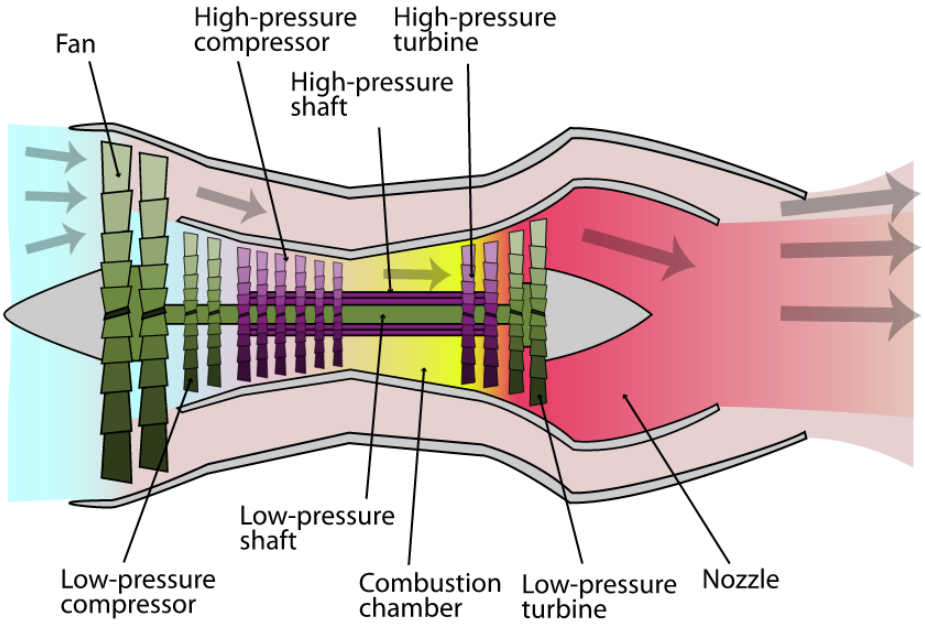

Figure 2.6: Schematic of a Turbofan Engine [29]

To this end, there are several desirable characteristics of high temperature materials [1]. First, they should be able to withstand loading at temperatures close to their melting point. A high temperature material is one that can operate at greater than 60% of its melting point (in absolute units). In addition, the material should have substantial resistance to long-term mechanical degradation. Resistance to creep deformation as well as static mechanical properties must be maintained over time. Finally, high-temperature materials must tolerate severe operating environments that have the possibility of resulting in corrosion, oxidation, or other forms of surface degradation.

Especially for operating temperatures over 800°C, as in gas turbines for jet propulsion, nickel-base superalloys have become an important material for their ability to fulfill all three of the above requirements. Nickel was chosen as the base element for these alloys for three main reasons. First, it has a stable face-centered cubic (FCC) lattice structure that does not undergo any phase changes between room temperature and its

melting point. An example of the FCC lattice structure is shown in Figure 2.7. Nickel is also a material with high ductility and toughness, so it is naturally resistant to fatigue and fracture. Finally, it has good creep resistance due to its low diffusion rate. Most of the chosen alloying elements were transition metals, meaning they are within the "d block" of the periodic table [30].

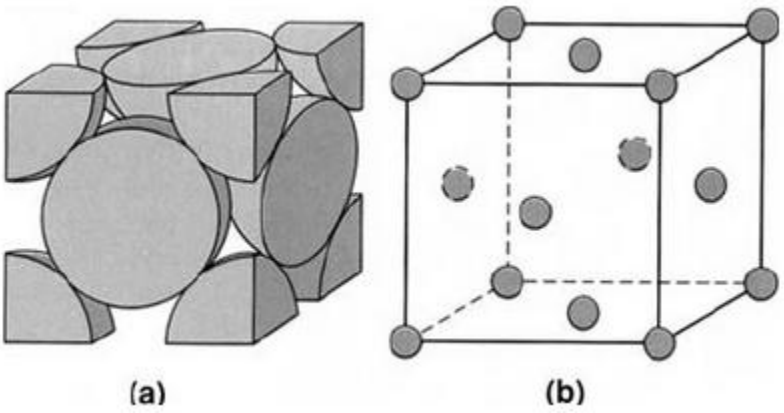

Figure 2.7: Unit Cell of the FCC Crystal Structure [1]

The performance of gas turbine engines can be greatly improved as the turbine entry temperature (TET) can be increased. As a result, the TET has become a central aspect of the design [31]. Figure 2.8 shows how the take-off TET of Rolls-Royce civil aeroengines has evolved over time, along with the material capabilities. The TETs for different families of engines are displayed as an asterisks. For civil aircraft, the TET varies during the flight, but it is greatest during take-off. Since the first engine was produced in 1940, the TET has been improved by 700°C [32]. This is due to the increased material capabilities, along with the cooling of turbine blades and the application of coatings.

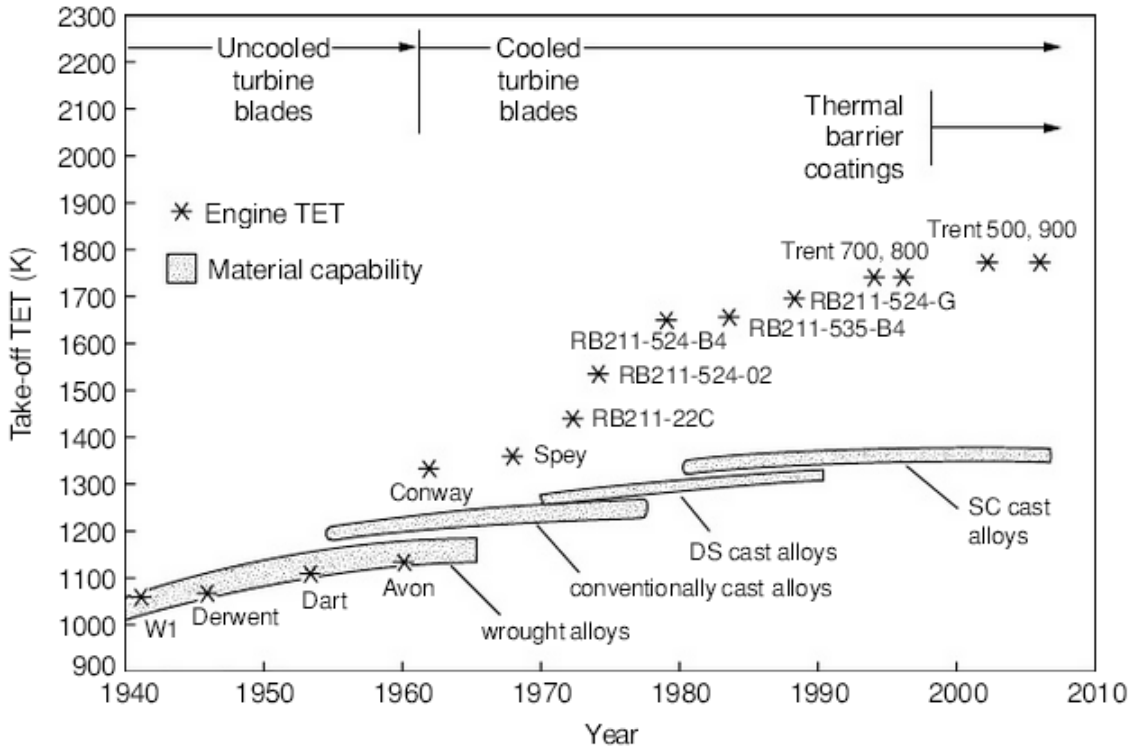

Figure 2.8: Evolution of the Turbine Entry Temperature Capability of Rolls-Royce's Aeroengines [32]

As the temperatures of gas turbine engines has increased over the years, so too has the capabilities of the superalloys comprising their components. Figure 2.9 shows how the creep performance of superalloys has evolved since the 1940s. The first turbine blades produced were wrought superalloys, and Nimonic alloys enabled the blade performance to be drastically improved [33]. The development of improved casing methods also led to better performance, followed by the introduction of directional solidification and then the production of monocrystalline, or single-crystal, superalloys. Although the performance of the superalloys of each production method gradually increased over time, the largest jumps in performance occurred with the introduction of an improved processing technique.

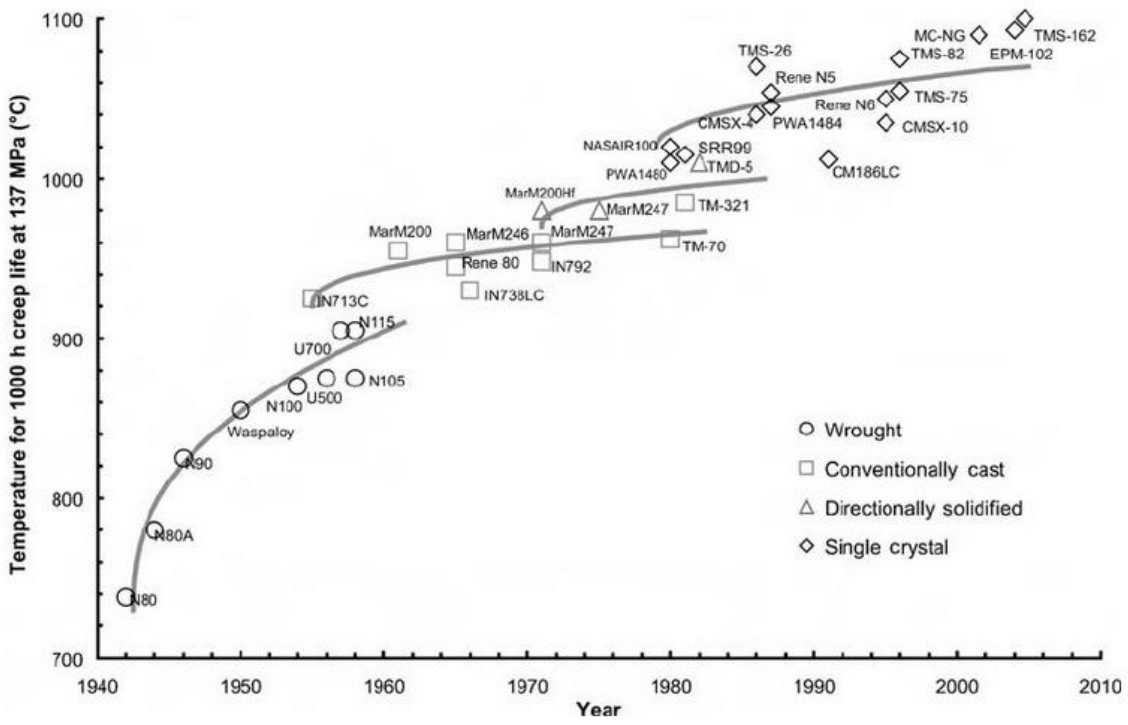

Figure 2.9: Evolution of the High-Temperature Capability of Superalloys [1]

Figure 2.10 depicts turbine blades in polycrystalline, directionally solidified, and single crystal forms. Conventionally cast superalloys would have the equiaxed crystal structure shown in Figure 2.10(a). With directional solidification, as shown in Figure 2.10(b), columnar structures were produced with the transverse grain boundaries mostly removed. Grain boundaries were eventually completely removed to produce single-crystal blades, as shown in Figure 2.10(c). With the monocrystalline material, grain-boundary strengthening elements such as boron and carbon were no longer necessary, so the blades could undergo better heat treatments, and the fatigue live was also improved.

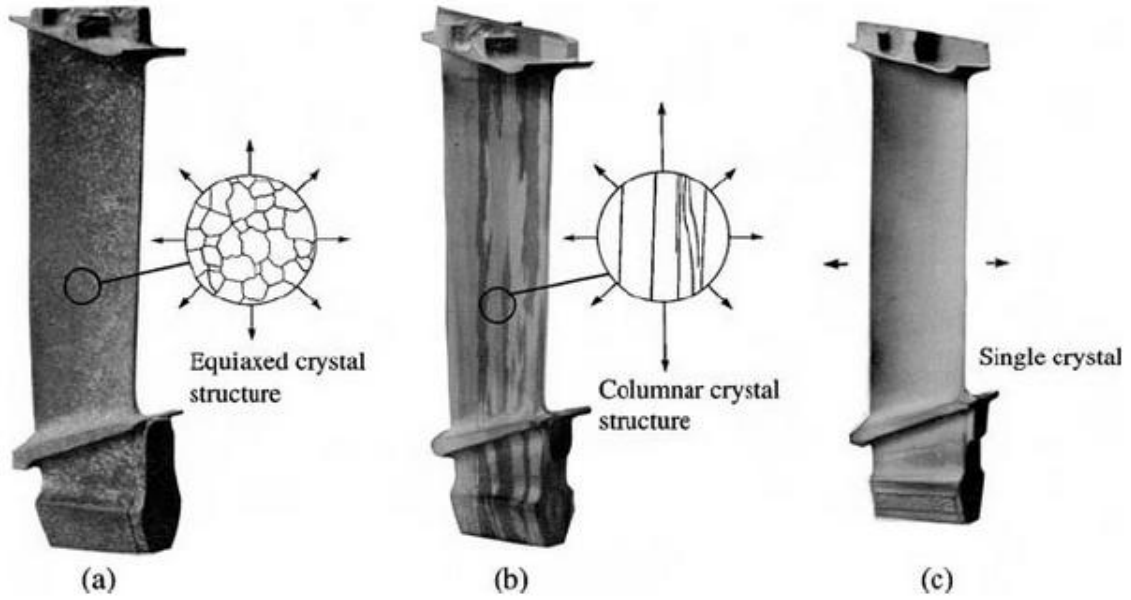

Figure 2.10: Turbine Blades in (a) Polycrystalline, (b) Directionally Solidified, and (c) Single Crystal Forms [34]

2.2.2: Microstructure and Composition

2.2.2.1: Microstructure

The microstructure of superalloys typically consists of three different phases. The gamma phase (γ) exhibits the FCC structure and forms a continuous matrix. This phase contains significant concentrations of cobalt, chromium, molybdenum, ruthenium, and rhenium. A gamma prime precipitate phase (γ') is coherent within the γ-matrix and contains elements like aluminum, titanium, and tantalum. In addition, superalloys contain carbides and borides, which generally reside on the γ-grain boundaries [35].

Figure 2.11(a) shows a section through the phase diagram of a Ni-Cr-Al alloy at 75% Ni (by atomic percentage). Experiments were performed by Beardmore *et al*. [36] using the alloys of varying composition represented by the dots on the phase diagram.

The resulting yield stress as a function of temperature of these alloys is shown in Figure 2.11(b). It was found that the yield stress of a two-phase γ + γ' alloy increases to a peak at about 800°C. Above this temperature, the yield stress obeys a rule of mixtures so that it corresponds to the weighted average of the values for each phase. However, at low temperatures, the actual yield strength of the two-phase alloy is much higher that what would be predicted by the rule of mixtures. Similar work by Piearcey *et al*. [37] with the directionally solidified alloy Mar-M200 produced similar results. A comparison to the behavior of a cube-oriented Ni_3Al alloy confirmed that the behavior of the alloy at and beyond the peak stress is driven by the strength of the γ' particles.

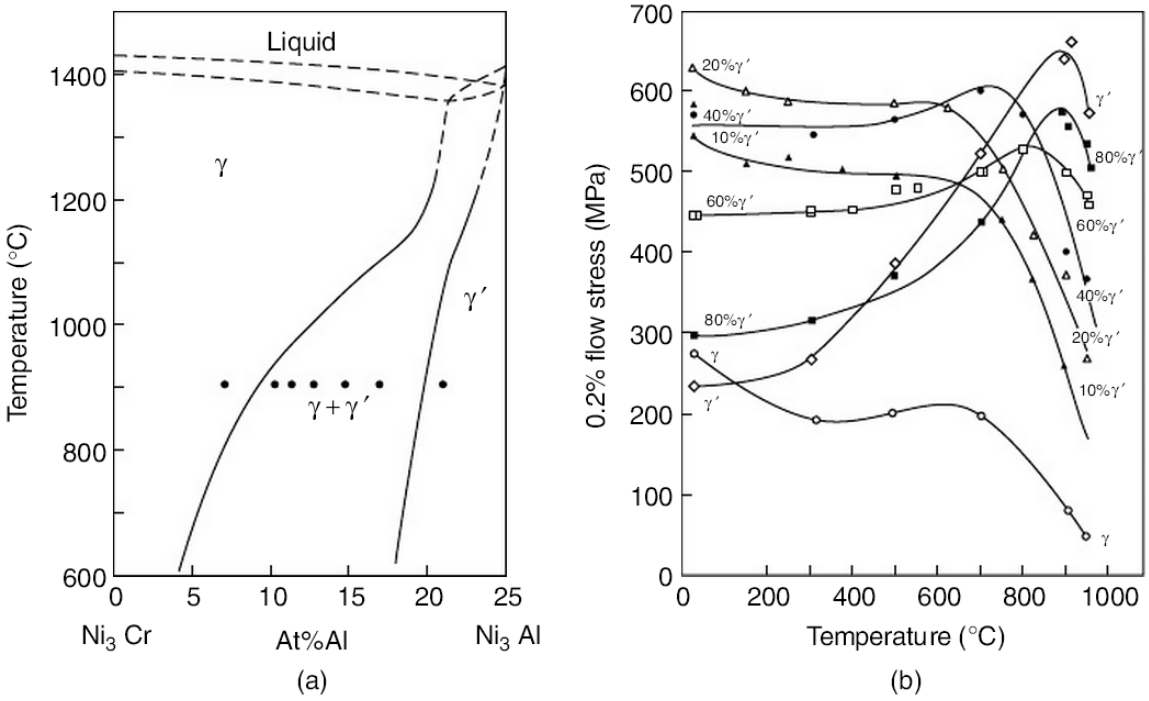

Figure 2.11: (a) Phase Diagram of a Ni-Cr-Al alloy at 75 at% Ni, and (b) Variation in Yield Stress with Temperature for the Alloys Produced [36]

Davies and Stoloff [38] explored this behavior at temperatures below the peak yield stress by examining Ni-Al alloys. The yield stress of several alloys with different compositions was determined at temperatures between -200°C and 800°C. The results are displayed in Figure 2.12. The Ni-8%Al alloy did not contain enough aluminum for γ' precipitation, so there were only minimal strengthening effects For the Ni-14%Al alloys, the heat treatment was found to have a significant effect on the strength due to its effects on the fraction, size, and distribution of the precipitates. The 700°C heat treatment resulted in large enough particles that were not spaced too far apart, resulting in a fairly constant yield stress across the range of temperatures because the deformation mode was microscopic deformation of the γ' particles.

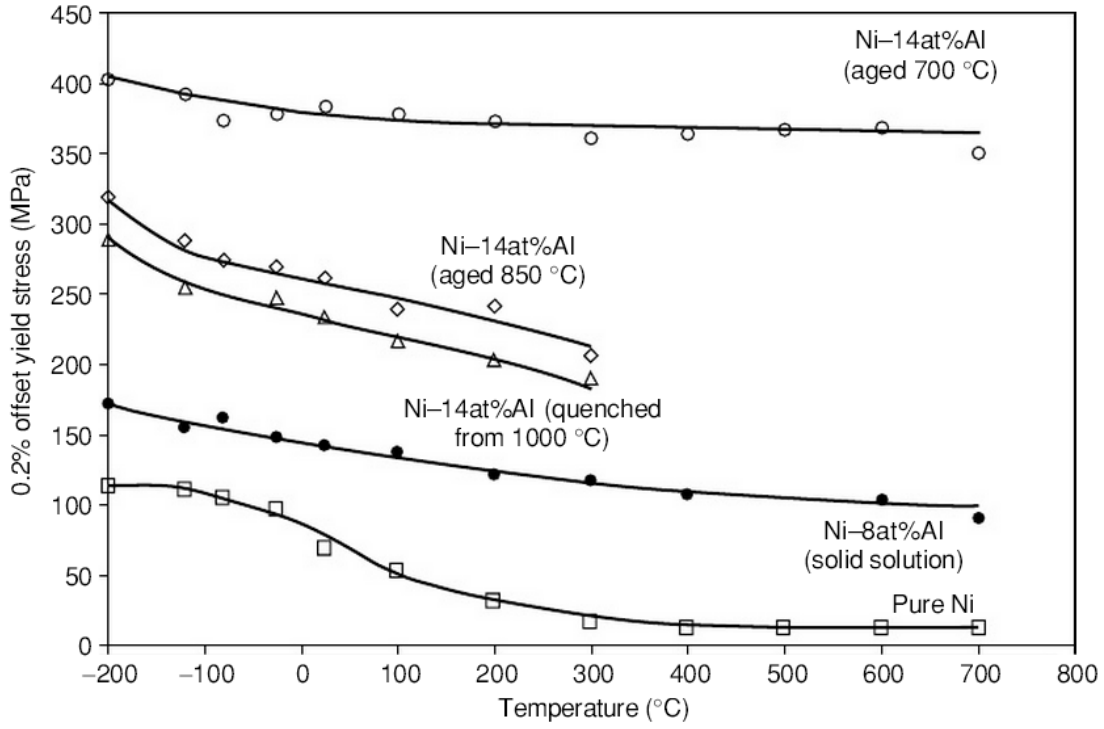

Figure 2.12: Yield Stress of Several Ni-Al Alloys as a Function of Composition and Temperature [38]

An image of the microstructure of PWA 1484 can be found in Figure 2.13. The rectangular Ni_3Al $L1_2$ γ' particles within the γ-phase matrix can clearly be distinguished, with a γ' volume fraction of approximately 60%. As depicted, the optimum microstructure consists of many fine γ' particles separated by only very thin layers of γ matrix.

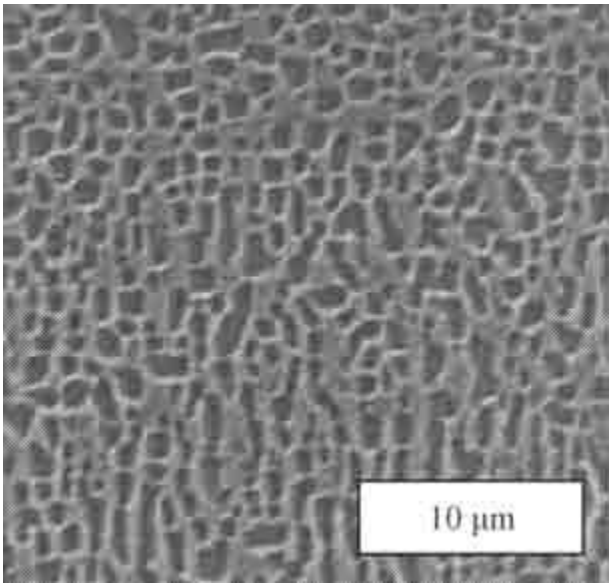

Figure 2.13: Image of the Gamma/Gamma Prime Microstructure of the Single-Crystal Superalloy PWA 1484 [19]

The material undergoes a three-step heat treatment process [39]. First, there is a 1316°C for 4 hours solution heat treatment to dissolve the coarse γ' particles resulting from the casting process into a rectangular array of finer cuboidal particles. Next, a 1079°C for 4 hour cycle is used to bond a coating to the surface of the alloy and create an optimal size and distribution of γ' particles. Finally, a 704°C for 24 hour age is used to enhance the yield strength at intermediate temperatures by producing ultra fine γ' between the larger particles. The large rectangular particles are clearly visible in the

Figure 2.14, and the fine particles (indicated by an “A”) can be seen in some locations of the matrix. The cuboidal γ’ particles measure about 0.35 to 0.6 μm, while the spherical particles are about 30 nm in size.

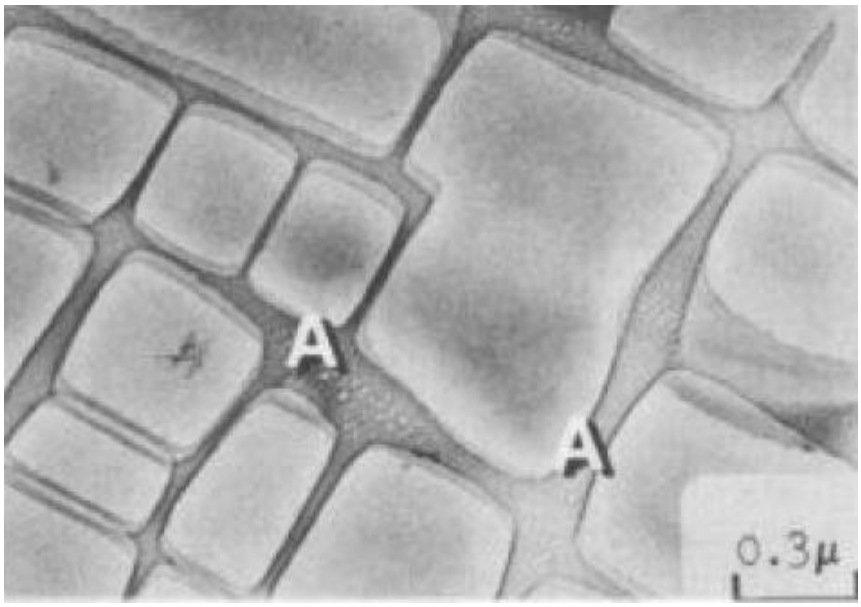

Figure 2.14: Microstructure of PWA 1484 after Heat Treatment [39]

The solidification process leads to a dendritic structure, as shown in Figure 2.15. A single-crystal nickel-based superalloy with 6.3 wt% Al, 6 wt% Cr, and additional Co, Ti, Mo, W, and Ta is shown. Both the dendritic and interdendritic regions contain uniformly distributed γ’ precipitates within the γ phase matrix, but the compositions are different. In the dendritic regions, the content of Al, Ti and Ti are typically lower, while W, Mo, and Cr are more abundant [40]. The dendrites form along the direction of casting, with the secondary arms (appearing as plus sign shapes) occurring along the <001> family of directions [41].

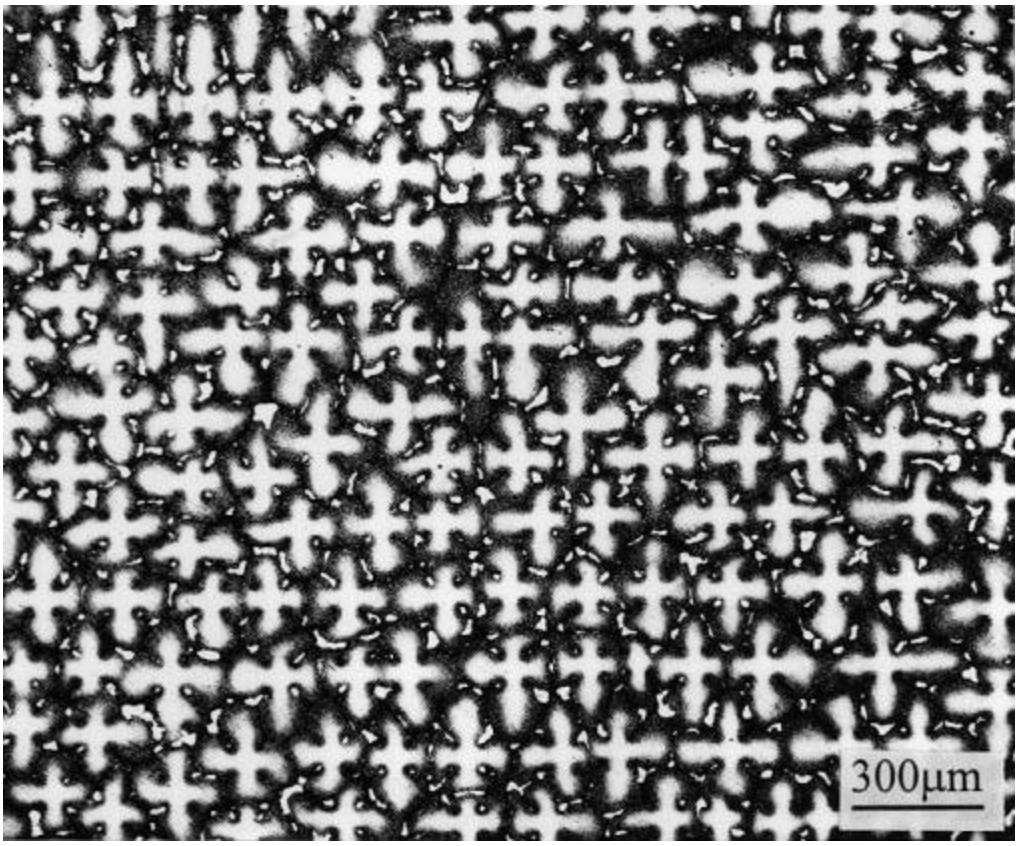

Figure 2.15: Dendritic Solidification Structure of a Single-Crystal Superalloy [40]

For comparison and completeness of this discussion, Figure 2.16 shows a schematic of the microstructure of a polycrystalline superalloy, in which the γ' distribution is much more complex. Secondary intergranular γ' particles are also present, along with tertiary γ' particles that reside within the γ grains. Currently, single-crystal materials are usually used for turbine blades. However, polycrystalline materials are still commonly used as the turbine disks where the higher temperatures are not experienced due to their isotropic properties, lower production costs, and easier machining [42].

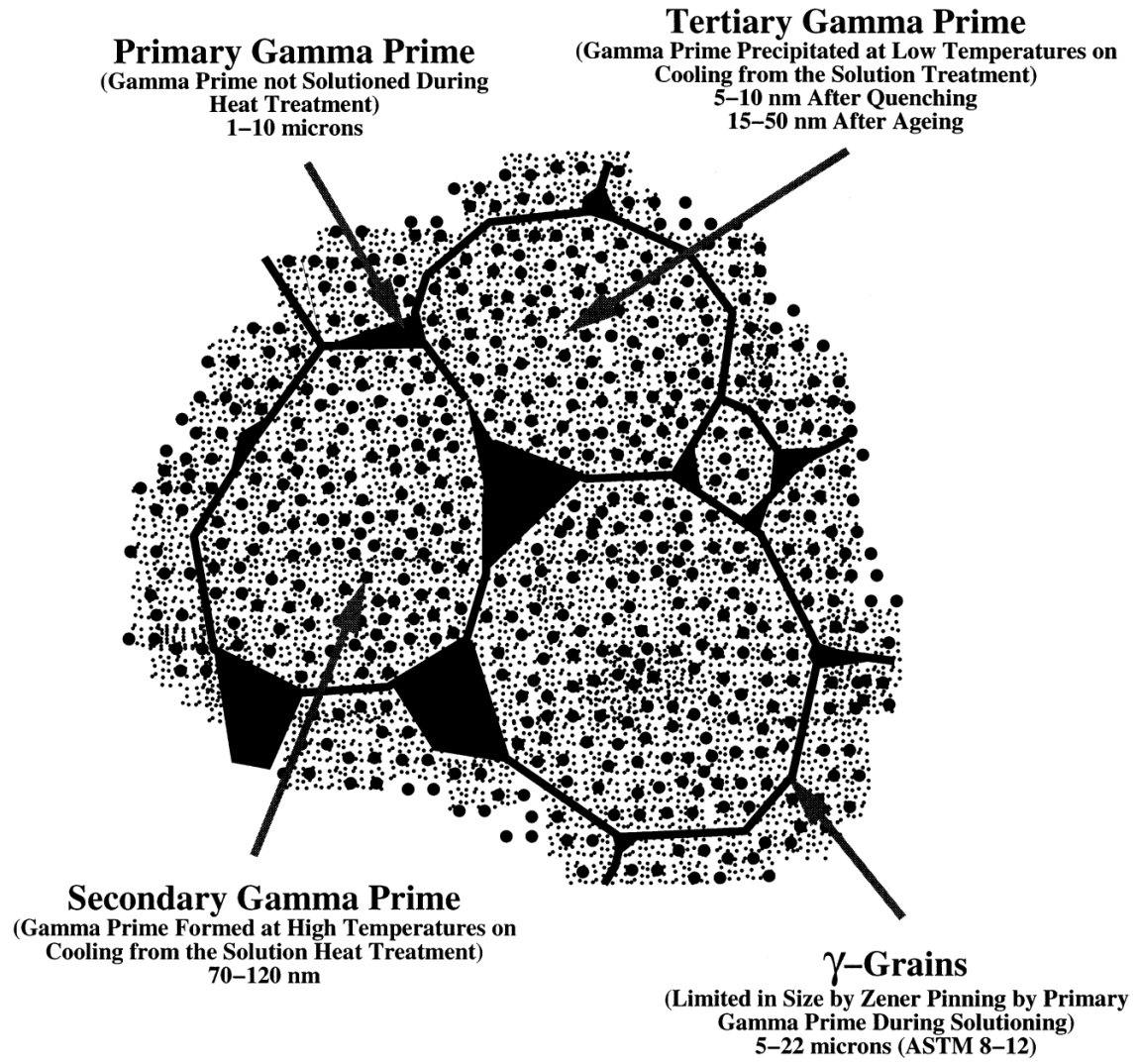

Figure 2.16: Schematic of the Microstructure of a Turbine Disc Alloy [43]

2.2.2.2: Turbine Blade Applications

The improvements in performance of single-crystal superalloys for turbine blade applications have come about due to four primary design guidelines that have been developed [1]. First, the elements should be proportioned such that the γ' volume fraction is about 70%. Murakumo *et al*. [44] performed creep experiments on the alloys TMS-75 and TMS-82+, which have identical composition for the γ' precipitates, and as shown in

Figure 2.17, this is where the optimum creep behavior is achieved. Creep dislocations do not penetrate γ' precipitates, but there is also a strengthening effect against creep deformation from the γ/γ' interfaces.

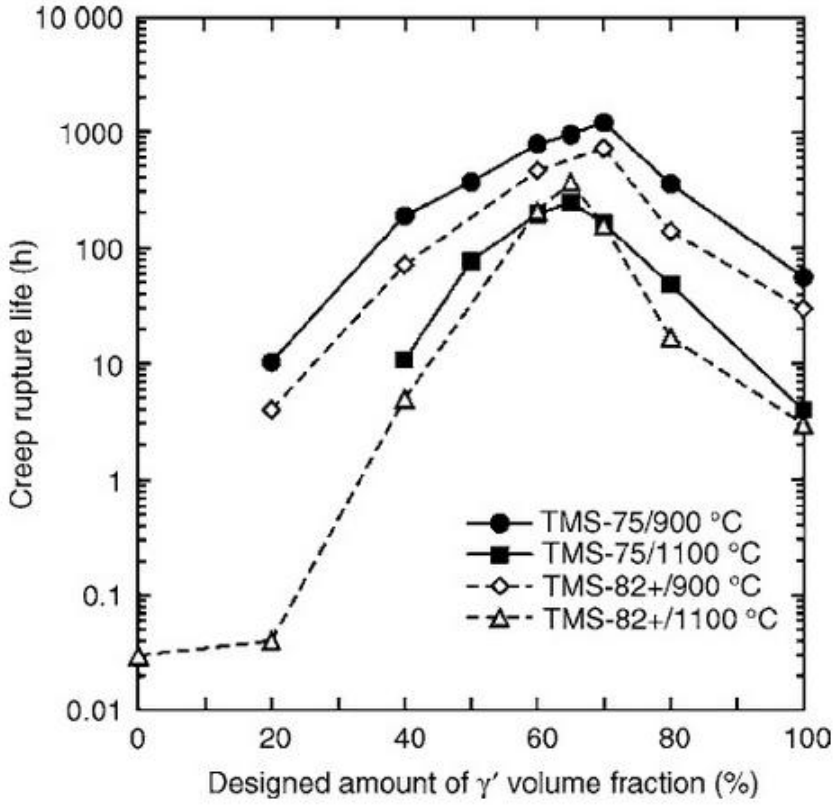

Figure 2.17: Variation of Creep Rupture Lives with Gamma Prime Fraction of Single-Crystal Superalloys [44]

Second, the composition of the alloy should be chosen so that the γ/γ' lattice misfit is small. In this case, the interfacial energy between the matrix and precipitates is minimized, and γ' coarsening is restricted. The γ' coarsening phenomenon will be discussed later in section 2.3.2.

Third, the concentrations of creep-strengthening elements (especially Re, W, Ta, Mo, and Ru) should be significant but not large enough to promote the precipitation of

topologically close-packed (TCP) phases. The best creep strengtheners are the elements that diffuse most slowly in nickel; in ascending order of effectiveness, they are Co, Cr, Ta, W, and Re. However, if these elements are too abundant, TCP phases that are detrimental to the mechanical properties of the alloy are created. Figure 2.18 shows an example of two TCP phases (σ and μ) that were created in the experimental second-generation superalloy RR2071 after aging at 900°C for 500 hours.

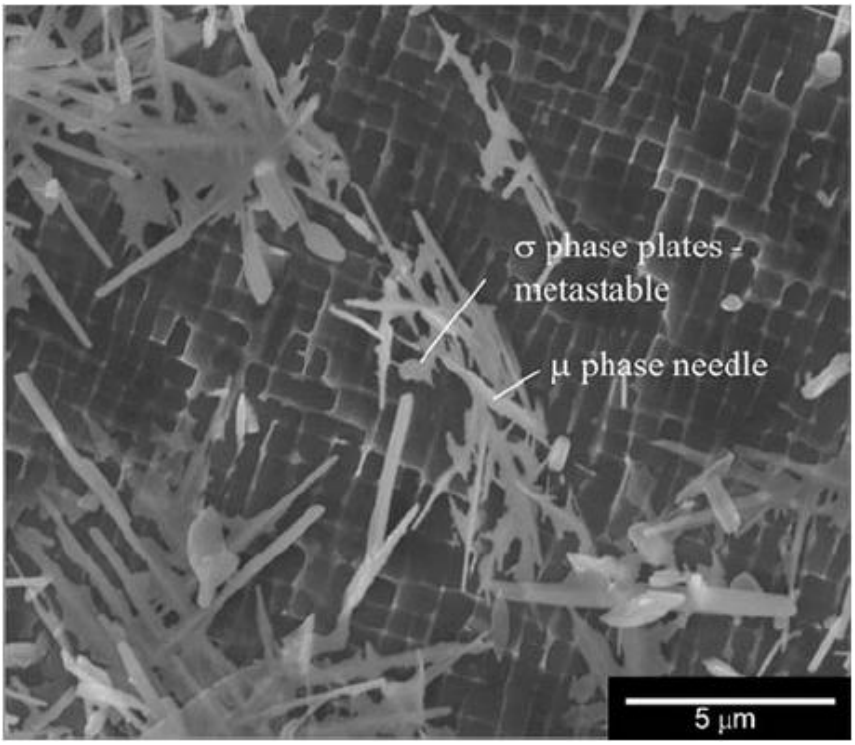

Figure 2.18: Extensive Precipitation of TCP Phases in RR2071 Aged at 900°C for 500 Hours [1]

Fourth, the composition of the superalloy should be chosen to avoid the surface degradation from exposure to hot working gases. Oxidation attack reduces the material thickness and could also lead to mechanical fatigue failure. For example, Pratt & Whitney successfully increased oxidation resistance when transitioning from the first-

generation superalloy PWA 1480 to PWA 1484, as shown by Cetel and Duhl [39]. The increase in Al content increased the tendency for aluminum oxide formation, while the decrease in Ti content decreased the rate of alumina formation. Rare-earth additions (Hf, La, and Y) also bind with sulfur impurities present in the alloy so that the sulfur does not separate the protective oxide scale from the metal surface. The resulting reduction in metal loss is depicted in Figure 2.19.

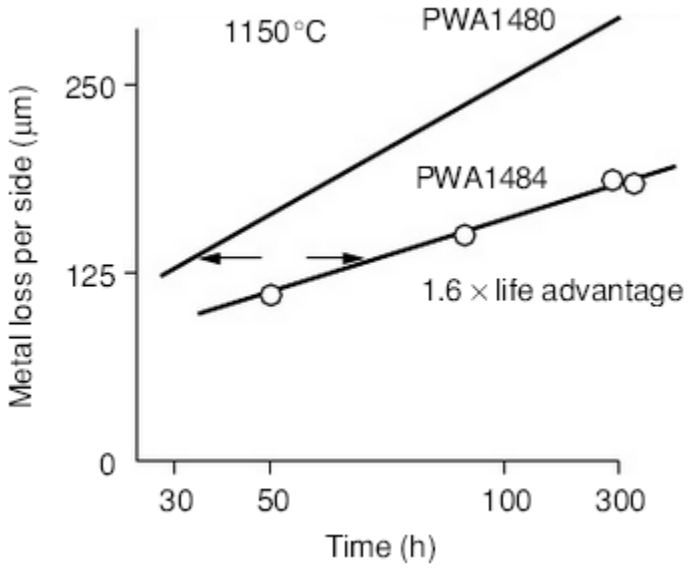

Figure 2.19: Uncoated Oxidation Resistance of PWA 1480 and PWA 1484 [39]

The evolution of the chemical composition of superalloys can be seen from Table 2.1 through Table 2.4, which display the composition of select first-, second-, third-, and fourth-generation superalloys. Over the years, as more of the four guidelines mentioned above were developed and discovered, several trends became apparent in the compositions of the newly developed superalloys. The first-generation single-crystal superalloys contain noticeable amounts of γ' hardening elements Al, Ti, and Ta, and the

grain-boundary-strengthening elements C and B from directionally solidified alloys are no longer necessary. The characteristic addition to second-generation alloys was 3 wt% Re; this amount was increased to about 6 wt% for third-generation alloys. Ruthenium was also added to create fourth-generation alloys. Overall and most notably, in the production of the newer superalloys, there have been significant additions of Re and reductions of Ti and Mo. The experimental aspect of this research focuses on the second-generation superalloy PWA 1484. It contains Cr along with excess Al that is not used to form the γ' precipitates for oxidation resistance. Several other elements are included for solid solution strengthening, increasing the γ' phase strength, and to control the mismatch between the γ matrix and γ' precipitates to ensure that the precipitates are coherent with the matrix.

Table 2.1: Chemical Compositions (Weight %) of Selected First-Generation Single-Crystal Superalloys [1]

Alloy	Cr	Co	Mo	W	Al	Ti	Ta	Nb	V	Hf	Ni	Density (g/cm^3)
Nasair 100	9	—	1	10.5	5.75	1.2	3.3	—	—	—	Bal	8.54
CMSX-2	8	4.6	0.6	8	5.6	1	6	—	—	—	Bal	8.60
CMSX-6	9.8	5	3	—	4.8	4.7	2	—	—	0.1	Bal	7.98
PWA1480	10	5	—	4	5	1.5	12	—	—	—	Bal	8.70
SRR99	8	5	—	10	5.5	2.2	3	—	—	—	Bal	8.56
RR2000	10	15	3	—	5.5	4	—	—	1	—	Bal	7.87
Rene N4	9	8	2	6	3.7	4.2	4	0.5	—	—	Bal	8.56
AM1	7.8	6.5	2	5.7	5.2	1.1	7.9	—	—	—	Bal	8.60
AM3	8	5.5	2.25	5	6	2	3.5	—	—	—	Bal	8.25
TMS-6	9.2	—	—	8.7	5.3	—	10.4	—	—	—	Bal	8.90
TMS-12	6.6	—	—	12.8	5.2	—	7.7	—	—	—	Bal	9.07

Table 2.2: Chemical Compositions (Weight %) of Selected Second-Generation Single-Crystal Superalloys [1]

Alloy	Cr	Co	Mo	Re	W	Al	Ti	Ta	Nb	Hf	Ni	Density (g/cm^3)
CMSX-4	6.5	9	0.6	3	6	5.6	1	6.5	—	0.1	Bal	8.70
PWA1484	5	10	2	3	6	5.6	—	8.7	—	0.1	Bal	8.95
Rene N5	7	8	2	3	5	6.2	—	7	—	0.2	Bal	8.70
MC2	8	5	2	—	8	5	1.5	6	—	—	Bal	8.63
TMS-82+	4.9	7.8	1.9	2.4	8.7	5.3	0.5	6	—	0.1	Bal	8.93

Table 2.3: Chemical Compositions (Weight %) of Selected Third-Generation Single-Crystal Superalloys [1]

Alloy	Cr	Co	Mo	Re	W	Al	Ti	Ta	Nb	Hf	Others	Ni	Density (g/cm^3)
CMSX-10	2	3	0.4	6	5	5.7	0.2	8	0.1	0.03	—	Bal	9.05
Rene N6	4.2	12.5	1.4	5.4	6	5.75	—	7.2	—	0.15	0.05C 0.004B 0.01Y	Bal	8.97
TMS-75	3	12	2	5	6	6	—	6	—	0.1	—	Bal	8.89

Table 2.4: Chemical Compositions (Weight %) of Selected Fourth-Generation Single-Crystal Superalloys [1]

Alloy	Cr	Co	Mo	Re	Ru	W	Al	Ti	Ta	Hf	Others	Ni	Density (g/cm^3)
MC-NG	4	<0.2	1	4	4	5	6.0	0.5	5	0.10	—	Bal	8.75
MX4 / PW1497	2	16.5	2.0	5.95	3	6.0	5.55	—	8.25	0.15	0.03C 0.004B	Bal	9.20
TMS-138	2.8	5.8	2.9	5.1	1.9	6.1	5.8	—	5.6	0.05	—	Bal	8.95
TMS-162	2.9	5.8	3.9	4.9	6	5.8	5.8	—	5.6	0.09	—	Bal	9.04

2.2.2.3: Turbine Disc Applications

For completeness of this discussion, polycrystalline superalloys used for turbine discs will also be mentioned here. Although the operating temperatures of turbine discs are much lower than those for the blades, the induced stresses are substantially higher. Therefore, there are four primary requirements for the properties of turbine disc alloys [1]. First, they must have a high yield stress and tensile strength to prevent deformation or fracture. Second, they should have high ductility and fracture toughness for damage tolerance. Next, they should resist fatigue crack initiation, and finally, they should have low fatigue crack propagation rates. As this research deals with PWA 1484, a single-crystal material used for turbine blades, the detailed guidelines for turbine disc materials will not be discussed here. The chemical composition of several superalloys used for gas turbine engine discs is given in Table 2.5. These alloys can either be produced by ingot metallurgy, where the material is produced by vacuum induction melting and then

thermally-mechanically worked [45], or through powder metallurgy. The choice of production method is dictated by the chemistry of the alloy [46].

Table 2.5: Compositions (Weight %) of Common Turbine Disc Alloys [47]

Alloy	Cr	Co	Mo	W	Nb	Al	Ti	Ta	Fe	Hf	C	B	Zr	Ni
Alloy 10	11.5	15	2.3	5.9	1.7	3.8	3.9	0.75	—	—	0.030	0.020	0.05	Bal
Astroloy	15.0	17.0	5.3	—	—	4.0	3.5	—	—	—	0.06	0.030	—	Bal
Inconel 706	16.0	—	—	—	2.9	0.2	1.8	—	40.0	—	0.03	—	—	Bal
Inconel 718	19.0	—	3.0	—	5.1	0.5	0.9	—	18.5	—	0.04	—	—	Bal
ME3	13.1	18.2	3.8	1.9	1.4	3.5	3.5	2.7	—	—	0.030	0.030	0.050	Bal
MERL-76	12.4	18.6	3.3	—	1.4	0.2	4.3	—	—	0.35	0.050	0.03	0.06	Bal
N18	11.5	15.7	6.5	0.6	—	4.35	4.35	—	—	0.45	0.015	0.015	0.03	Bal
Rene 88DT	16.0	13.0	4.0	4.0	0.7	2.1	3.7	—	—	—	0.03	0.015	0.03	Bal
Rene 95	14.0	8.0	3.5	3.5	3.5	3.5	2.5	—	—	—	0.15	0.010	0.05	Bal
Rene 104	13.1	18.2	3.8	1.9	1.4	3.5	3.5	2.7	—	—	0.030	0.030	0.050	Bal
RR1000	15.0	18.5	5.0	—	1.1	3.0	3.6	2.0	—	0.5	0.027	0.015	0.06	Bal
Udimet 500	18.0	18.5	4.0	—	—	2.9	2.9	—	—	—	0.08	0.006	0.05	Bal
Udimet 520	19.0	12.0	6.0	1.0	—	2.0	3.0	—	—	—	0.05	0.005	—	Bal
Udimet 700	15.0	17.0	5.0	—	—	4.0	3.5	—	—	—	0.06	0.030	—	Bal
Udimet 710	18.0	15.0	3.0	1.5	—	2.5	5.0	—	—	—	0.07	0.020	—	Bal
Udimet 720	17.9	14.7	3.0	1.25	—	2.5	5.0	—	—	—	0.035	0.033	0.03	Bal
Udimet 720LI	16.0	15.0	3.0	1.25	—	2.5	5.0	—	—	—	0.025	0.018	0.05	Bal
Waspaloy	19.5	13.5	4.3	—	—	1.3	3.0	—	—	—	0.08	0.006	—	Bal

2.3: Mechanical Properties of Single-Crystal Superalloys

2.3.1: Temperature Dependence of Strength

Figure 2.20 displays the yield stress as a function of temperature for several single-crystal superalloys along the <001> direction (the crystal orientation with the largest strength). For most other alloy systems, the yield stress greatly decreases with increasing temperature. In contrast, the yield stress for these nickel-based superalloys actually increases with temperature up to about 800°C, but then it begins to decrease quickly, and the material becomes considerably weaker near 1200°C.

This anomalous yielding behavior is due to the γ' phase. At lower temperatures, any decrease in strength of the γ matrix is counteracted by the strengthening of the precipitates [48]. As the temperature increases, cross-slip from octahedral planes to cubic planes within the γ' particles is enhanced, which resists deformation and hardens the

particles. However, at higher temperatures, coarsening of the particles allows increased Orowan looping, and the γ' precipitates also may begin dissolving. As a result, the yield stress peaks when the effects of these deformation mechanisms are balanced.

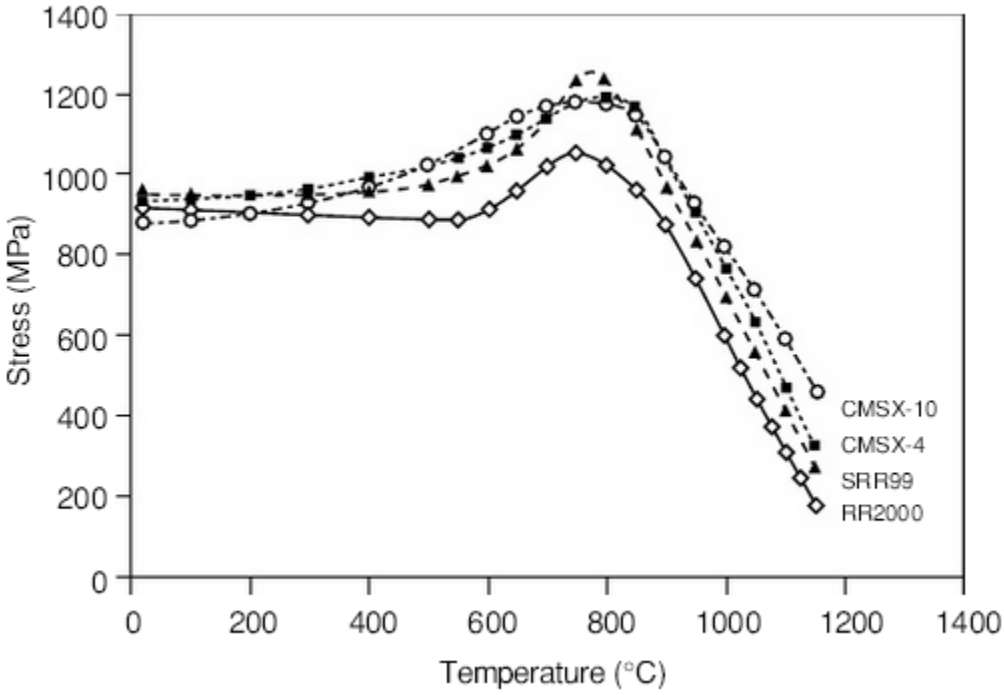

Figure 2.20: Variation of Yield Stress with Temperature for Several Single-Crystal Superalloys [1]

The temperature-dependent tensile properties of PWA 1484 determined by Cetel and Duhl [39] are shown in Figure 2.21. The yield strength as well as tensile ductility are displayed. At room temperature, PWA 1484 has a yield strength of about 960 MPa, increasing to almost 1000 MPa near 750°C. Similar to the other single crystal superalloys, the strength begins to decrease drastically with increasing temperature after the peak strength is reached.

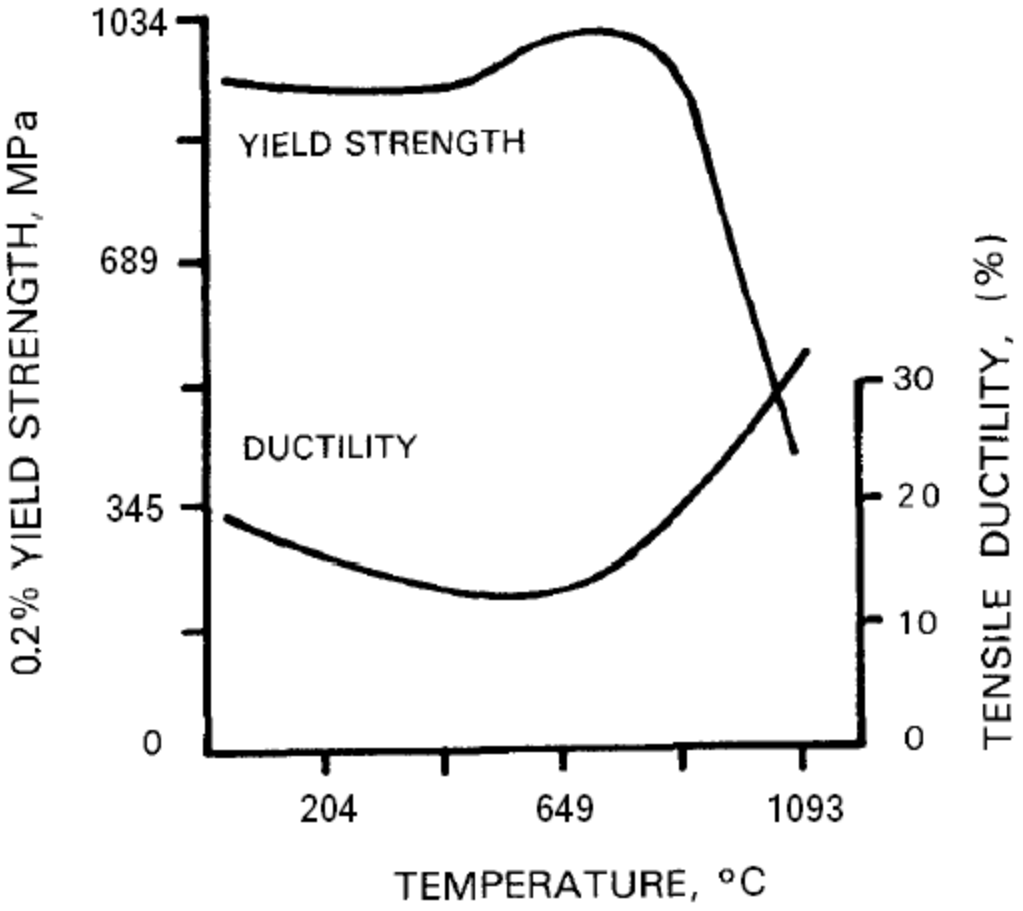

Figure 2.21: Tensile Properties of PWA 1484 as a Function of Temperature [39]

2.3.2: Behavior in Creep

Creep deformation, or the time-dependent inelastic deformation of a material at a stress well below yield, is of great interest when considering superalloys held at temperature within a gas turbine engine. Data has shown that the mechanism of creep deformation is sensitive to the temperature and stress, resulting in several creep regimes with distinct modes of microstructural degradation [49]. Figure 2.22 shows creep data for the single-crystal superalloy CMSX-4 in the <001> direction at three different combinations of temperature and stress. In each case, plots of creep strain vs. time and

creep strain rate vs. creep strain are provided. Primary creep deformation occurs at lower temperatures with sufficiently high stresses, as shown in Figure 2.22(a), where the strain rate first increases and then decreases with increasing creep strain. The amount of primary creep increases with the applied stress, and significant primary creep only occurs above a threshold of about 500 MPa. Primary creep results in inhomogeneity of slip, so initially cylindrical creep specimens can become elliptical due to the considerable creep anisotropy in single-crystal superalloys [50]. After primary creep, secondary creep may occur, where the creep strain rate is essentially constant. The secondary creep rate is proportional to the amount of primary creep strain [51].

Tertiary creep, which is observed in Figure 2.22(b), occurs in all known single-crystal superalloys at intermediate levels of temperature and stress [1]. In this regime, the creep strain rate increases monotonically with the creep strain rate, and there is no period of steady-state creep as is observed in polycrystalline superalloys. The γ' particles remain intact, and the dislocation motion is restricted to the γ channels.

The rafting regime occurs at temperatures above about 1050°C, as shown in Figure 2.22(c). There is a creep-hardening effect where the creep strain stays essentially constant before it drastically increases. The γ/γ' microstructure degrades quickly due to the high temperatures, causing equilibrium interfacial dislocation networks to form at the interfaces [52]. In addition, the γ' particles undergo directional coarsening, or rafting, causing them to coalesce [53-55].

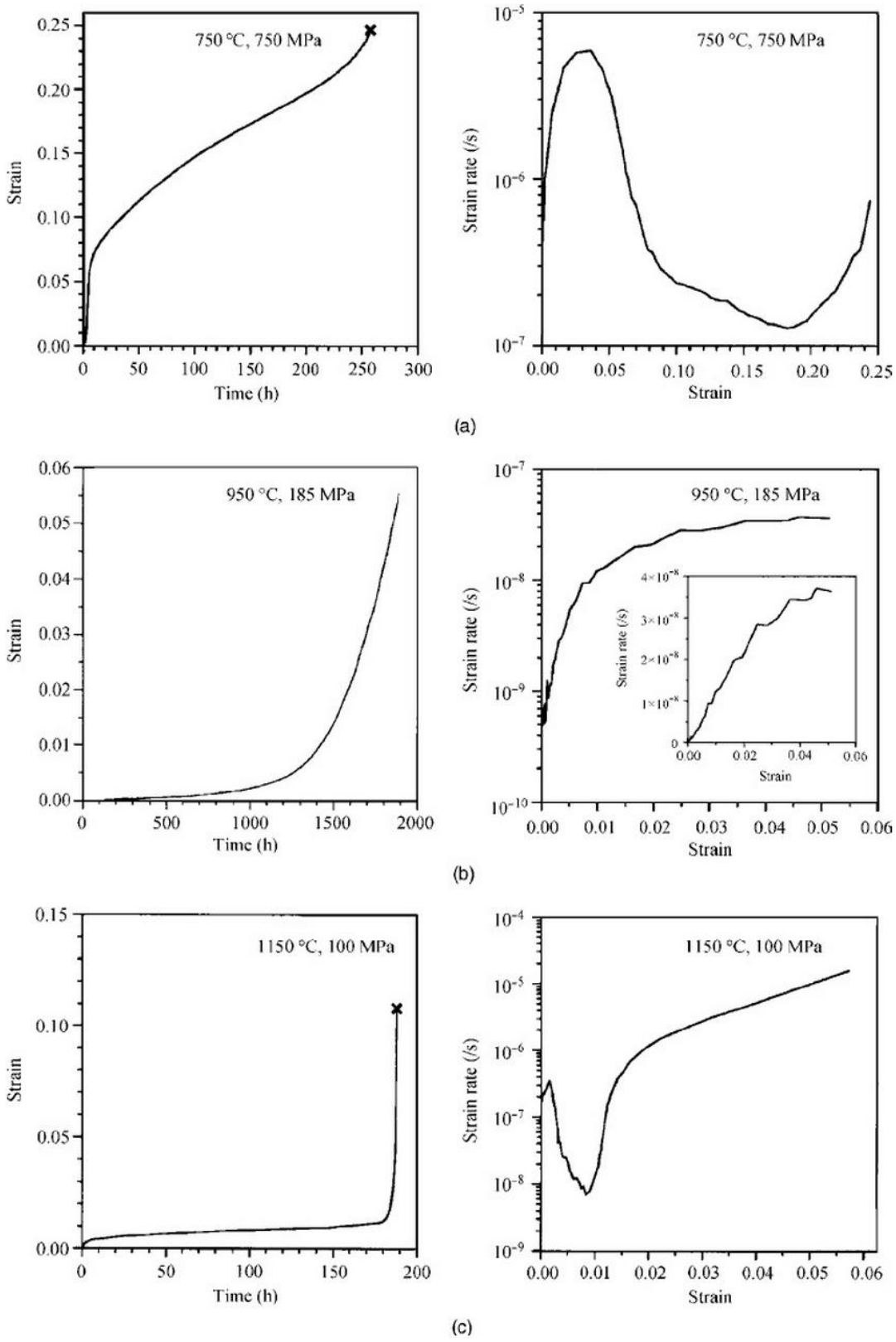

Figure 2.22: Constant Load Creep Data for CMSX-4 at Different Temperatures and Stresses [51]

An example of rafting can be found in Figure 2.23, which shows the γ/γ' microstructure of CMSX-4 after being deformed at 1150°C and 100 MPa for 10 hours. The tensile loading direction is vertical in the plane of the picture. The broad faces of the rafts are perpendicular to the axis of loading due to the negative lattice misfit.

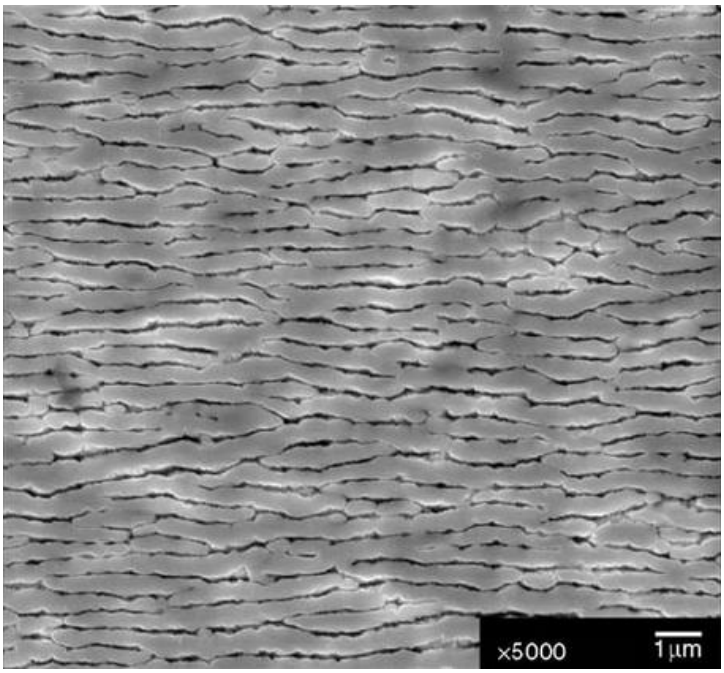

Figure 2.23: Rafted Microstructure of CMSX-4 After Deforming at 1050°C and 100 MPa for 10 Hours [53]

Figure 2.24 displays a comparison of the creep strength of PWA 1480 and PWA 1484 by Cetel and Duhl [39]. The amount of stress required to obtain 1% creep strain in 300 hours was measured. It can be seen that for a stress of 207 MPa, the improvements in the composition for PWA 1484 allowed a temperature increase of 39°C to result in the same amount of creep. This also corresponded to a fourfold life advantage at the same stress level and temperature. This major breakthrough could result in significant weight reduction for the overall structure.

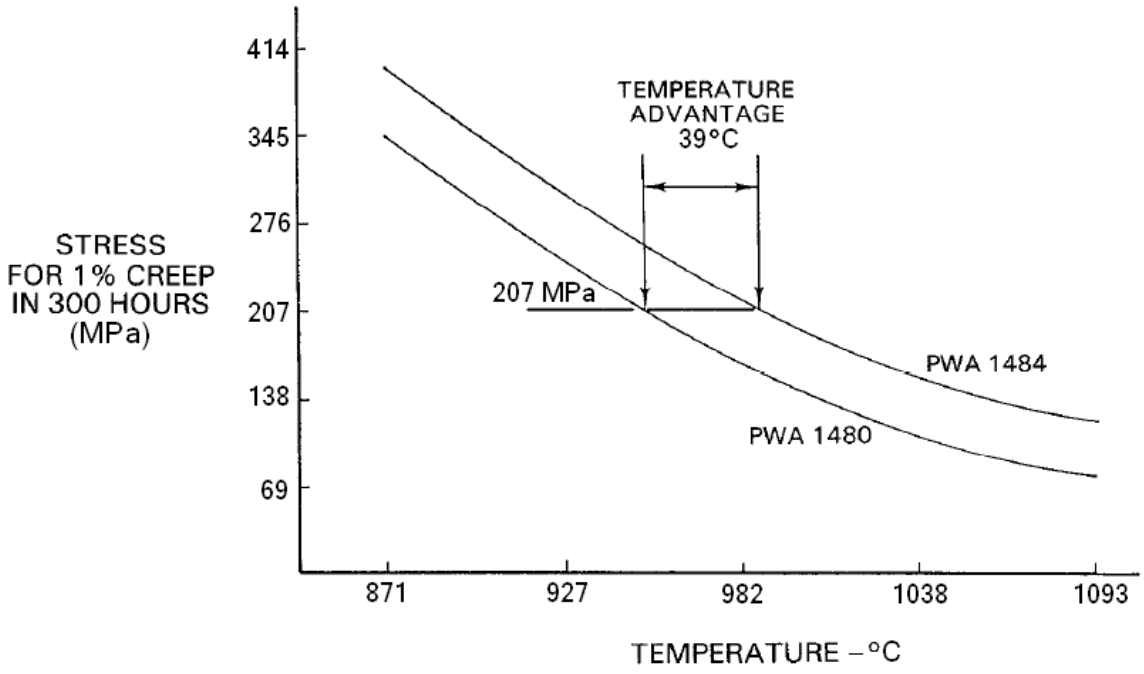

Figure 2.24: Creep Strength of PWA 1480 and PWA 1484 [39]

2.3.3: Behavior in Fatigue

For superalloys, as with other metals, fatigue damage usually occurs in the form of localized slip along certain lattice planes [56]. At temperatures around 700°C with high stresses, persistent slip bands can be formed and shear the γ' particles [57]. At higher temperatures and low stresses, dislocation movement is limited to the γ matrix channels, so deformation occurs in the {111} lattice planes with the highest stresses, and crack initiation occurs at surface pits or cracks in the oxide layer [58].

Low-cycle fatigue (LCF) occurs when the nominal stress applied to the material is larger than the elastic limit. Most of the fatigue life is spent in the crack propagation state, and failure usually occurs within 10^5 cycles for superalloys. In turbine blades, LCF results from abrupt changes in loading during engine start-up and shut-down [1]. Dalal *et*

al. [59] showed that the LCF behavior of single-crystal superalloys is very sensitive to crystal orientation, as shown in Figure 2.25. Experiments were performed on smooth, polished specimens of a Ni-6.8Al-13.8Mo-6W alloy at 980°C under total strain control at 0.33 Hz with R = 0. For all crystal orientations, the logarithm of the strain range was found to be inversely proportional to the logarithm of the fatigue life. The <001> crystal orientation, which has the lowest elastic modulus, displayed the best performance in fatigue, while the <111> orientation, which has the highest elastic modulus, performed the worst. As a result, it was shown that the fatigue strength strongly corresponds to the elastic modulus of the crystal orientation in an inverse manner due to the higher stresses experienced in the stiffer directions.

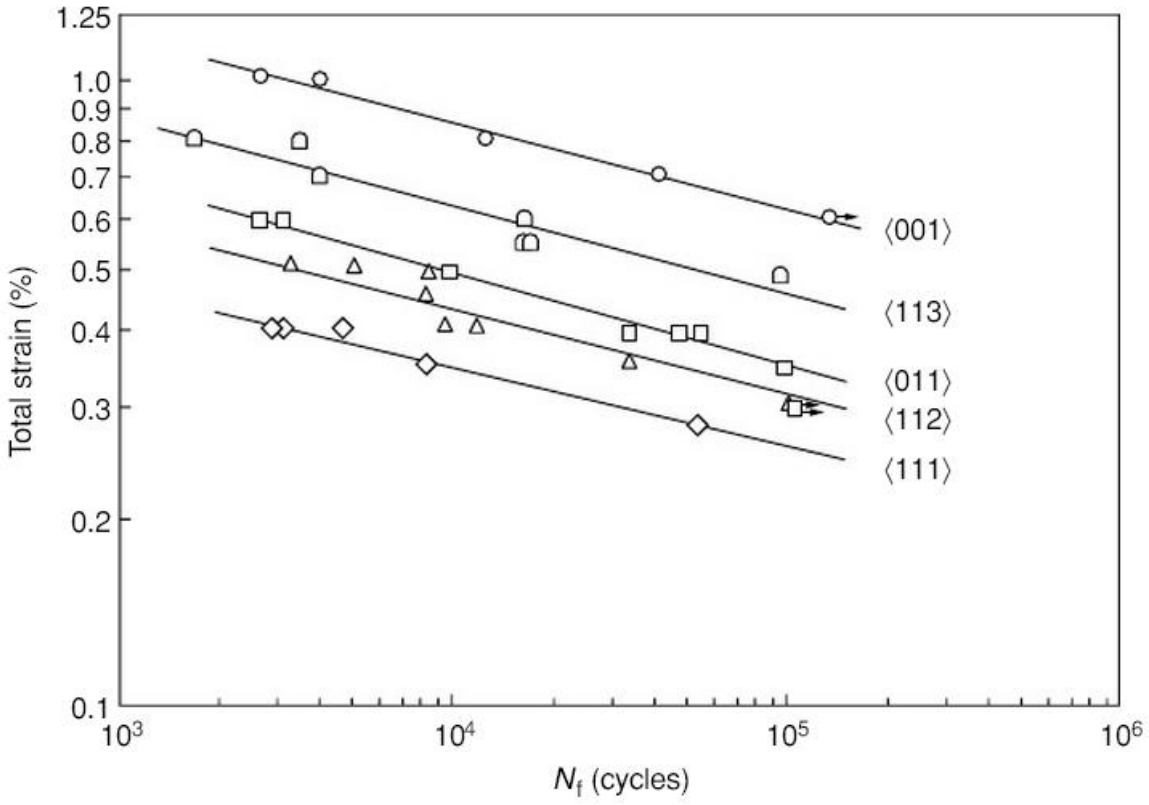

Figure 2.25: Orientation Dependence of Strain-Controlled LCF Life of a Single-Crystal Superalloy at 980°C and 0.33 Hz with R = 0 [59]

Experiments performed by MachLachlan and Knowles [60] explored the effects of LCF life of the single-crystal superalloy CMSX-4, as shown in Figure 2.26. LCF tests were performed under load control with R = 0 at temperatures between 750°C and 1050°C. The LCF life was found to decrease quickly and non-linearly with increasing temperature, and no endurance limit was observed.

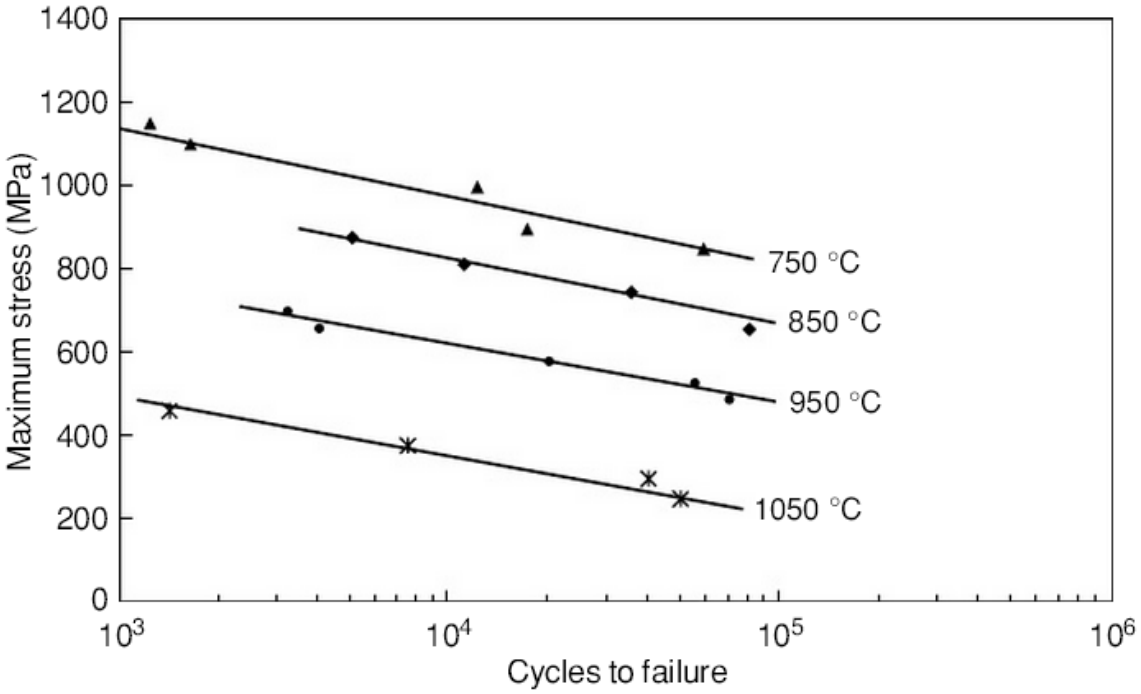

Figure 2.26: Temperature Dependence of Load-Controlled LCF Life of Uncoated CMSX-4 with R = 0 [60]

High-cycle fatigue (HCF) occurs when the stress amplitudes are small and always within the elastic regime. The majority of the fatigue life is spent in the crack initiation stage, and failure usually occurs after 10^5 cycles. For turbine blades during HCF, vibrations are superimposed on the mean stress induced from the centrifugal force as well as the thermal loads from thermal gradients in the blade [1]. Wright *et al*. [9] explored the

effect of *R*-ratio and frequency on the HCF life of PWA 1484 with a platinum oxide coating. All of the tests were performed under load control on <001> specimens at 1038°C. Figure 2.27 shows the results of the first set of experiments, which were performed at 59 Hz for varying *R*-ratios. No endurance limit was observed, and the HCF lives decreased while the slope of the stress-life curve became steeper as the *R*-ratio was increased towards 1. When the mean stress is plotted against the time to failure, as in Figure 2.27(b), the data for the higher *R*-ratios collapses to a single line, meaning that the life is becoming independent of *R*-ratio and that creep is the dominant damage mechanism. However, for lower *R*-ratios, fatigue is the dominant mechanism.

Figure 2.28 displays the data obtained by Wright *et al*. [9] at varying frequencies with two different *R*-ratios. For $R = -1$, the results were found to be independent of frequency, meaning that a time-independent fatigue process is dominant at low mean stresses. For $R = 0.1$, the HCF life was larger at higher frequencies, meaning that a time-dependent creep and/or environmental degradation process was dominant in failure. At the lower frequencies, there was much more time per cycle for these processes to take effect, leading to the much shorter lives.

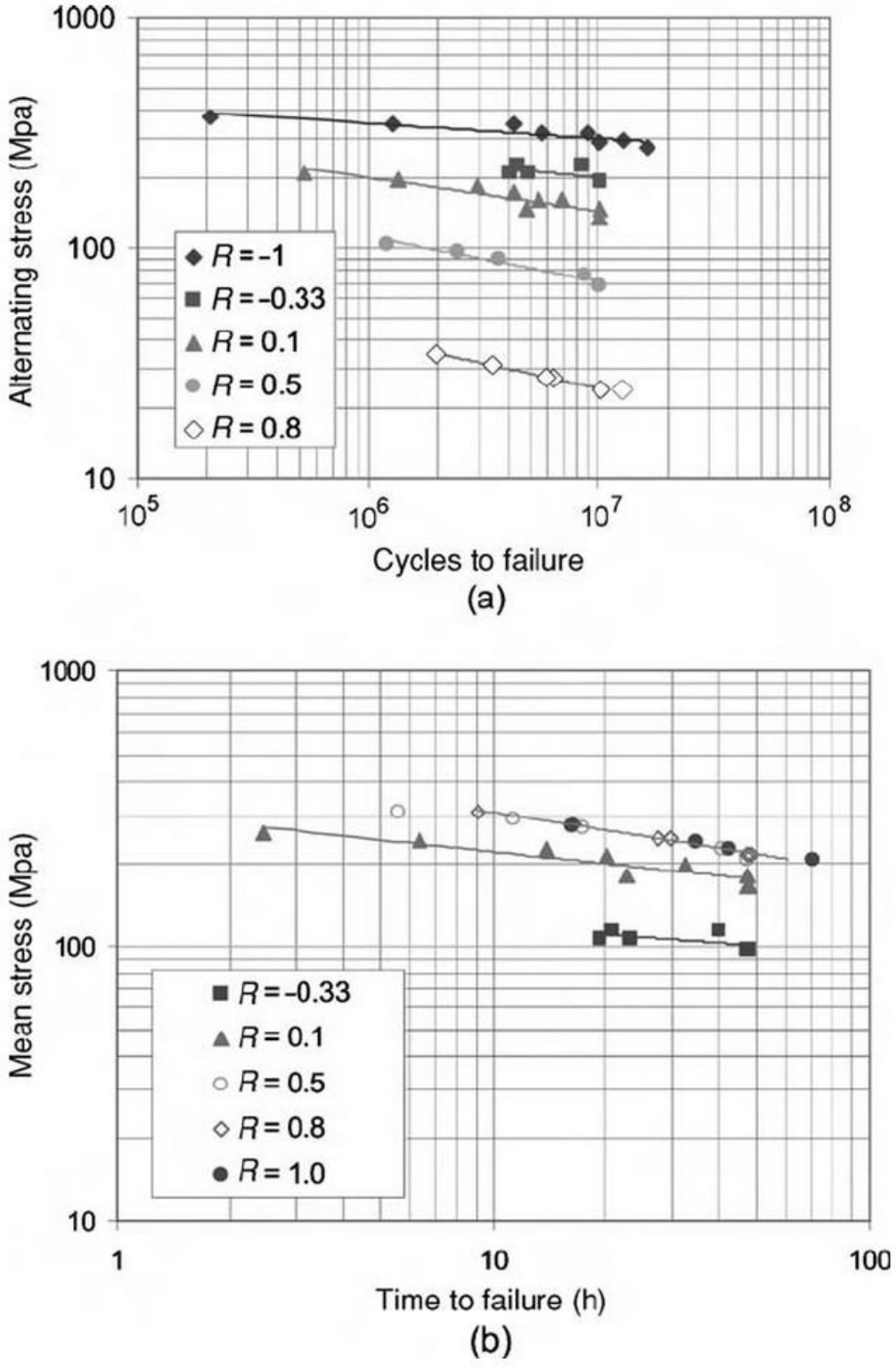

Figure 2.27: HCF Data for Coated PWA 1484 at 1038°C and 59 Hz Showing the Effect of *R*-ratio [9]

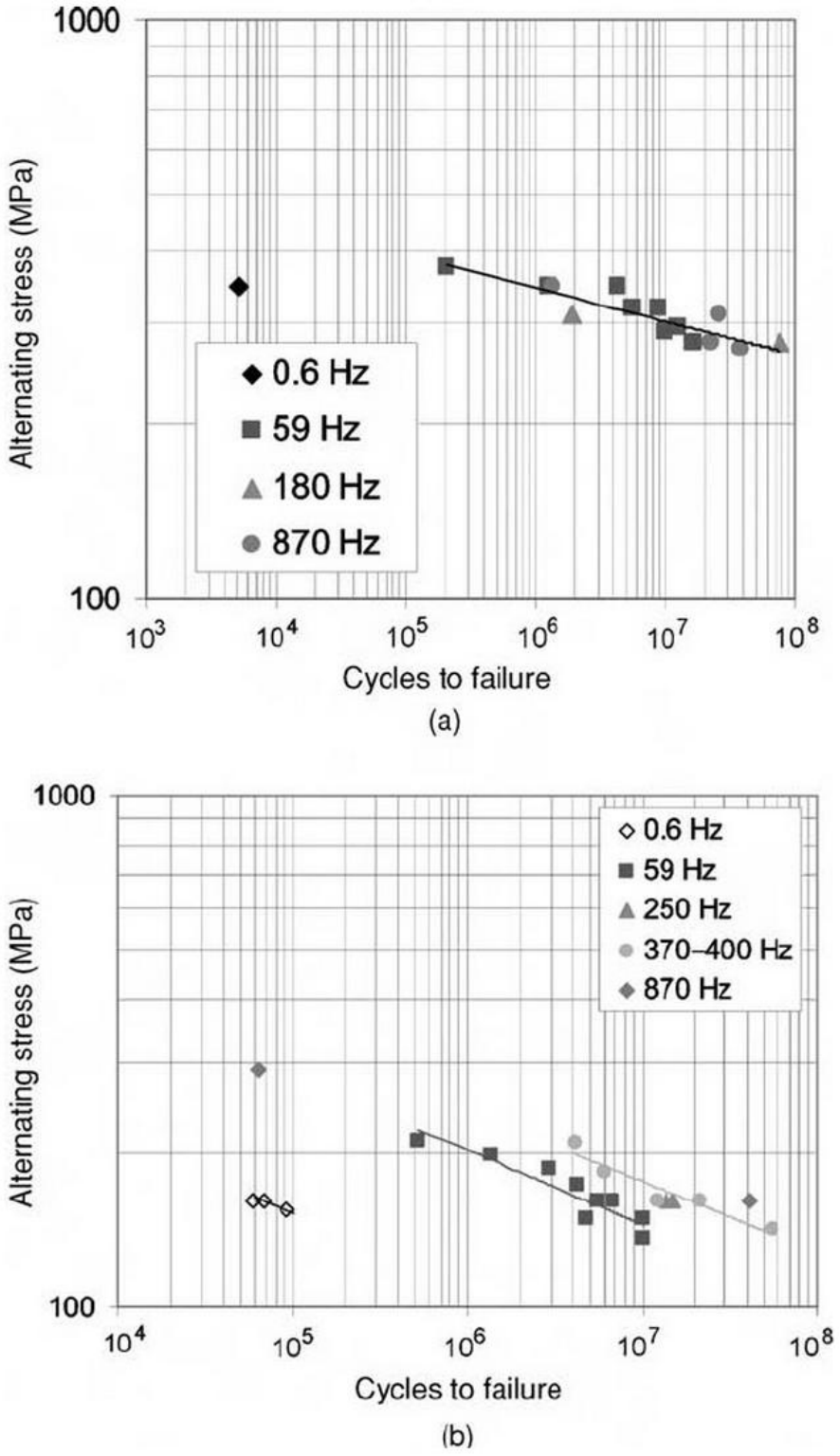

Figure 2.28: HCF Data for Coated PWA 1484 at 1038°C Showing the Effect of Frequency with (a) R = -1 and (b) R = 0.1 [9]

Figure 2.29 shows an example of a modified Goodman diagram (alternating stress vs. mean stress) created for the HCF life of PWA 1484 at 871°C with a defined 10^7 cycle endurance. HCF tests were performed by Cetel and Duhl [39] on smooth and notched specimens of the alloy between 593°C and 982°C. At these high temperatures, the fatigue results showed significant improvement over previous alloys like PWA 1480 due to the superior creep performance.

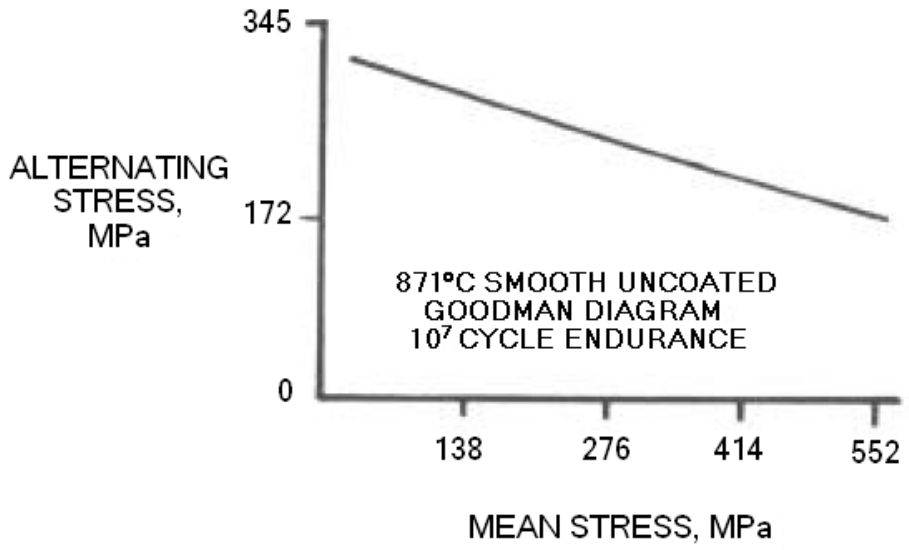

Figure 2.29: Modified Goodman Diagram for PWA 1484 at 871°C [39]

2.4: Environmental Degradation of Superalloys

2.4.1: Oxidation

Giggins and Pettit [61] examined the oxidation of Ni-Cr-Al alloys of varying compositions at temperatures of 1000°C, 1100°C, and 1200°C. Each alloy contained nickel, and some contained only the γ phase, while others also included the γ' and/or αCr phases. It was found that all of the alloys experienced a period of transient oxidation

before steady-state conditions were reached. During this period, the surface of the alloy was rapidly converted to oxide layers, and the composition of the oxide was constantly changing. After steady-state was reached, the alloy could be categorized as either a Group I, Group II, or Group III alloy. However, some alloys, called transition alloys, showed an oxidation layer of constantly-changing composition.

The typical oxidation behavior observed for a Group I alloy is shown in Figure 2.30. Group I alloys typically followed parabolic rate laws with a short transient period. The oxidation rate for these alloys was much greater than that of pure nickel. The nickel was oxidized externally to form a continuous scale of NiO, and a discontinuous subscale of Al_2O_3 and Cr_2O_3 was formed due to internal oxidation of the aluminum and chromium. The oxidation rates were controlled by transport through the NiO scale.

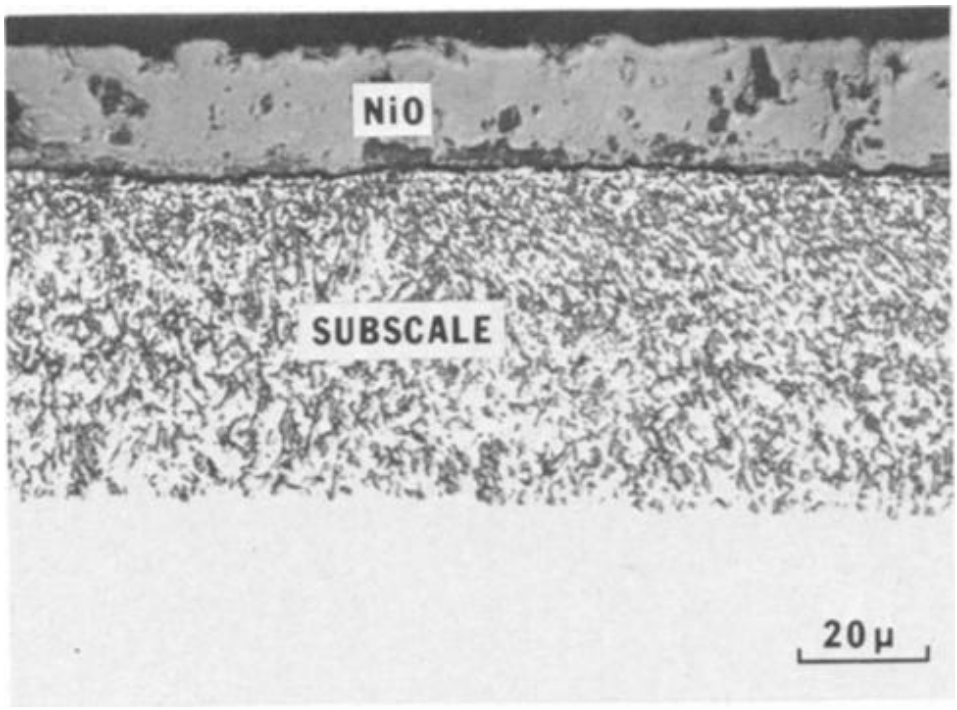

Figure 2.30: Representative Oxidation Mechanism for Group I Alloys [61]

Figure 2.31 shows the oxidation behavior of Group II alloys. The oxidation usually followed the parabolic rate law, although some experiments showed deviation. There is a dense outer layer of Cr_2O_3 with a subscale precipitate of Al_2O_3. The oxidation rate was controlled by diffusion through the aluminum-doped Cr_2O_3 scale. PWA 1484 has been found to be a Group II oxide former, with dominant oxides consisting of spinel, NiO, α-Al_2O_3, or some combination of the three [14].

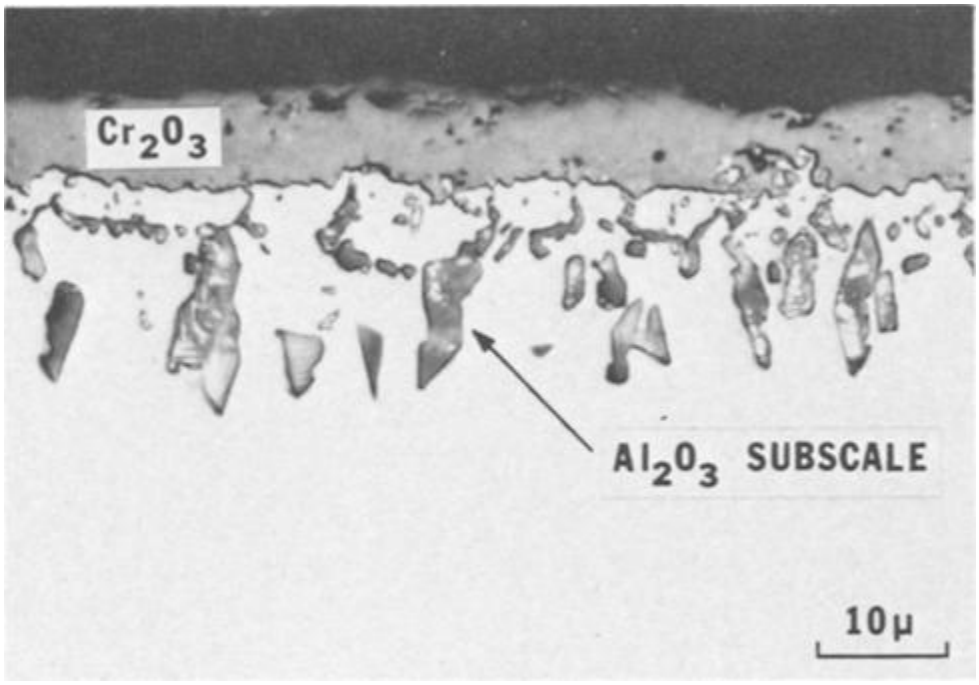

Figure 2.31: Representative Oxidation Mechanism for Group II Alloys [61]

The oxidation mechanisms shown by Group III alloys can be found in Figure 2.32. These alloys essentially obeyed a parabolic rate law from the start of oxidation. The rate constants were found to be substantially smaller than those for Group I or II alloys. Oxide scales on the surface consisted of only Al_2O_3, and the oxidation rate was controlled by diffusion through this scale.

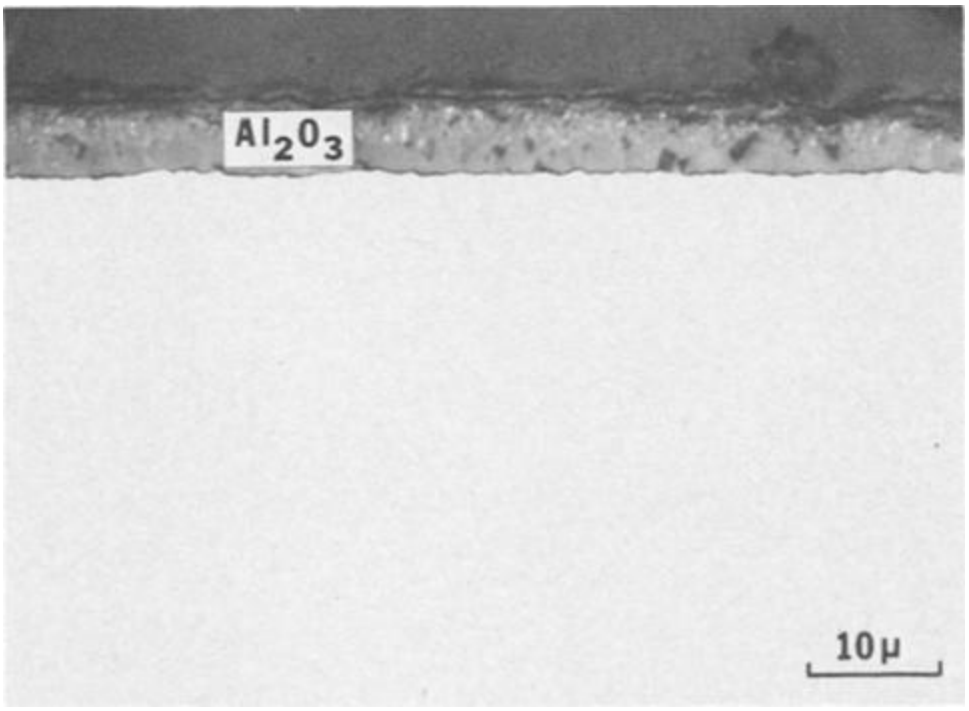

Figure 2.32: Representative Oxidation Mechanism for Group III Alloys [61]

For practical superalloys, oxidation is not as clearly defined into the groups described above, and the behavior becomes complicated due to the number of elements composing the alloy. As deduced by Giggins and Pettit [61], the oxidation behavior is heavily dependent on alloy composition. Figure 2.33 shows an example of the oxidation behavior of the third-generation superalloy CMSX-10 after being exposed to certain temperatures for 100 hours. CMSX-10 does not form an alumina scale, and an external NiO scale as well as internal oxidation can be observed [62]. With the increased Re content and decreased Cr content, the alloy cannot resist either the formation of the thick Ni scale or internal oxidation. As a result, a surface coating is extremely necessary in practical applications of the material.

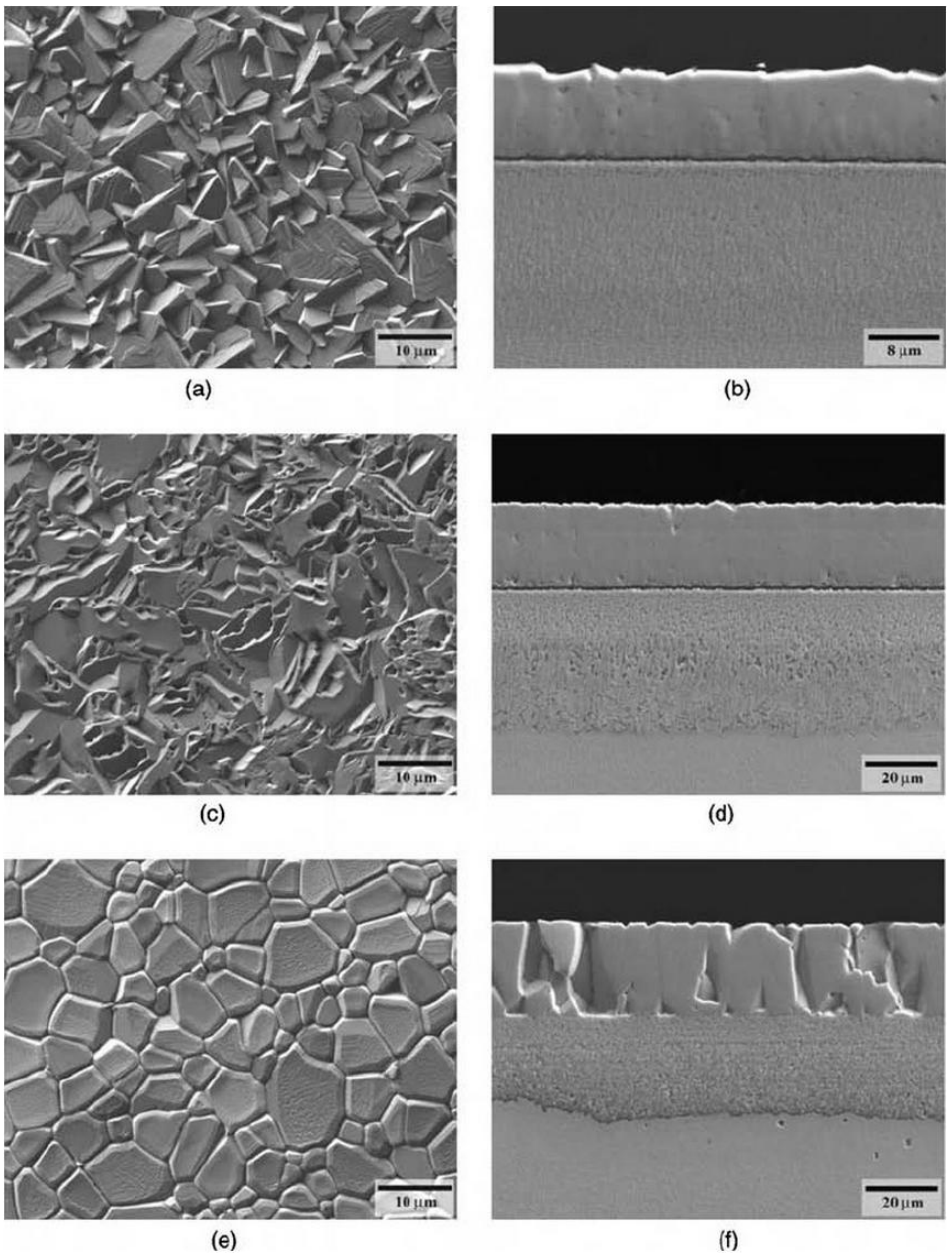

Figure 2.33: Surface and Cross-Section Views of Oxidation of CMSX-10 After Heat Treatment for 100 Hours at (a,b) 800°C, (c,d) 900°C, and (e,f) 1000°C [1]

A cyclic oxidation study was recently performed on typical single-crystal superalloys of each generation with one-hour hold times at 1100°C [1]. The results of the study are shown in Figure 2.34. At higher cycle counts, the first-generation superalloys demonstrated the best performance, with performance decreasing with each generation.

This is due to the increasing emphasis being placed on different mechanical properties and less dependence on the alloy composition to impart oxidation resistance. Instead, the superalloys are increasingly reliant on surface coatings for protection from the environment.

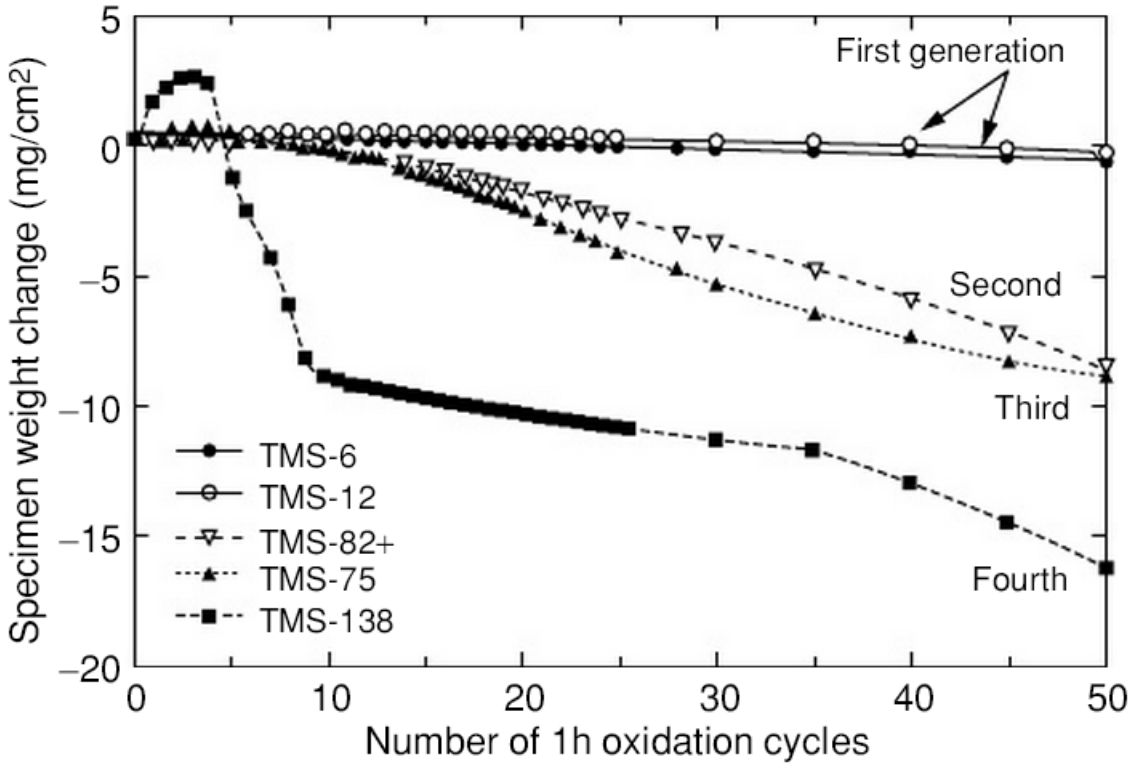

Figure 2.34: Results of Cyclic Oxidation Testing of Single-Crystal Superalloys [1]

Oxidation attack of superalloys can easily be the initial cause of eventual fatigue failure [1]. Wright [63] performed low cycle isothermal fatigue experiments on the second generation single-crystal superalloy René N4 in an uncoated form. As shown in Figure 2.35, there was extensive oxidation damage at the surface, and a fatigue crack initiated at oxide pits.

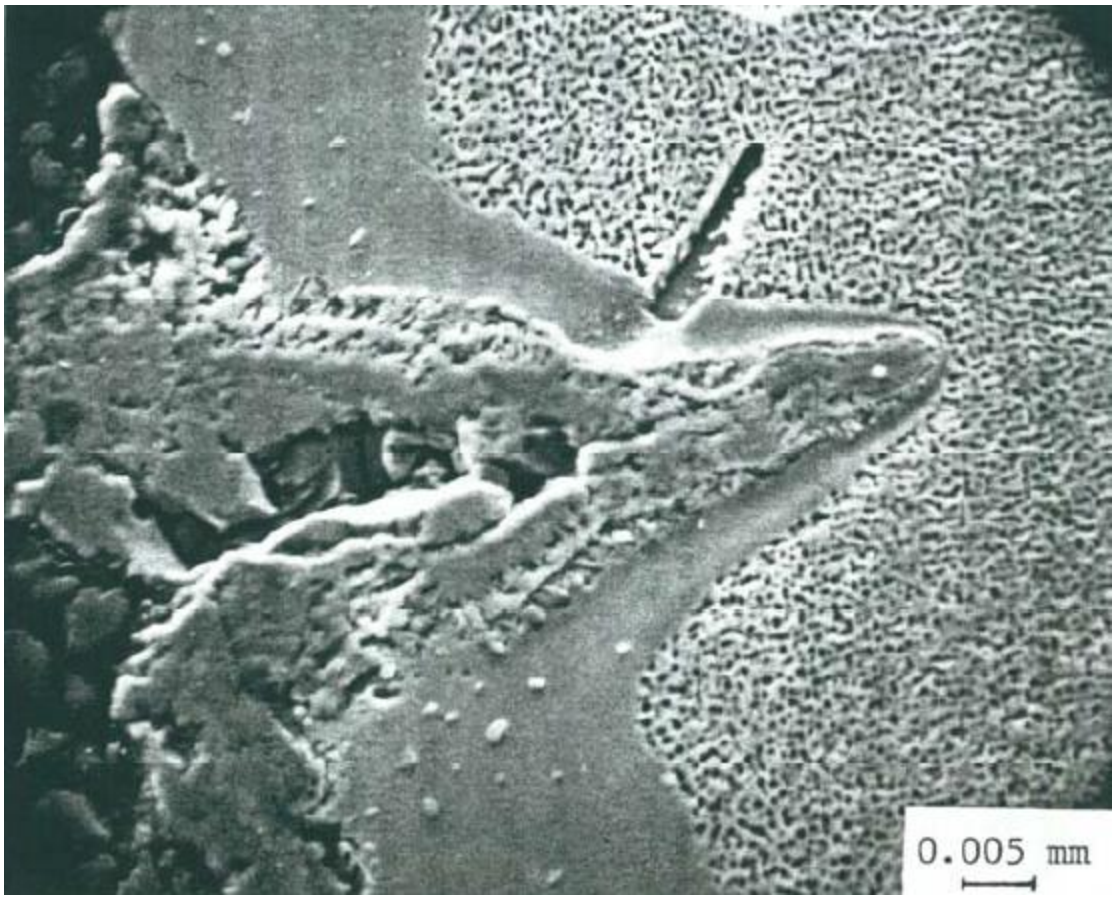

Figure 2.35: Fatigue Crack Initiation from Oxide Pits in Uncoated René N4 [63]

2.4.2: Gamma Prime Depletion

The oxidation of superalloys causes the depletion of the γ' particles near the surface. This can occur when aluminum diffuses into the surface of the alloy, creating an aluminum-rich surface oxide, or when oxygen diffuses into the surface to form subsurface alumina particles [64]. Studies involving a wide variety of superalloys, including both single crystal and directionally solidified alloys, all found evidence of γ' depletion at high temperatures [61-67]. The depletion of the strengthening precipitates results in the weakening of the microstructure, which causes a greater amount of plasticity from equivalent loading conditions. Zhao *et al*. [68] performed analysis on the

response of CMSX-4 at a notch tip to examine the effects of γ' depletion. Figure 2.36 shows the resulting plastic strain distribution near the notch tip after a constant load for 400 hours at 950°C with and without oxidation effects. It can clearly be seen that the environmental damage has caused a redistribution of stresses and an increased accumulation of plastic strain, indicating that the environmental degradation led to increased mechanical damage. Dumoulin *et al*. [69] also produced similar results.

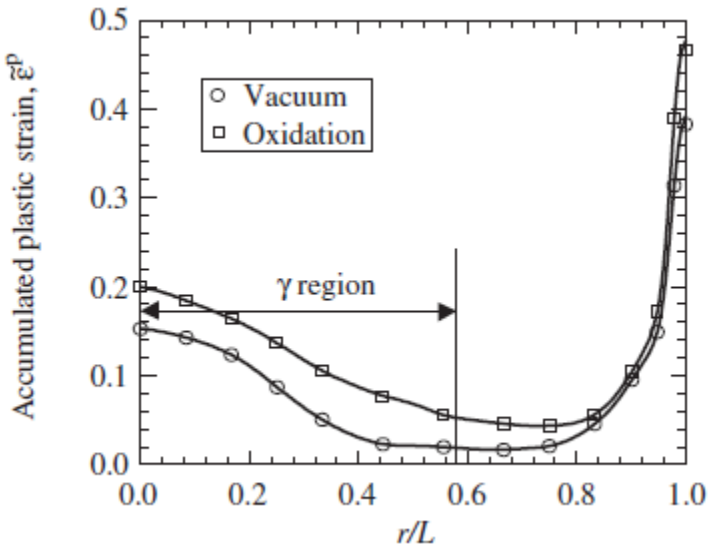

Figure 2.36: Distribution of Plastic Strain Near a Void with and without Oxidation at 950°C for 400 Hours [68]

2.5: Coatings

Since the entry temperatures of gas turbine engines have increased beyond the melting temperatures of the materials used, the components would degrade quickly without the protection they receive from surface coatings [4]. As a result, the design of coatings and measures to make sure they remain intact and compatible with the base metal of the components have become very important considerations. However, because

of the mechanical properties of the coatings and mismatches in the coefficients of thermal expansion between the coating and base metal, the coatings tend to crack and spall relatively quickly [1]. In addition, the cracks in the coating may propagate into the base metal itself due to the localized stress concentration, which causes increased crack growth rate in the superalloy [8]. Work performed by Heine *et al*. [70] demonstrated that coatings could result in up to 7.5 times shorter fatigue life when compared to the uncoated alloy.

Figure 2.37 displays the relative coating lives and turbine temperature enhancements provided by three common coating technologies: diffusion coatings, overlay coatings, and thermal barrier coatings. Diffusion coatings are the most common and often consist of an aluminum layer deposited onto the surface by chemical vapor deposition, and a heat treatment promotes adhesion and diffusion with the substrate to form an aluminum-rich layer on the surface [71]. A layer of platinum may be placed on the surface before the aluminization process to increase oxidation resistance [72]. Overlay coatings provide greater resistance to oxidation and corrosion, but they are more costly because they must be applied by air or vacuum plasma spraying or electron beam physical vapor deposition [73, 74]. Gas turbine components are usually coated with MCrAlX-type materials with various compositions, where "M" refers to some combination of Ni and Co and "X" refers to reactive elements [75, 76]. Unlike diffusion coatings, these overlay coatings have flexibility in compositions which are independent of the substrate. Thermal barrier coatings offer an even greater advantage and involve a ceramic layer being deposited on the superalloy, which provides insulation and lowers the temperature of the substrate. To prevent spallation of the coating, a bond coat (some

form of diffusion or overlay coating) is usually deposited between the ceramic layer and the superalloy [77, 78].

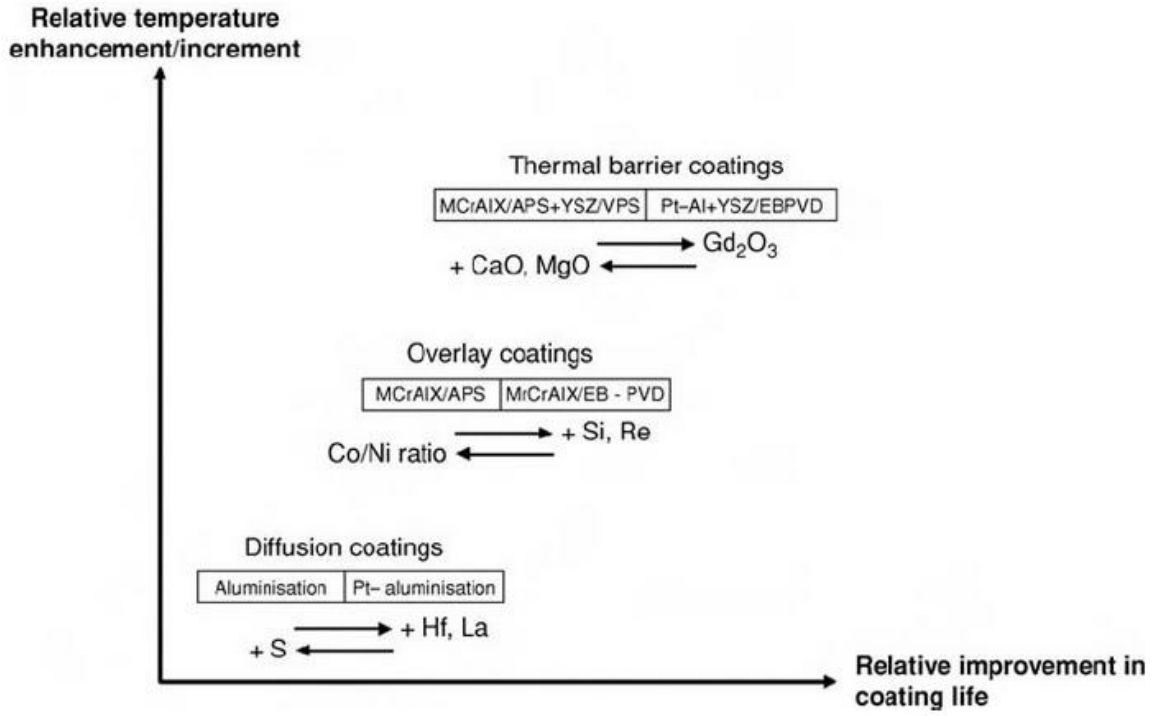

Figure 2.37: Relative Coating Lives and Turbine Temperature Enhancements from Three Coating Forms [79, 80]

Tamarin *et al*. [4, 5] performed load-controlled out-of-phase TMF tests on CMSX-4 with and without coatings; the results are displayed in Figure 2.38. As labeled in the figure, the uncoated superalloy (4), as well as the alloy with Co-32Ni-21Cr-8Al-Y (1), Ni-8Co-12Cr-7Al-Y (2), and Ni-7Co-12Cr-17Al-Y (3) overlay coatings were examined. It was found that the coating (especially cobalt-based coatings, which are more brittle than nickel-based coatings) substantially reduced the TMF life.

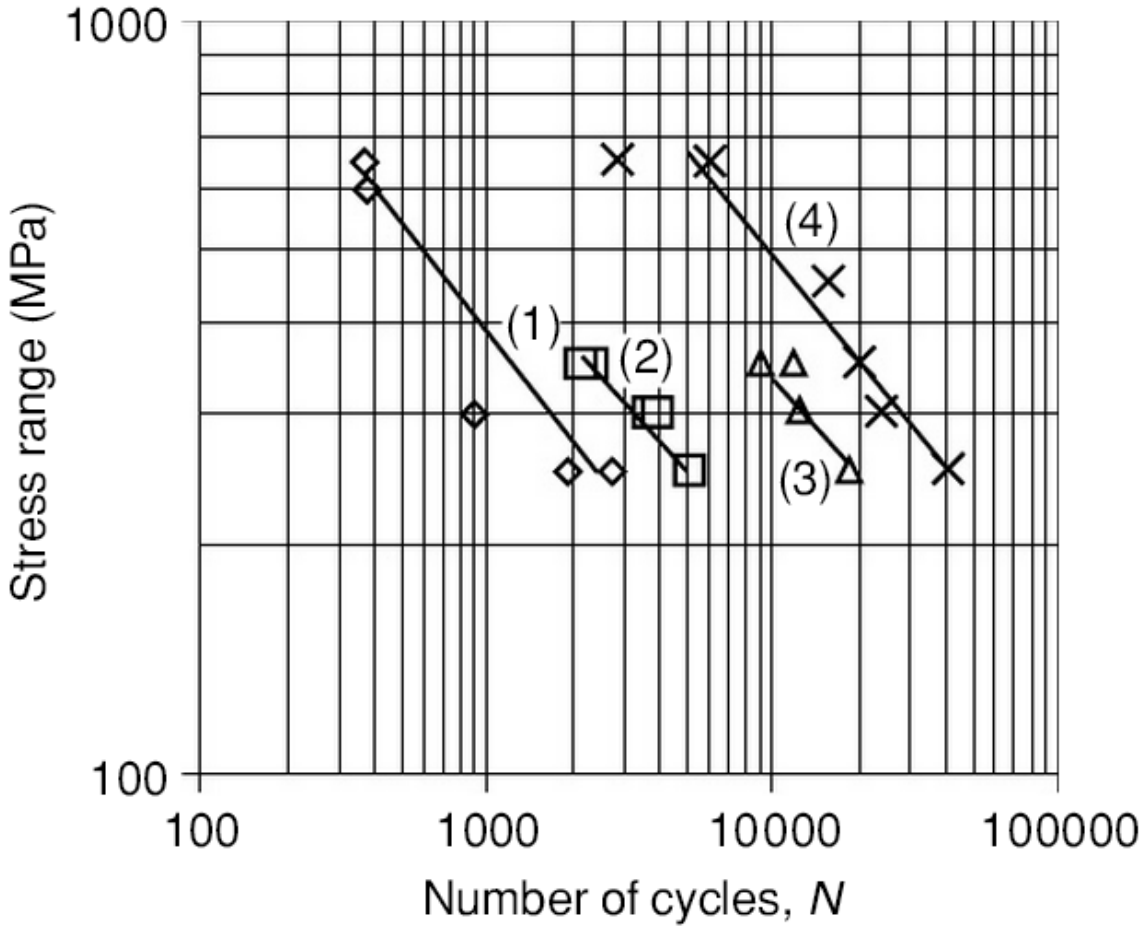

Figure 2.38: OP Load-Controlled TMF Results for CMSX-4 in the Uncoated Condition (4) and with Various Overlay Coatings (1-3) [5]

On the other hand, testing performed by Wood *et al*. [3] did not show such a deficit. Experiments were performed on IN738LC with a CoNiCrAlY coating under strain-controlled TMF between 300°C and 900°C. Although extensive cracking was observed in the coating, as shown in Figure 2.39, the resulting TMF lives of coated and uncoated specimens were not significantly different.

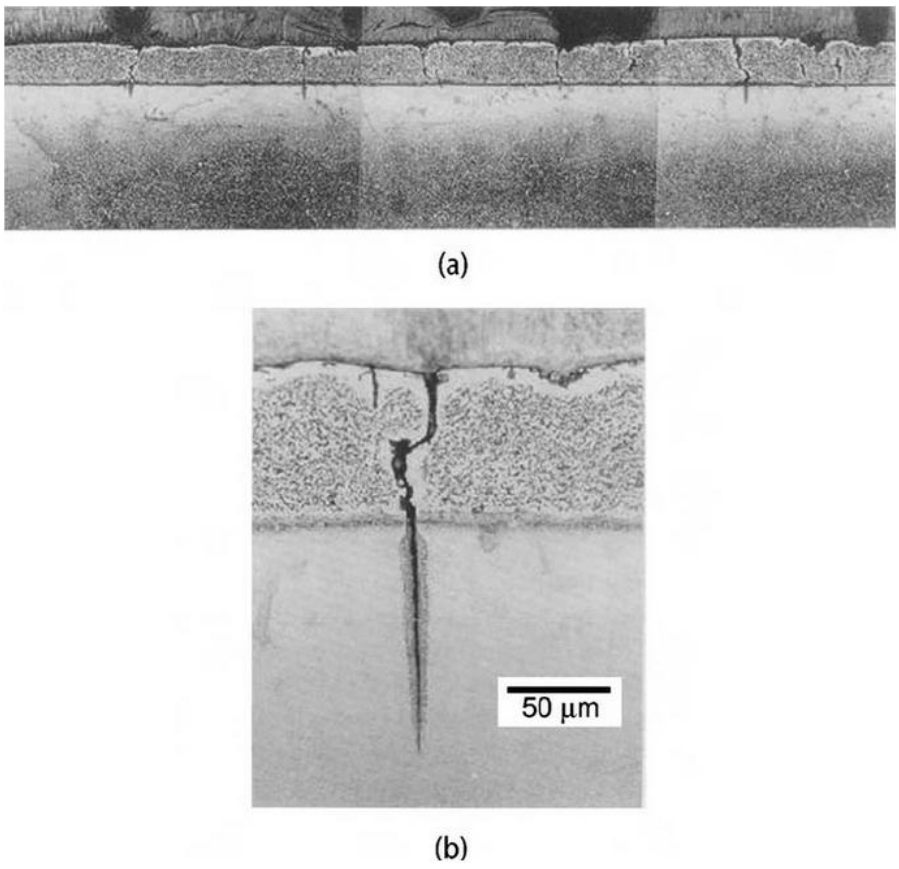

Figure 2.39: Extensive Cracking in CoNiCrAlY Overlay Coating on IN738LC Substrate after TMF Testing [3]

2.6: Behavior of Superalloys Under TMF Conditions

While isothermal fatigue is relatively straightforward and bithermal fatigue displays the interaction effects for the damage mechanisms that occur at high and low temperatures, conventional TMF can create many different damage mechanisms and interactions during each cycle [42]. Before discussing these, it is necessary to understand the general damage mechanisms for superalloys at different temperatures. At low temperatures, deformation occurs by γ' shearing because the precipitates are closely spaced. In strain-controlled fatigue tests, the stresses in annealed materials generally increase with the cycle count and then may stabilize or begin to soften. In fact, under

cyclic loading, many superalloys have been found to harden both at room temperature and at elevated temperatures [81-87]. This is the result of an increase in the dislocation density and cross-slip that restricts the dislocation motion. The hardening becomes more pronounced at higher strain levels. At higher temperatures, coarsening of the precipitates may occur, leading to lower strength. Cross-slip is enhanced, leading to the formation of fewer slip bands. Shearing of the γ' results in softening, as shown by Antolovich *et al*. [88] in René 80. At intermediate temperatures, Milligan and Antolovich [89] found that deformation in PWA 1480 occurred through a γ' bypass mechanism.

Depending on test conditions, four primary damage mechanisms occur in superalloys during TMF: creep, fatigue, creep-fatigue, and environmental-fatigue. During creep failure, cracks initiate from internal micropores [28, 90]. Creep in tension increases the mean stress, while creep in compression decreases it. Creep can be observed during in-phase TMF, but out-of-phase tests only tend to exhibit creep during a high-temperature hold time [91]. Fatigue cracks initiate at the surface of the material due to the motion of dislocations during cyclic plasticity [28, 92].

An example of damage mechanism interactions was shown by Boursier [93]. Fatigue experiments were performed on René 80 in which the material was cycled isothermally with a constant strain range for about half its expected life, and then the temperature was changed between 25°C and 760°C before cycling continued. The specimen that started at high temperature broke on the first cycle at room temperature, and it was found that the oxides formed at the high temperature were cracked by slip bands at room temperature. However, the specimen that began at room temperature and then cycled at 760°C did not fracture until the expected failure life predicted for

isothermal conditions. As a result, not only were temperature interaction effects observed, but they were found to be sequence-dependent.

The results of Boursier [93] explain why out-of-phase TMF is more damaging than isothermal fatigue or in-phase TMF. This was also shown experimentally by Gayda *et al*. [26], who conducted isothermal, in-phase bithermal, and out-of-phase bithermal fatigue experiments on bare and coated PWA 1480. The applied coating was a NiCoCrAlY coating named PWA 276. The out-of-phase lives were found to be much lower than either the in-phase or isothermal lives, confirming that these interaction effects must be at play. Therefore, out-of-phase TMF testing is used to find the limiting life of turbine components. In addition, while isothermal bare and coated results differed, the results under bithermal fatigue conditions were shown to be very similar.

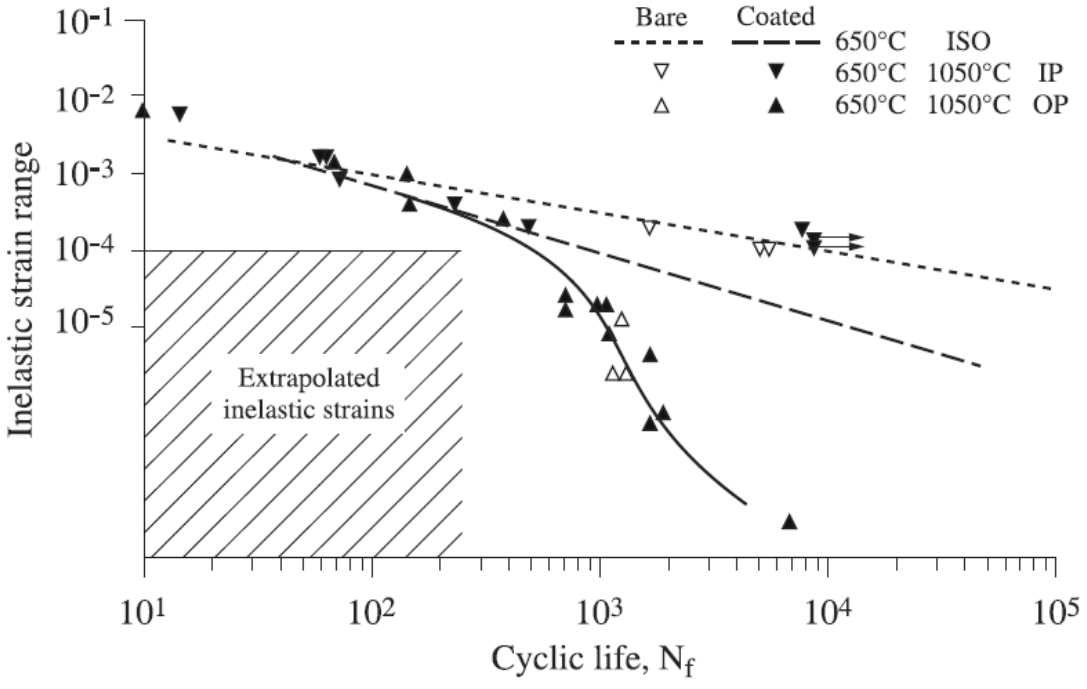

Figure 2.40: Isothermal Fatigue and IP/OP BiF Life Curves for PWA 1480 [26]

The results of TMF tests performed on PWA 1484 by Cetel and Duhl [39] are shown in Figure 2.41, where they are compared to results from PWA 1480. The material was coated with a NiCoCrAlHfSiY overlay coating, and the out-of-phase strain-controlled tests were performed at temperatures of 427-1038°C. It is believed that the increased creep resistance of PWA 1484 when compared to PWA 1480 doubled the TMF life or equivalently led to an increase of 36°C in the maximum temperature. Due to an increase in creep resistance, the mean stress during the test was not as high, leading to better performance and longer life.

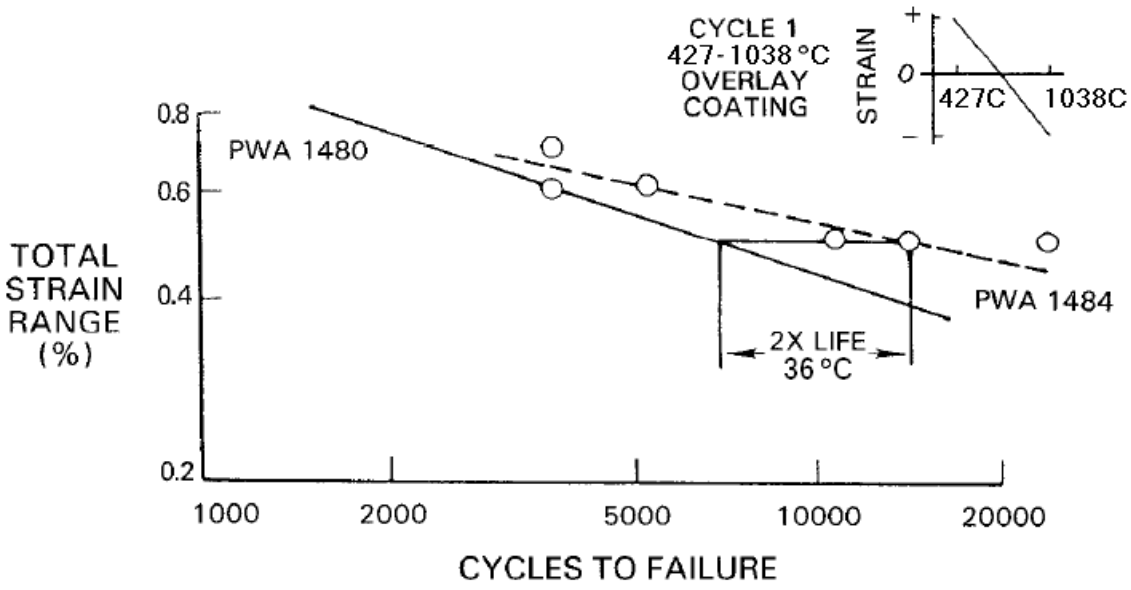

Figure 2.41: Out-of-Phase TMF Life of PWA 1480 and PWA 1484 [39]

2.7: Effects of TMF Testing Variables

2.7.1: Introduction

A myriad of factors have the possibility to influence TMF test results for identical loading conditions. Apart from the test conditions themselves, these may include factors such as specimen geometry, methods of temperature control, temperature gradients in the specimen, and phase angle, whether they are purposefully applied or if they are a result of errors in test methods. These effects have all been explored in some form, and the results are discussed below.

2.7.2: Specimen Geometry

Loveday *et al*. [94] performed a TMF inter-comparison exercise with eight inner-circle laboratories using specimens of the polycrystalline superalloy Nimonic 90 of three different geometries (solid, hollow, and flat) produced at the same workshop and ten outer-circle participants using specimens of their own in-house geometry. Tests were fully-reversed and mechanical strain controlled, and three repeat IP tests at a strain range of 0.7% along with three repeat OP tests at a strain range of 0.8% were conducted. A ramp waveform with temperatures of 400-850°C and a 180 second cycle time was used. It was found that the overall scatter was ±67% for IP tests and ±45% for OP tests. The differences in results for solid round bar, hollow, and solid flat specimens were small in comparison to the scatter, but tubular specimens typically gave slightly shorter lives than solid specimens.

Pahlavanyali *et al*. [95] performed TMF tests on both miniature and full-scale specimens of Nimonic 90 to investigate whether testing costs could be reduced. The thin

miniature specimens had a 1x1 mm cross-section in the gage section, while the full-scale specimens had a hollow geometry. Temperatures ranged from 400-850°C with a heating and cooling rate of 5°C/s, and four different phase angles were used. Tests were conducted under displacement control in such a way that the stress would be equal in both sizes of specimens. Good agreement in the TMF lives for both types of specimens were demonstrated, and the failure mechanisms were the same for both specimens.

2.7.3: Temperature

In addition to the geometry effects discussed above, Loveday *et al*. [94] also explored the effects of temperature measurement systems. Five methods of temperature measurement were employed: ribbon thermocouples, spot-welded bead thermocouples, thermocouples with individually spot-welded wires, beaded thermocouples tied on to the specimen, and sheathed thermocouples inserted into the specimen through a hole in the grip end. It was difficult to make firm conclusions due to the scatter in the data, but the ribbon and spot-welded bead thermocouples tended to have the largest scatter and lowest TMF lives, probably caused by uncertainty and underestimation of the temperature measurement. In addition, some of the laboratories also did not have the capabilities to span the entire temperature range in the given cycle time; as a result, it was found that the TMF life increased with increasing temperature range.

In a comparison experiment performed by Beck and Rau [96], similar thermocouple attachment methods, as well as optical pyrometry, were employed for temperature measurements and compared. Although none of the methods were ruled out, several recommendations were presented to ensure the best temperature reading. No

differences were observed between the readings from type R and type K thermocouples, so type K wire was recommended for temperatures up to 850°C due to the better thermo-voltage, but higher-temperature type R wire was recommended for temperatures above 900°C.

Kuhn *et al*. [97] aimed to discover the effects of defined temperature errors on the TMF test results for Nimonic 90. Out-of-phase, fully-reversed, strain-controlled tests were performed with a mechanical strain range of 0.8% and temperatures of 400-850°C with a temperature rate of 5°C/s. Both time-based and temperature-based thermal strain compensation methods were used. Tests under time-based compensation were found to be much more sensitive to temperature errors, especially at the lower temperature. An increasing temperature range decreased the life due to the extra strain supporting the mechanical loading, while a decreasing temperature range increased the life. However, the life results for temperature-based compensation tests were found to be more tolerant of temperature errors. Nevertheless, the temperature errors were found to affect the cyclic stress-strain curves.

Brendel *et al*. [98] examined the effects of thermal gradients on out-of-phase TMF results for Nimonic 90. A temperature range of 400-850°C and a fully-reversed mechanical strain range of 0.8% were employed, along with two different heating/cooling rates (5°C/s and 20°C/s) for a low thermal gradient and a high thermal gradient. It was found that the gradient had no significant effect on the life results, but finite element analysis showed that the thermal gradient may have reduced stresses in the specimen under tensile loading. In addition, the heating/cooling rate was not found to affect the test results.

On the other hand, Andersson and Sjostrom [99] performed similar experiments with heating/cooling rates of 5°C/s, 2°C/s, and 10°C/s and found different results. They found that the TMF lives of the 10°C/s tests were the longest, and the 2°C/s tests had the shortest lives, with the 5°C/s tests falling in between. It was suggested that the reason for this was the increased compressive creep for the slower heating/cooling rates, causing larger back-stress in tension; however, this result should be material-specific.

2.7.4: Phase Angle

Another set of experiments performed by Pahlavanyali *et al*. [100] explored the effect of phase angle. TMF tests on Nimonic 90 were performed under the same conditions as mentioned before [95], but phase angles of $\varphi = 0°$ (in-phase), 180° (out-of-phase), 180°±10°, 180°±20°, and 270° (counter clockwise) were all used. It was found that deviations of ±10° from the out-of-phase cycle had no significant effect on the life results, while a deviation of +20° produced higher plasticity and -20° produced lower plasticity than the out-of-phase test.

CHAPTER 3

EXPERIMENTAL METHODS

3.1: Introduction

For this work, uniaxial out-of-phase thermo-mechanical fatigue tests under mechanical strain control were performed using hollow specimens of PWA 1484. Half of the specimens were protected by a coating on the outer surface. The buttonhead specimens, shown in Figure 3.1, are optimized for testing at Pratt & Whitney labs. However, these specimens could not be used in the collet grips of the testing system present at Georgia Tech. Up to this point, all of the TMF testing performed at Georgia Tech used solid cylindrical specimens of a similar geometry to that shown in Figure 3.2. Therefore, a modified gripping mechanism had to be created.

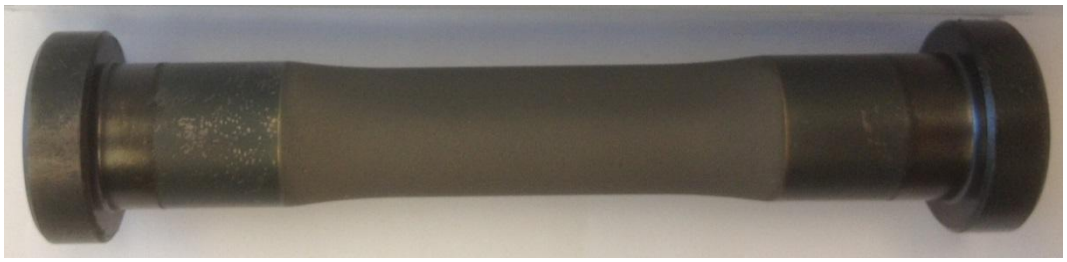

Figure 3.1: Hollow Buttonhead Test Specimen as Received from Pratt & Whitney

Figure 3.2: Solid Round Bar Test Specimen Normally Used at Georgia Tech

As a result, the ends of the specimens were modified to create a new gripping section, and a system of adapters was created to increase the gripping diameter to a standard size for the collet grips. Due to concerns about crushing the hollow specimens, plugs were also inserted into the ends. Figure 3.3 shows a visualization of the specimen with the modifications to the gripping mechanism, while Figure 3.4 shows an exploded view of the whole assembly, complete with the plugs and collet adapters. Analysis performed on these modifications predicted that they would be successful (see section 4.2 of this thesis), and in practice they have allowed for successful TMF tests using the current test machine and grips. To ensure validity of the data, the tests were performed while conforming to the requirements provided by an ASTM standard practice for strain controlled TMF testing [101].

Figure 3.3: Visualization of Modifications to Gripping Mechanism

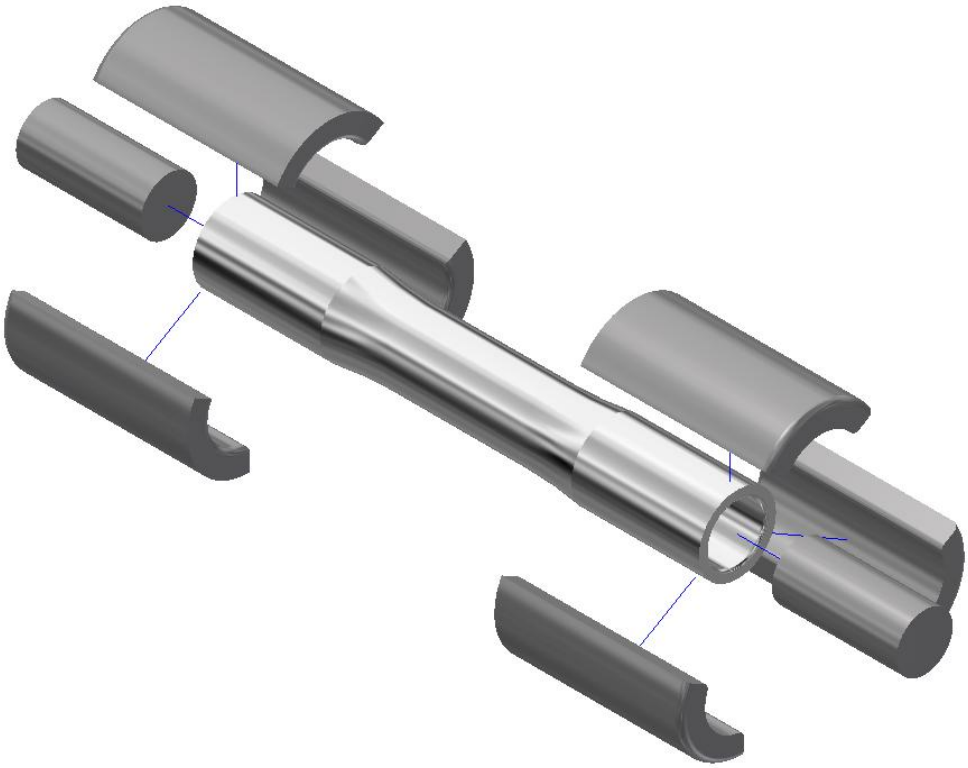

Figure 3.4: Exploded View of Modified Specimen, Plugs, and Adapters

3.2: Materials

The specimens used for testing were supplied by Pratt & Whitney and were composed of PWA 1484, a second generation single crystal nickel-based superalloy. Due to its resistance to mechanical degradation and ability to retain its properties at elevated temperatures, the material is used for components in gas turbine engines [1]. The chemical composition of PWA 1484, a cast alloy, can be seen in Table 3.1. For additional information on the microstructure and processing, refer to section 2.2.2.1 of this thesis.

Table 3.1: Nominal Composition of PWA 1484 (Weight %) [1]

Element	Ni	Co	Ta	W	Al	Cr	Re	Mo	Hf
Weight %	59.3	10.0	9.0	6.0	5.6	5.0	3.0	2.0	0.1

Turbine blades are commonly protected by a surface coating to increase the resistance to environmental damage. In practice, if the metal surface is exposed to high operating temperatures, it can experience chemical and mechanical degradation relatively quickly [1]. Of the fifteen test specimens received, seven were coated and eight were uncoated. The coating applied to the specimens is Pratt & Whitney proprietary, and as such, it could not be examined or described any further. To prevent additional differences between the specimens, the uncoated specimens underwent an identical heat treatment process as was used in the application of the coating to the coated specimens.

3.3: Specimen Design and Modification

Figure 3.5 and Figure 3.6 show the original buttonhead specimens. Several dimensions have been omitted for simplicity, but the critical dimensions are included. The drawing in original English units (along with those of all of the following drawings) can be found in Appendix A of this thesis. This specimen geometry works very well for TMF testing at Pratt & Whitney with the correct grips and cooling from internal air flow. The specimens were originally machined by Metcut Research Inc. in Cincinnati, Ohio. The quality inspection for the original specimen machining can be found in Appendix B. The tolerance allows the inner diameter to range between 1.13729 cm and 1.14808 cm, but all of the specimens received had an inner diameter smaller than 1.143 cm. Also, the outer diameter of the shank could range between 1.5621 cm and 1.5875 cm, but this dimension was greater than or equal to 1.5748 cm for all of the specimens received.

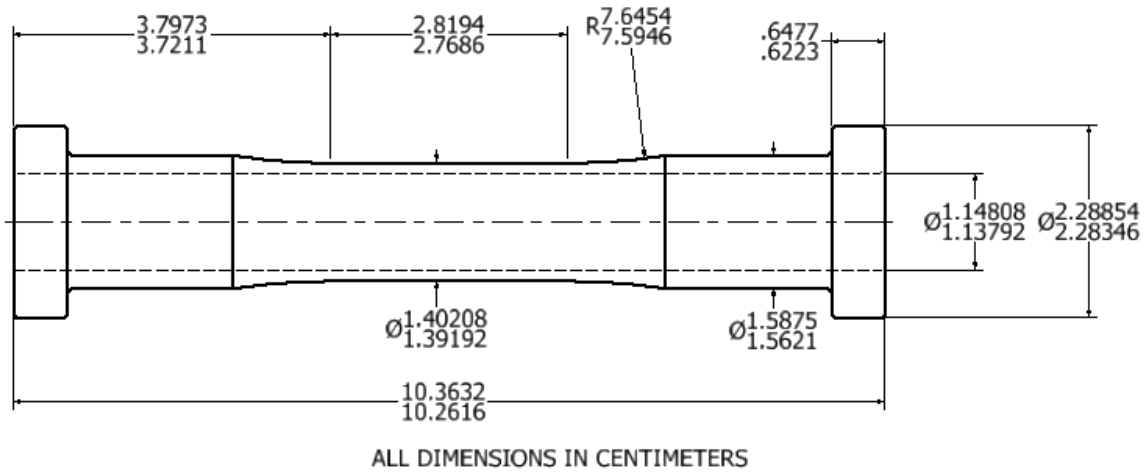

Figure 3.5: Drawing of the Original Specimen with Critical Dimensions

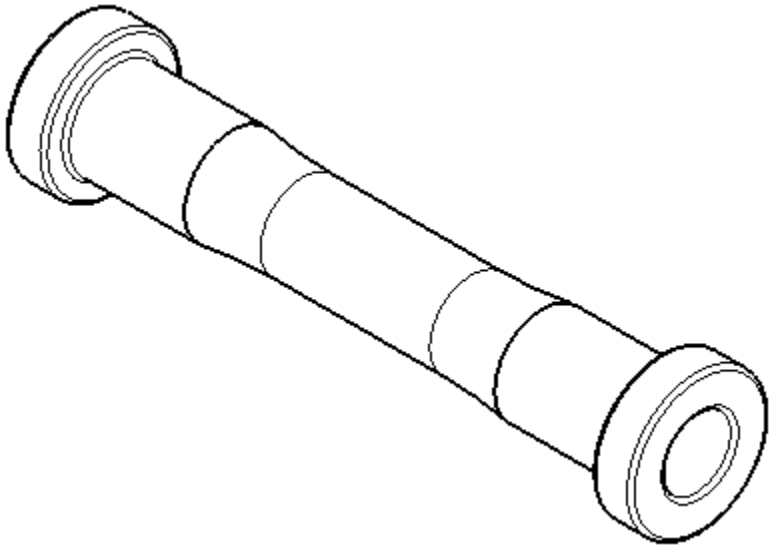

Figure 3.6: Isometric View of the Original Specimen

To accommodate the present testing equipment, the buttonheads of the specimens had to be removed, and due to the nature of the collet grips, the tolerance of the gripping section also needed to be maintained more closely. As a result, the entire shank section was machined, as shown in Figure 3.7 and Figure 3.8. Grinding down the buttonheads as opposed to cutting off the ends was a useful way to provide additional gripping force by

preserving the specimen's length. As previously mentioned, since all of the specimens were large enough, a new diameter of 1.5748 cm for the gripping section was chosen. The machining modification of the specimens was performed by Element Materials Technology in Cincinnati, Ohio. The quality inspection for this machining step can be found in Appendix B.

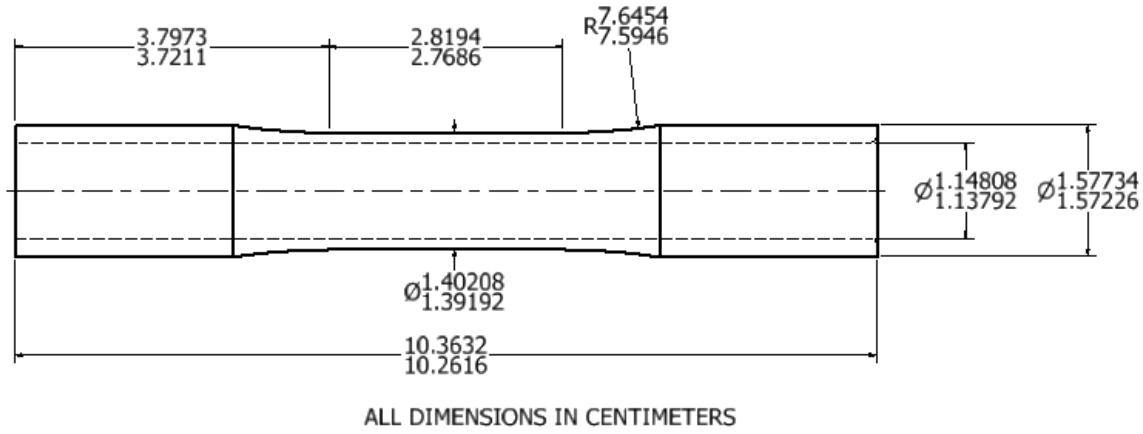

Figure 3.7: Drawing of the Modified Specimen with Critical Dimensions

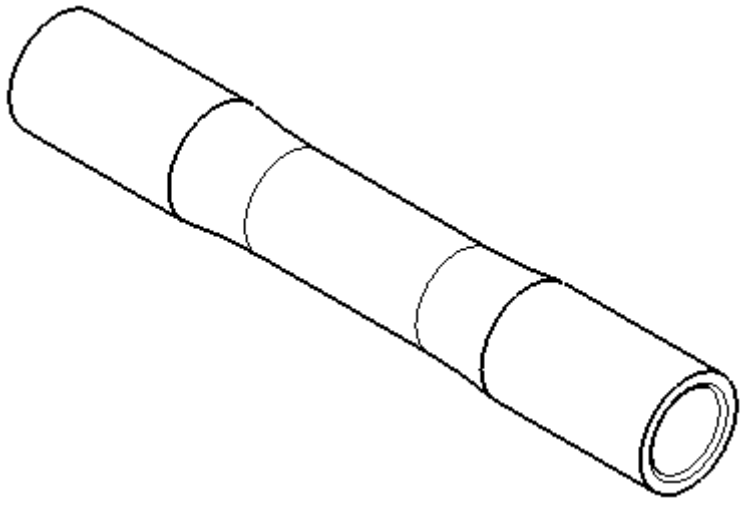

Figure 3.8: Isometric View of the Modified Specimen

3.4: Modified Gripping Method

3.4.1: Plugs

Due to concern based on previous experience with hollow specimens, plugs were inserted into the ends of the specimens using a shrink fit method to prevent crushing in the collet grips. Calculations were performed to find the stresses induced in the specimen's gripping section, and finite element models were also created to check for any stress concentrations and ensure that the gage section was not affected. In addition, the stress in the specimen that may be induced by the changing temperature of the trapped air was calculated. For detailed results of these analyses, see section 4.2 of this thesis.

Figure 3.9 shows a drawing of a plug. Based on the analysis mentioned above, the diameter needed to be slightly larger than the inner diameter of the specimen (ideally rounded up to the nearest thousandth of an inch, or within an increment of 0.0254 mm) for this insertion method. The 2.54 cm length of the plugs was chosen such that they almost reach the point where the specimen starts to neck down towards the gage section while sitting flush with the end. The leading edge of the plug could have also been filed off for easier insertion, although this was not performed in this case.

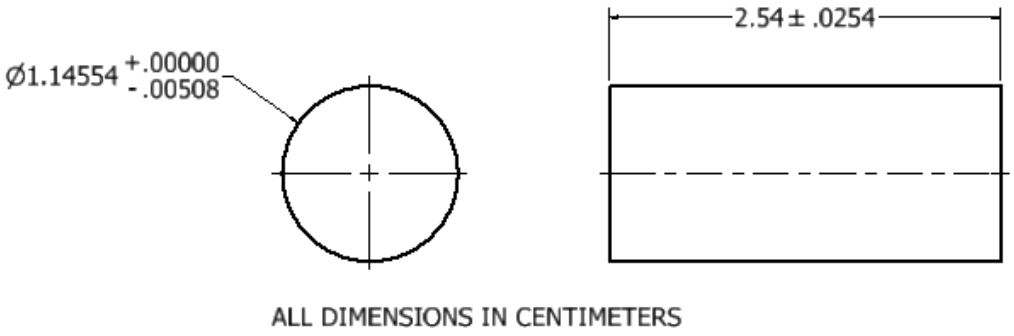

Figure 3.9: Drawing of a Plug

Ideally, the plugs also would have been made from PWA 1484 or another superalloy with a very similar coefficient of thermal expansion to that of the specimens in order to prevent possible expansion mismatches during the thermal cycling of the TMF tests. However, for ease of machining and economic considerations, the plugs were produced from steel. During testing, the water-cooling of the gripping section and the large applied clamping force prevented any problems.

A burr existed on the inner edge of the ends of most of the specimens, so it was originally thought that the holes were smaller than they were in actuality. The burrs were removed with a manual deburring tool before proceeding. The shrink fit was performed using a dry ice and alcohol bath, although it could have been easier to use a cooling agent such as liquid nitrogen. The plugs were placed in the bath for 10-15 minutes and then slid into one end of the specimen. The assembly was allowed to return to room temperature to ensure a stable fit before proceeding with the other end of each specimen. For some of the largest plugs, the bath alone did not provide enough of a temperature difference to adequately shrink the plug; in these cases, the specimen was placed in an oven and heated to 200°C for 5-10 minutes before finally performing the fit. Figure 3.10 shows two specimens (one uncoated and one with the coating) after the completed machining modifications and with plugs inserted. As previously mentioned, the uncoated specimens underwent an identical heat treatment used during the application of the coating, which caused the darker color of the surface of the material away from the machining modifications.

Figure 3.10: Uncoated (Left) and Coated (Right) Specimen After Modifications

3.4.2: Collet Adapters

After modifying the specimens, adapters for the collet grips were produced to allow the specimens to be gripped by 2.54 cm diameter collets. Figure 3.11 is a drawing of one of the adapters. The inner radius was dictated by the chosen outer diameter of the specimen gripping section, and the outer radius was dictated by the chosen size of collet grips. The height of the adapters was chosen to be the same as the height of the gap in the collet grips so that the top edge could easily and uniformly sit flush with the top of the collets. The adapters were machined by wire EDM from a plate of alloy A-286 steel, an iron-nickel base superalloy. This material was selected due to its relatively high strength.

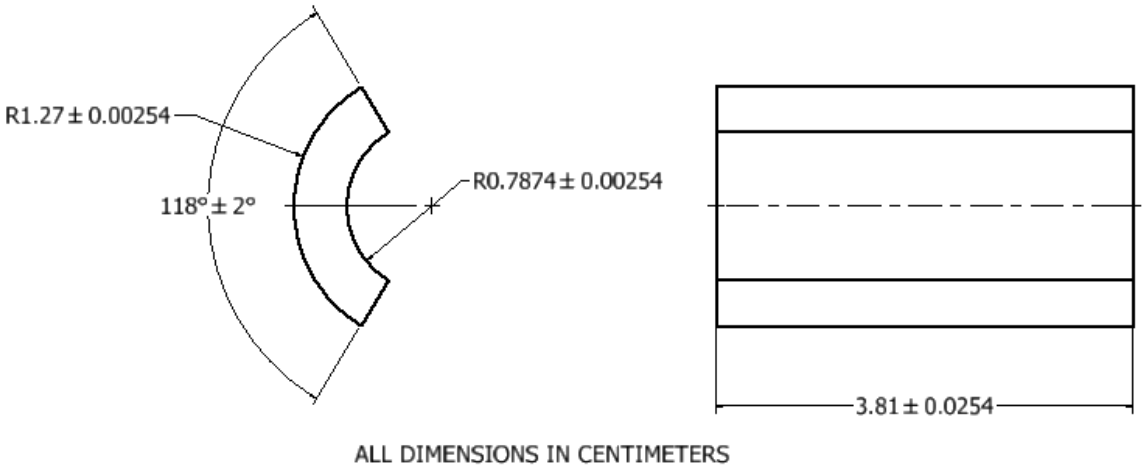

Figure 3.11: Drawing of a Collet Adapter

To allow the adapters to be easily inserted into the grips and the specimen to be more easily inserted into the adapters, as well as to reduce stress concentrations on the specimen, certain edges of the adapters were filed down by hand. As shown in Figure 3.12, these edges include the outside bottom edge (making first contact with the collet grips), the top inside edge (making first contact with the specimen), and the two inside vertical edges that may dig in to the specimen.

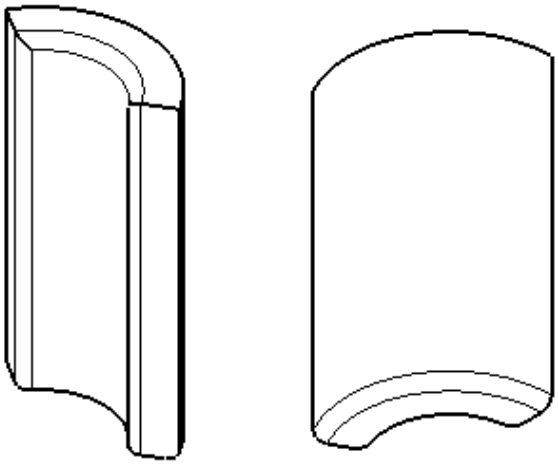

Figure 3.12: Views of Collet Adapter with Filed Edges

Three of these adapters were placed inside each grip around the specimen to match up with the three pieces of the collet. It is important to note that the uniformity of these adapter pieces is extremely critical to avoid alignment issues during the gripping of the specimen, which could lead to the unintended application of a bending moment. Also, it is important to make sure that the longitudinal flat surfaces of all three adapters do not make contact with each other when clamped (meaning that they do not span a complete 360 degrees), or the specimen may slip out during the TMF testing due to the interference resulting in insufficient clamping force. This problem actually occurred during initial verification; to correct this problem, the edges of the adapters were ground down to make sure each one spanned less than 120 degrees. Figure 3.13 shows a modified specimen in the test frame being successfully gripped by the adapted collet system.

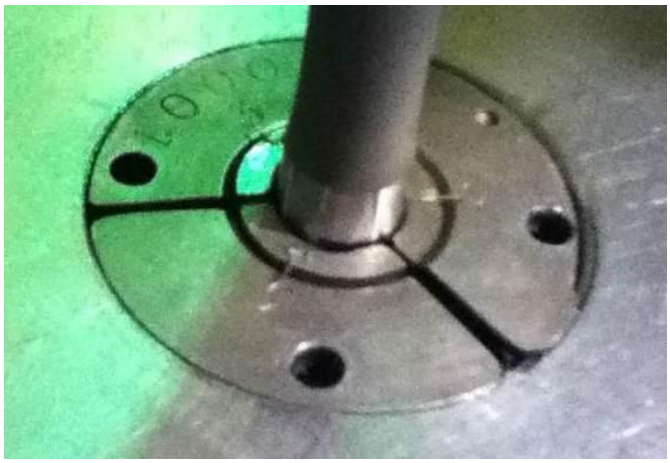

Figure 3.13: Specimen Gripped by Collet with Adapters

3.4.3: Clamping Force Analysis

Calculations were performed in order to determine the theoretical grip pressure necessary to apply the desired loads. Each of the following equations and constants

(Equation 3.1, Equation 3.2, A, $\mu_{g\text{-}c}$, and C_R) were found in the equipment manual for the grips [102]. First, the clamping pressure that had been applied to the round bar specimens in previous experiments was determined. A grip supply pressure P of 20.68 MPa had been used. The specimens were 1.27 cm in diameter at the ends and were inserted 1.778 cm into the grips, giving a gripping area of 7.094 cm^2. The clamping force F_c is determined from Equation 3.1,

$$F_c = PA\left(\frac{\cos 15° - \mu_{g-c}\cos 75°}{\cos 75° + \mu_{g-c}\cos 15°}\right) \tag{3.1}$$

where A = 60.7 cm^2 is the area of the grip piston and $\mu_{g\text{-}c}$ = 0.06 is the coefficient of friction between the grip and collet. An original clamping force of 376.7 kN was determined, and when divided by the gripping area, the clamping pressure was determined to be 531.0 MPa.

For these experiments on the hollow specimens, the collet grip adapters had an outer diameter of 2.54 cm, and the ends were inserted 1.651 cm into the grips, giving a gripping area of 13.17 cm^2. In order to obtain the same clamping pressure as the round bar specimens, it is found that the required clamping force is 699.6 kN. Using Equation 3.1, the required grip supply pressure is found to be 38.41 MPa. This value was attainable, as the maximum supply pressure to the grips is 44.82 MPa.

In order to ensure that the calculated grip supply pressure would be sufficient, another calculation was performed. At 760°C, the ultimate tensile strength of PWA 1484 is at a maximum value of 992 MPa [103]. Therefore, for the specimens' cross-sectional area of 2.027 cm^2, the maximum applied axial load L would be 18.65 kN. The required grip supply pressure can be predicted by Equation 3.2,

$$P = \left(\sqrt{L^2 + \left(\frac{2T}{D} \right)^2} \right) C_R \tag{3.2}$$

where T is the applied torque, D is the specimen diameter, and C_R = 0.422 MPa/kN is a constant value for round specimens. As an axial-torsion machine was used but no torque was applied to the specimen, T = 0. This equation predicts that a grip supply pressure of 21.21 MPa would be sufficient, although it was finally decided that P = 38.41 MPa from the previous calculation would be used since it provided some measure of safety and conservatism.

3.5: Equipment

Tests were performed using an MTS axial/torsion closed-loop servohydraulic test frame with model 204.63 100 kN axial actuator. The tests were controlled using an MTS FlexTest 40 digital controller and Multipurpose Elite software. The specimens were gripped with water-cooled MTS 646.10 A/T collet grips for 25.4 mm round specimens.

The specimens were heated using an Ambrell EASYHEAT 0224 induction heating system. The seven-turn inductive coil was formed using 4.7625 mm diameter copper tubing. The heater was controlled using a Eurotherm 3204 temperature/process controller. The temperature of the specimen was measured through a thermocouple welded to the specimen; 30 AWG type K wire, 24 AWG type K wire with high temperature glass sheathing, and 30 AWG type R wire were each used at some point during the testing. The thermocouples were spot welded to the specimen using a Unitek spot welder with model 1-163-02 spot welder control. For preliminary temperature

experiments with multiple thermocouples, the temperatures were read using an OMEGA model 199 digital temperature indicator.

Axial strain was measured using an MTS 632.53E-14 extensometer with 3.5 mm diameter ceramic rods that were 11.43 cm long. The ends of the rods were sharpened using a 26.9875 mm diameter grinding wheel at a 30° angle such that the tip of the rods conformed to the outer diameter of the specimen gage section. The extensometer has an operating range from +20% to -10% strain, and it was calibrated periodically to a range of ±5% strain.

Figure 3.14 shows the experimental setup for the TMF testing. The test specimen can be seen in the collet grips (with adapters) surrounded by the induction coil. The extensometer can also be seen in its mounting apparatus and attached to the front of the specimen through the gaps in the seven-turn coil.

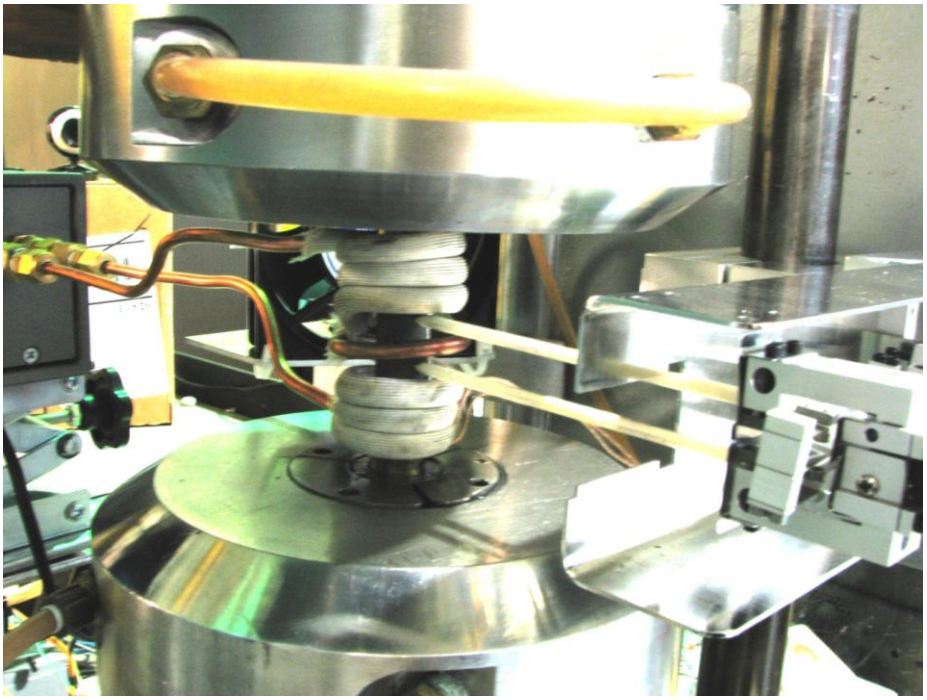

Figure 3.14: TMF Test Setup

3.6: Testing Procedure

3.6.1: Overview of TMF Test Procedure

Prior to beginning the TMF test setup, the surfaces of the collet grips, adapters, and specimen gripping section were cleaned with ethanol while the test machine was warming up. A thermocouple was spot welded to the top of the specimen just outside of the gage section (3.686 cm from the end of the specimen) for temperature control. If necessary, the specimen surface was gently exposed using P4000 grit grinding paper. The wire was fed towards the top of the specimen and secured at the edge of the gripping section underneath two pieces of nickel wire that were welded to the surface at that location. A picture of the type R thermocouple secured to the specimen is shown in Figure 3.15. The rationale for the location of the thermocouple is explained later in section 3.7.2.1.

Figure 3.15: Thermocouple Attachment to Specimen

The specimen was then inserted into the test machine. First, with ample space between the top and bottom grips, three collet adapters were held in place in the top grip by hand while inserting the specimen 1.651 cm until it was manually tightened. A view of the specimen with the thermocouple wire positioning after it was inserted into the top grip can be found in Figure 3.16. Next, the bottom grip was set in the desired position, and three more collet adapters were placed inside and positioned so that they were flush with the top surface of the grip. With the specimen moving through the induction coil, the top grip was carefully brought downwards while making sure the alignment was correct until the specimen was inserted 1.651 cm into the bottom grip. Then, the bottom grip was manually tightened, and the supply pressure to both grips was turned on.

Figure 3.16: Front View of Specimen after Insertion into Top Grip

The coil was then centered around the specimen, and the extensometer was put in place. Several non-damaging force-controlled cycles were run at a frequency faster than the actual test frequency to ensure that the extensometer rods were not slipping. Under force control, the elastic modulus of the specimen was measured at room temperature, along with the minimum, mean, and maximum temperature for the TMF test. If necessary, the values of the Porportional-Integral-Derivative (PID) gains of the temperature controller were adjusted to obtain a stable temperature in order to record an accurate modulus.

Next, as the tests were all performed under mechanical strain control, the thermal strain compensation was performed. Several thermal cycles under zero force were performed while the temperature vs. strain response was observed until a stable response was achieved. As it was ideal that no thermal strain hysteresis exist, the PID values of the controller and the position of the coil were adjusted until the thermal strain response was satisfactory. A fourth-order polynomial was fit to the temperature vs. strain response to model the thermal strain, and the mechanical strain was calculated as the difference between total strain and thermal strain. To check the accuracy of the thermal strain compensation, a thermal cycle under zero mechanical strain was performed, and the resulting maximum and minimum loads on the specimen were observed and compared to allowable limits.

After the test procedure was edited for the appropriate mechanical strain range, the actual test could be initiated. A much more detailed step-by-step list for the testing procedure can be found in Appendix C. The test ended either when the specimen fractured or when it was stopped manually after a sufficient drop in tensile load suggested

that a crack had initiated and propagated in the specimen. After the TMF test was completed, the specimen was inspected, and if applicable, the fracture surface or gage section was more closely examined under a microscope. Finally, the data files for the tests were processed and analyzed using MATLAB.

3.6.2: Changes to TMF Test Procedure

Throughout this project, a few changes to the testing procedure were implemented, mostly related to the thermocouples. Initially, in addition to the control thermocouple, a second auxiliary thermocouple was also welded to the specimen just below the gage section (3.683 cm from the end of the specimen). However, this was eliminated to prevent the possibility of crack initiation at this location. The wire from the control thermocouple at the top of the specimen also initially ran downwards through the bottom of the coil, but it was redirected upwards in order to prevent the sheathing from burning, which would cause degradation of the actual thermocouple wire. To accomplish this, a single piece of nickel wire was used at first, but a second piece was added to ensure that the thermocouple wire was secured and could not wiggle in either direction. Finally, for the first few experiments, type K (nickel-chromium vs. nickel-aluminum) thermocouple wire was used, but type R (platinum-13% rhodium vs. platinum) wire was later implemented due to its resistance to degradation and associated longer life at higher temperatures.

3.6.3: Attempt at an Alternate Method of Thermocouple Attachment

To avoid any potential damage to the specimen resulting from spot welding the thermocouple wire, an alternate non-welding thermocouple attachment method was explored. As a small region of the coating needed to be removed in order to weld to a coated specimen, the idea initially stemmed from the desire to leave the coating intact so that no part of the surface of the specimens would be exposed. An experiment was performed to determine if it was feasible to tie on a beaded thermocouple to the surface of the specimen. For this experiment, using type K thermocouple wire, a thermocouple was welded to the specimen, and a separate thermocouple bead was also formed and tied on to the specimen directly next to the weld using wire with high temperature glass sheathing. Using the welded thermocouple as the control, the temperature reading from the tie-on thermocouple was examined over a temperature range of 427°C to 1050°C. The welded thermocouple temperature was set to 50°C increments between 550°C and 1050°C, as well as to 427°C, 732°C, and 1038°C. The end goal was to create a correlation between the readings from the welded thermocouple and the tie-on thermocouple so that the tie-on method could be used for temperature control of further TMF testing. The experiment was set up and dismantled three separate times to check for repeatability and to try to obtain a relationship between the two temperature readings that was as accurate as possible.

Figure 3.17 shows the tie-on thermocouple readings for the three experimental setups as a function of the welded thermocouple temperature, while Figure 3.18 displays the difference between the two thermocouple readings across the temperature range that was examined. While the reading from the tie-on thermocouple was always lower than

the welded thermocouple, it was found that the temperature difference was large and not constant. In addition, neither the correlation between the two readings or the temperature difference was linear, and neither curve followed the same shape across the different setups. The tie-on thermocouple temperature was also fairly inconsistent between the three experimental setups, so it was determined that this thermocouple attachment method was not completely repeatable and had a fairly large dependence on certain aspects of the setup. As a result, it was decided that the tie-on method of thermocouple attachment was not feasible and could not be used for TMF testing.

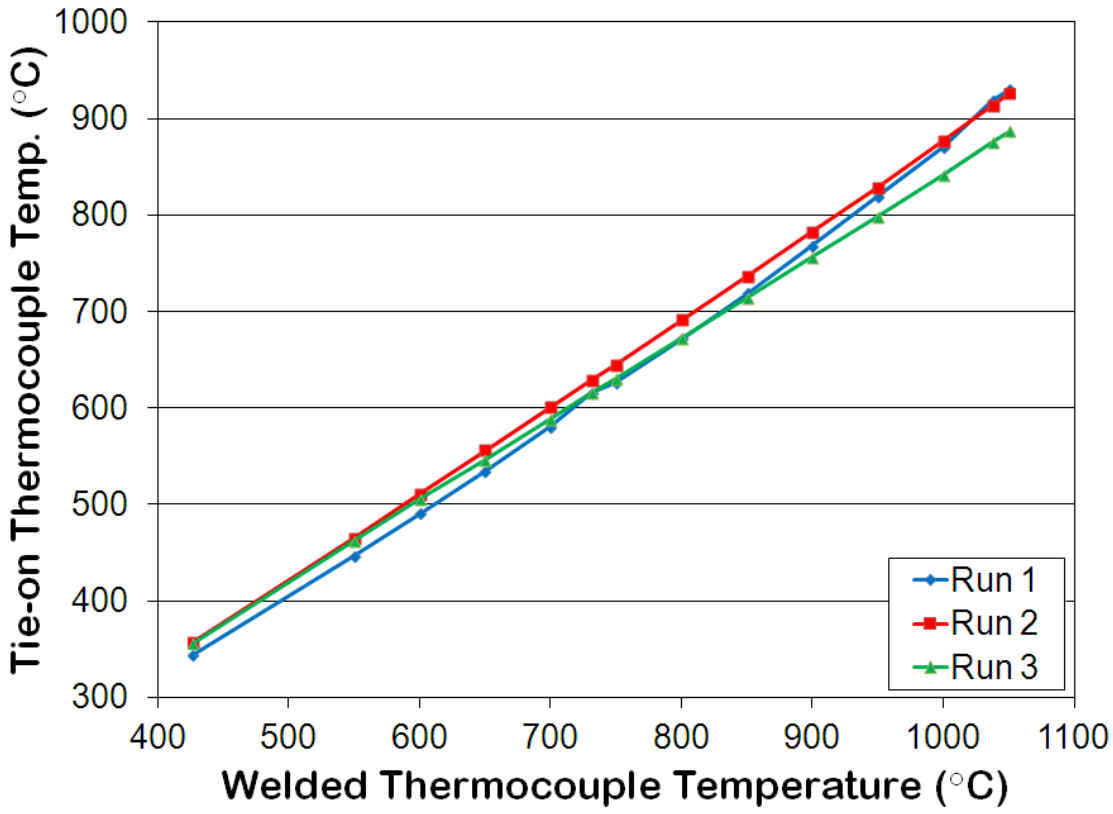

Figure 3.17: Tie-On Thermocouple Temperature Models

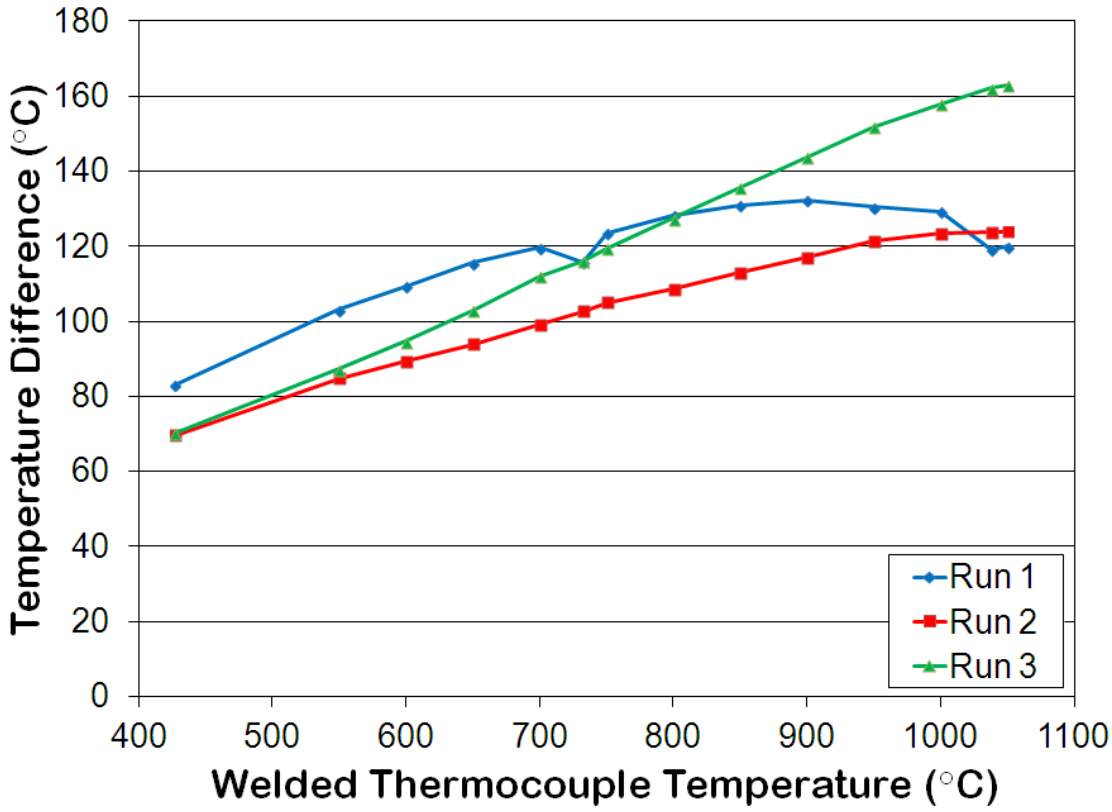

Figure 3.18: Temperature Difference Between Thermocouple Attachment Methods

3.7: Standardized Testing Practice

3.7.1: ASTM Criteria

3.7.1.1: Introduction of Testing Standard

The TMF tests for this work were performed in such a way as to conform to ASTM E2368 – Standard Practice for Strain Controlled Thermomechanical Fatigue Testing [101]. This standard practice governs uniaxially-loaded strain-controlled tests in which temperature and strain fields are simultaneously and independently varied with constant phasing. It covers all the aspects of TMF testing, including the terminology,

equipment, specimens, test procedure, and data reporting. The main requirements for the test procedure to ensure test validity are summarized in the following sections.

3.7.1.2: Specimen Temperature

At any given time during the TMF cycle, the maximum allowable axial temperature gradient in the gage section of the specimen is either 1% of the maximum cyclic temperature T_{max} (in Kelvin) or ± 3 K (whichever quantity is greater). Also, the maximum allowable transverse temperature gradient in the gage section is either 1% of T_{max} (in Kelvin) or ± 7 K (whichever quantity is greater).

In addition, the accuracy of the cyclic temperature control should be checked by examining the amount of hysteresis in the thermal strain (ε_{th}) response with the specimen held at zero force. The thermal strain hysteresis at any given temperature point should be no greater than 5% of the total thermal strain range over the temperature cycle.

3.7.1.3: Thermal Strain Compensation and Mechanical Strain

At any time during the test, the mechanical strain ε_{mech}, or the difference between the total strain and the compensating thermal strain, should not deviate from the desired value by more than 2% of the mechanical strain range $\Delta\varepsilon_{mech}$. The accuracy of the thermal strain compensation technique should also be checked before test initiation by performing a thermal cycle under strain control with zero mechanical strain. For an out-of-phase TMF test, the maximum and minimum allowable stresses during this cycle are calculated using the moduli at the corresponding temperatures as shown below in Equations 3.3 and 3.4,

$$\sigma_{max} = 0.02 \cdot (\varepsilon_{mech})_{max} \cdot E(T_{min}) \quad (3.3)$$

$$\sigma_{min} = 0.02 \cdot (\varepsilon_{mech})_{min} \cdot E(T_{max}) \quad (3.4)$$

such that the allowable stress magnitude during the cycle is equal to $(\sigma_{max}-\sigma_{min})/2$.

3.7.1.4: Temperature/Mechanical Strain Phasing

The error in the phasing between the temperature and mechanical strain should not exceed $\varphi \pm 5°$, where φ is the desired phase shift for the test. There should be no cumulative error throughout the duration of the test.

3.7.2: Procedures to Ensure Test Validity

3.7.2.1: Temperature Gradient

Before testing began, ten thermocouples (TCs) were welded to a single specimen in order to verify the temperature distribution induced by the induction coil. Seven TCs were attached along the length, and three additional TCs were attached circumferentially at the midpoint of the specimen. Figure 3.19 shows the locations and numbering scheme used in the following measurements. The TCs numbered 2 and 6 are slightly outside of the gage section, and the TCs numbered 3 and 5 encompass the 1.27 cm distance that lie between the extensometer rods.

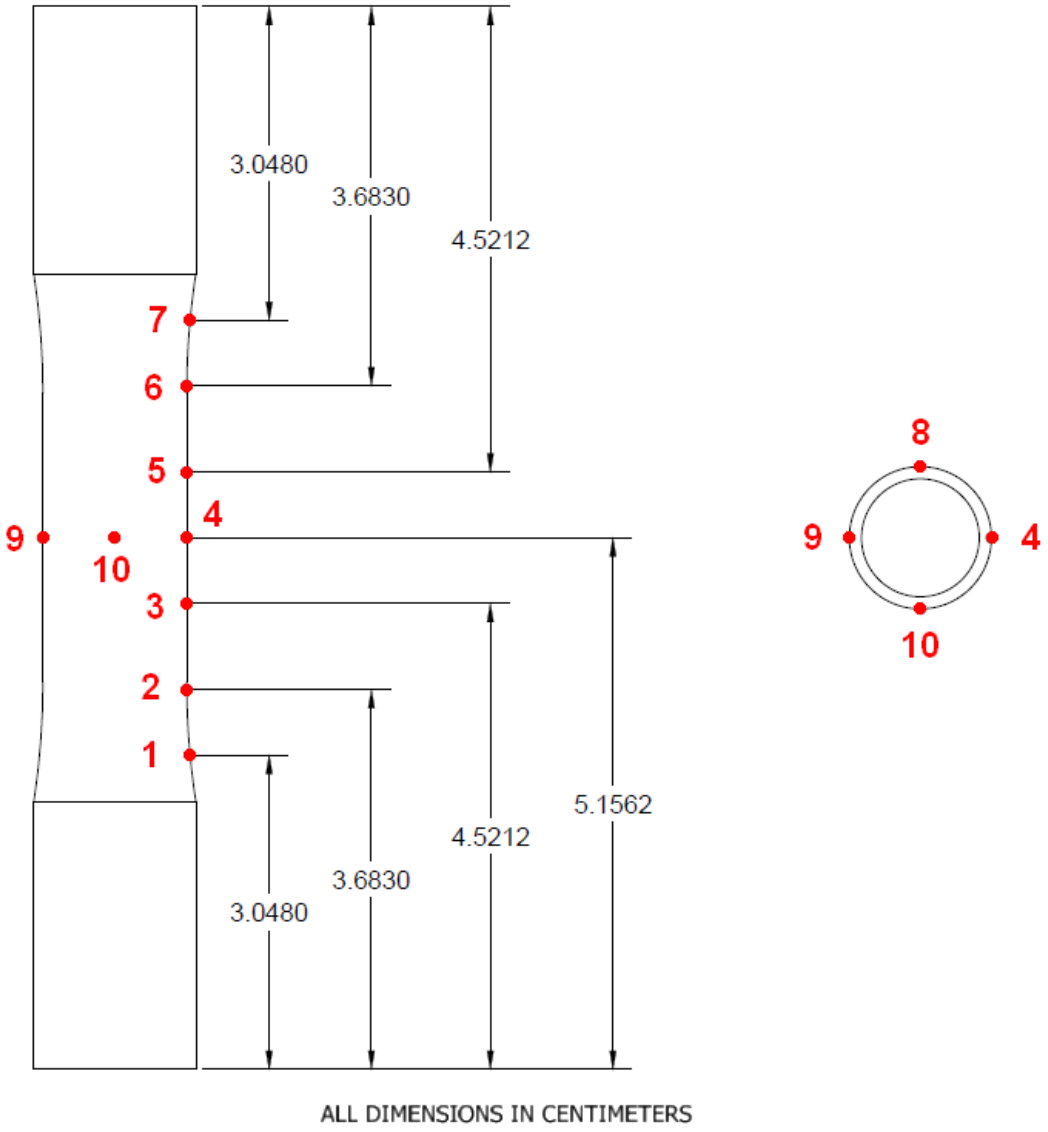

Figure 3.19: Thermocouple Locations for Temperature Gradient Testing

The specimen was inserted into the test machine, and the induction coil was centered around the specimen. First, TC 4 was used as the feedback for the temperature controller. The temperature distribution was observed and recorded at control setpoints of 550°C, 800°C, and 1050°C. The results are displayed in Table 3.2. An "x" in the column marked "Pass" indicates that the temperature at that location falls within the allowable variation specified by the ASTM standard.

Table 3.2: Temperature Distribution with TC 4 as Control

TC	TC Temperature Reading (°C)					
	550°C		800°C		1050°C	
	Temp.	Pass	Temp.	Pass	Temp.	Pass
1	451.7		712.8		996.1	
2	523.9		797.8	x	1076.7	
3	550.6	x	811.1		1082.2	
4	550.0	x	800.0	x	1050.0	x
5	554.4	x	817.8		1079.4	
6	542.8	x	810.0	x	1090.0	
7	440.6		678.3		931.1	
8	555.6	x	813.9		1070.0	
9	553.3	x	805.6	x	1058.9	x
10	542.2	x	792.2	x	1037.2	x

As the actual TMF tests are controlled by a TC outside of the gage section, it was decided that TC 6 would be the control location for the remainder of the tests. The temperature distribution was checked again with the new control TC with setpoints of 427°C, 550°C, 800°C, 1038°C, and 1050°C. Only the temperatures within the gage section were recorded, and the results can be found in Table 3.3.

Table 3.3: Temperature Distribution with TC 6 as Control

TC	TC Temperature Reading (°C)									
	427°C		550°C		800°C		1038°C		1050°C	
	Temp.	Pass	Temp.	Pass	Temp.	Pass	Temp.	Pass	Temp.	Pass
3	427.8	x	551.1	x	800.6	x	1035.6	x	1047.2	x
4	425.0	x	547.8	x	790.0	x	1015.6		1028.9	
5	432.8	x	557.8	x	803.3	x	1035.0	x	1046.7	x
6	427.0	x	550.0	x	800.0	x	1038.0	x	1050.0	x
8	433.9	x	556.7	x	797.2	x	1028.3	x	1040.0	x
9	432.8	x	557.2	x	796.1	x	1023.3		1034.4	
10	422.8	x	542.8	x	787.2		1007.2		1027.8	

The temperature setpoints were then adjusted until each of the recorded temperatures within the gage section fell within the allowable variation specified by the ASTM standard. Table 3.4 shows the final temperature distribution. The setpoint for each desired temperature can be found as the temperature reading for TC 6.

Table 3.4: Adjusted Temperature Distribution Results

	TC Temperature Reading (°C)									
	427°C		**550°C**		**800°C**		**1038°C**		**1050°C**	
TC	**Temp.**	**Pass**	**Temp.**	**Pass**	**Temp.**	**Pass**	**Temp.**	**Pass**	**Temp.**	**Pass**
3	423.9	x	547.8	x	801.1	x	1047.2	x	1060.6	x
4	427.2	x	550.6	x	796.1	x	1034.4	x	1047.8	x
5	433.9	x	557.8	x	810.0	x	1051.1	x	1062.8	x
6	422.0	x	545.0	x	797.0	x	1049.0	x	1065.0	x
8	433.9	x	557.8	x	805.6	x	1044.4	x	1059.4	x
9	430.0	x	551.7	x	797.8	x	1035.0	x	1046.7	x
10	421.7	x	542.2	x	790.0	x	1025.6	x	1037.8	x

3.7.2.2: Thermal Strain

During setup of each test, stress-free thermal cycling in force control was performed to examine the thermal strain hysteresis. A representative hysteresis loop for a 180 second cycle is shown in Figure 3.20. The temperature vs. strain curve was recorded, and if the widest gap in the hysteresis loop at any given temperature was larger than 5% of the total width (the difference in strain between the minimum temperature and the maximum temperature), the PID values of the temperature controller were altered or the position of the induction coil was slightly adjusted until the hysteresis loop was considered satisfactory. A fourth-order polynomial was then used to fit the thermal strain

as a function of temperature so that the mechanical strain could be calculated as the difference between total strain and thermal strain.

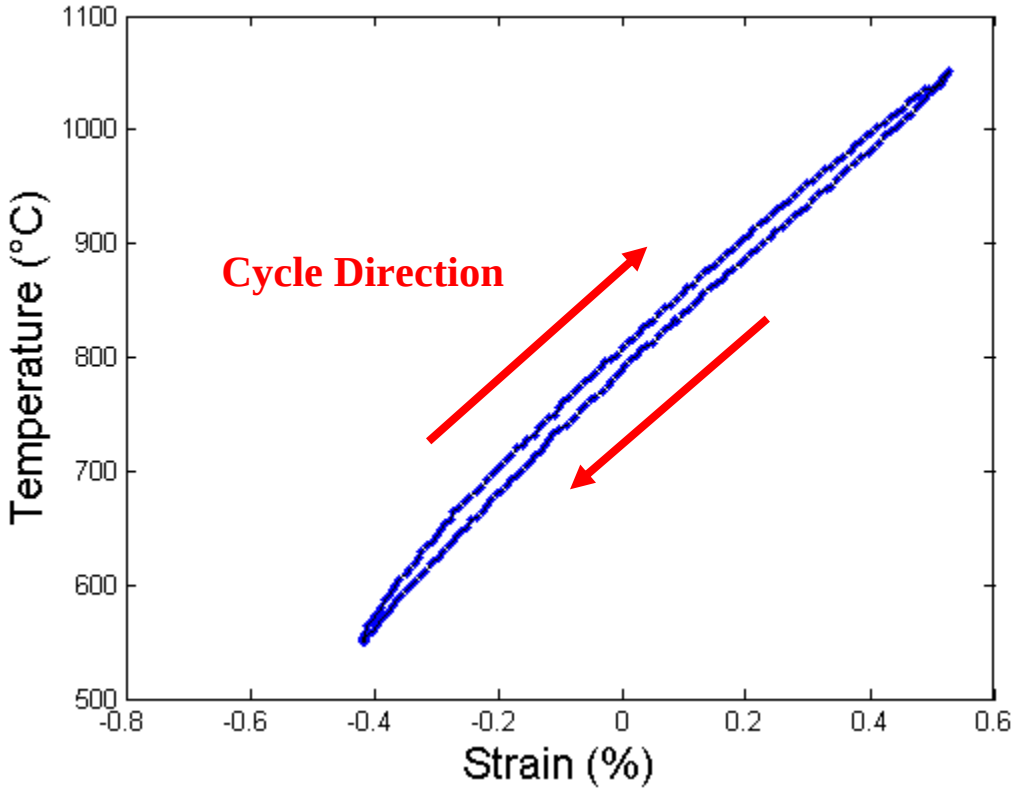

Figure 3.20: Representative Stress-Free Thermal Strain Response

When the actual test was started, two more stress-free thermal cycles were conducted while ensuring that the calculated mechanical strain was minimized. The data from these cycles was then analyzed more closely using MATLAB. A tenth-order polynomial was fit to each side of the hysteresis loop, and the two curves were used to verify that the thermal strain hysteresis criterion was indeed met.

3.7.2.3: Phase Angle

The phasing between the temperature and the mechanical strain was examined during the setup of the test. As the actual temperature signal exhibited a lag behind the control signal, a delay in the mechanical strain control signal was implemented at the start of the TMF cycling so that the two signals reached their peaks at the same time. After the test, cycles near the beginning and the end of the test were examined to ensure that the signals remained within the allowable 5° phase error. MATLAB code was used to find and compare the time at which each signal reached its peaks. The phasing of a representative out-of-phase 180 second TMF cycle is shown in Figure 3.21.

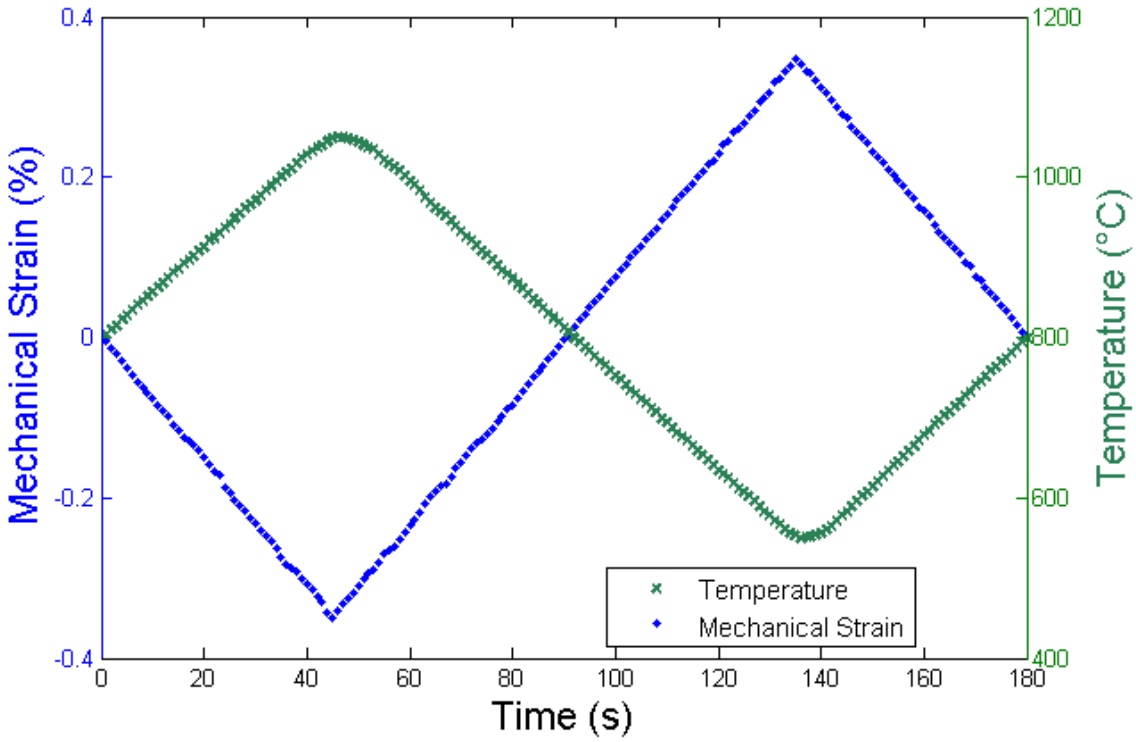

Figure 3.21: Representative Out-of-Phase TMF Cycle

3.7.2.4: Mechanical Strain Deviation

During the setup of the test, after the polynomial was fit to the thermal strain, a thermal cycle under mechanical strain control with zero mechanical strain was performed to verify the accuracy of the thermal strain compensation. The maximum and minimum stresses induced during the cycle were calculated and compared to the established allowable stress range.

In addition, during the test, the mechanical strain control signal was collected along with the actual response. After the test, a MATLAB script was used to ensure that the actual mechanical strain had not deviated from the control point at any time during the test by more than the allowable amount of 2% of the total mechanical strain range.

3.8: Failure Criteria

For previous TMF tests on PWA 1484 conducted at Georgia Tech by Amaro [14], the failure criterion corresponding to crack initiation was desired to be linked to the microstructure of the material to better represent a physics-inspired life estimation model. The crack length corresponding to crack initiation was decided to be equal to the dendrite spacing of the material, which was found to be 0.178 mm, as shown in Figure 3.22. For the solid specimens used for the tests (a drawing can be found in Appendix A), it was found that the ratio of the initial cross-sectional area to the cracked cross-sectional area would be equal to 0.996. This scenario is represented schematically in Figure 3.23. Therefore, failure was defined as the point in time at which the tensile load carrying capabilities of the specimen dropped by 1% for two consecutive cycles.

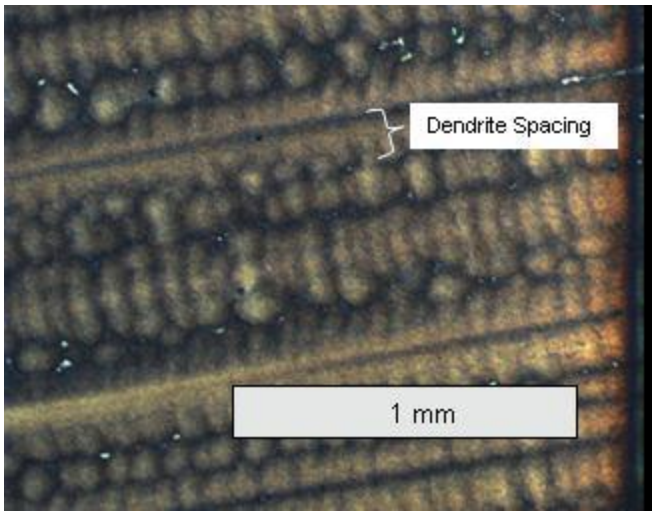

Figure 3.22: Dendrite Spacing of PWA 1484 [14]

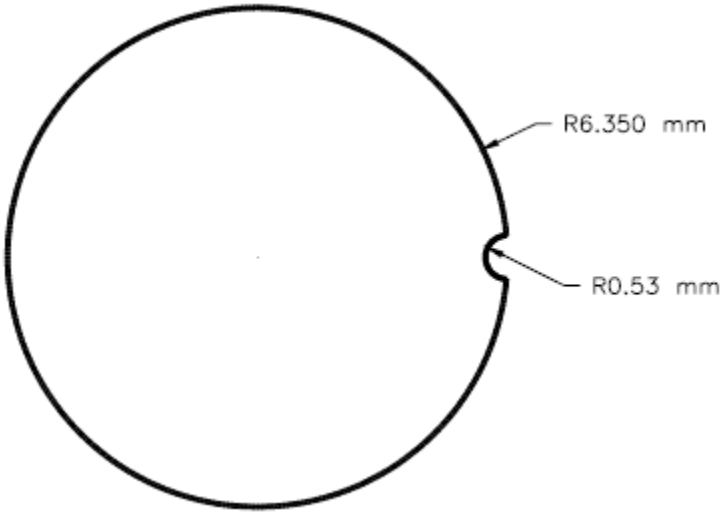

Figure 3.23: Schematic of Crack Initiation Criteria [14]

An alternative failure criterion used for comparison to Pratt & Whitney data corresponds to a 50% drop in load from the peak load seen during the test. In addition, although it was desired that the tests be stopped prior to the final specimen fracture in order to prevent damage to the extensometer rods or other equipment, specimen separation did occur to end several of the tests. As a result, for each TMF test conducted

in this study, the cycles at which a 1% load drop (N_i), 50% load drop, and specimen separation or test stoppage (N_f) were all recorded.

3.9: TMF Test Plan

Table 3.5 contains the test matrix used for this research project. All of the tests were performed under mechanical strain control and used the fully-reversed out-of-phase (OP) TMF waveform. A ramp waveform with a three-minute cycle and a temperature range of 550-1050°C was used in order to mimic cycle conditions in the work done by Amaro [14] on solid specimens. This would isolate any effects on the TMF life caused by specimen geometry. Each test was also performed on an uncoated and coated specimen in order to investigate the effects of the coating on life and damage mechanisms.

Table 3.5: TMF Test Matrix

Waveform	***R*-ratio**	**$\Delta\varepsilon_{mech}$ (%)**	**Cycle Time (sec)**	**T_{min} (°C)**	**T_{max} (°C)**
OP TMF, ramp	-1	0.5	180	550	1050
OP TMF, ramp	-1	0.7	180	550	1050
OP TMF, ramp	-1	0.8	180	550	1050
OP TMF, ramp	-1	0.9	180	550	1050

CHAPTER 4

RESULTS AND DISCUSSION

4.1: Introduction

This chapter presents all the results for this work. First, the analysis of the modified gripping method is explained, including results from both hand calculations and finite element analysis. Next, the actual TMF test results are given; first, the lives according to different failure criteria are compared, followed by more detailed plots and description of the material behavior during each test. Finally, the main research objectives are fulfilled by the following: (1) comparing the TMF results from this work for uncoated and coated specimens; (2) comparing these test results to those from previous testing at Georgia Tech, which used a different specimen geometry under identical test conditions; and (3) comparing these results to those from testing in Pratt & Whitney labs with the same specimen geometry under different test conditions.

4.2: Gripping Method Analysis

4.2.1: Hand Calculations

4.2.1.1: General Introduction of Calculations

Prior to modifying the specimens to prevent crushing in the collet grips, hand calculations assuming elastic deformation were performed to calculate the amount of hoop stress that would be induced in the ends of the specimen during the shrink of the plug. The goal was to create light pressure for a solid contact between the specimen and

plug without resulting in any harmful stresses in the specimen. Before the actual inner diameter of each specimen was known, the entire range of allowable hole sizes within the specified machining tolerance was explored. First, it was desired that only a single plug size would be used, and the hoop stress in the gripping section of the specimen was calculated in a simplified manner assuming that the plug was undeformable. Then, the stresses were recalculated accounting for the deformation of the plug, assuming it was also made from PWA 1484 as originally planned. A solution was explored to reduce the stresses by using multiple plug sizes, and finally the stresses resulting from the prescribed plug sizes for the actual specimen hole sizes were found.

4.2.1.2: General Equations

The cylindrical hollow specimen was treated as a thick-walled pressure vessel. Equations 4.1 through 4.3 were derived from Lame's equations [104]. The hoop stress in the specimen at a certain radius r is given by Equation 4.1,

$$\sigma_c(r) = \frac{p_i r_i^2 - p_o r_o^2}{r_o^2 - r_i^2} - \frac{r_i^2 r_o^2 (p_o - p_i)}{r^2 (r_o^2 - r_i^2)} \tag{4.1}$$

where p_i is the internal pressure, p_o is the external pressure, r_i is the inner radius, and r_o is the outer radius. Neglecting the external pressure and replacing the internal pressure with the pressure p applied from the plug after the shrink fit, the hoop stress is given by Equation 4.2. The hoop stress is maximum at the inner radius of the specimen (where $r = r_i$).

$$\sigma_c(r) = p \frac{r_i^2}{r_o^2 - r_i^2} \left(1 + \frac{r_o^2}{r^2}\right) \tag{4.2}$$

The pressure introduced by a shrink fit between the specimen and the plug is given by Equation 4.3,

$$p = \frac{\delta_r}{\frac{R_t}{E_s}\left(\frac{r_o^2 + R_t^2}{r_o^2 - R_t^2} + \nu_s\right) + \frac{R_t}{E_p}\left(1 - \nu_p\right)} \tag{4.3}$$

where δ_r is the radial interference, R_t is the nominal transition radius (after both bodies have deformed), E_s and E_p are the elastic modulus of the specimen and plug, respectively, and ν_s and ν_p are the Poisson's ratio of the specimen and the plug, respectively. The radial interference δ_r is simply the difference between the plug radius (r_p) and r_i since the plug radius is initially larger than the inner radius of the specimen. For the following calculations, the pressure from the shrink fit given in Equation 4.3 was substituted into the expression for the hoop stress in Equation 4.2.

4.2.1.3: Simplified Calculation Assuming Undeformable Plug

For the first set of calculations, the plug was assumed to be undeformable, which would greatly simplify the calculations and provide a hoop stress higher than would be expected in reality. If the plug cannot be deformed, its modulus essentially goes to infinity, and the nominal transition radius simply becomes the radius of the plug ($R_t = r_p$). Therefore, the contact pressure for this case can be described by Equation 4.4.

$$p = \frac{r_p - r_i}{\frac{r_p}{E_s}\left(\frac{r_o^2 + r_p^2}{r_o^2 - r_p^2} + \nu_s\right)} \tag{4.4}$$

After Equation 4.4 is substituted into the expression for hoop stress in Equation 4.2, the goal was to obtain the plug radius as a function of the desired hoop stress.

However, this could not be done algebraically, but the plug radius at a certain value of hoop stress can be found using the Goal Seek function in Microsoft Excel. All of the calculations take the outer radius to be r_o = 7.874 mm. The calculations used the properties E_s = 127,553 MPa and ν_s = 0.37 for PWA 1484 [103, 105]. The value used for ν_s was based on that of the similar nickel base superalloy CMSX-4, but regardless of the value chosen, it was also discovered that the results were insensitive to Poisson's ratio.

Table 4.1 shows the results of these calculations. The plug diameter that would give the desired hoop stress on the inner radius of the specimen (ranging from 3.45 MPa to 34.5 MPa) for the largest hole (11.4804 mm diameter) is displayed, followed by the corresponding hoop stress for the same plug size in the smallest hole (11.3792 mm diameter). The results clearly suggest that a plug fit for the largest hole would produce extremely large stresses when inserted into the smallest hole, which would even cause plastic deformation as the yield stress of PWA 1484 is 895 MPa at room temperature [103]. Since the assumptions for this exercise resulted in higher stresses, it was decided that a more rigorous calculation should be undertaken in order to provide a better estimate of the actual hoop stresses in the case that they may actually be tolerable.

Table 4.1: Results of Hoop Stress Calculations Assuming Undeformable Plug

Hoop Stress for Largest Hole (MPa)	**Resulting Plug Diameter (mm)**	**Resulting Hoop Stress for Smallest Hole (MPa)**
3.45	11.48115	991.3
6.90	11.48149	994.6
10.35	11.48184	997.8
13.80	11.48218	1001.1
17.25	11.48253	1004.3
20.70	11.48288	1007.6
24.15	11.48322	1010.8
27.60	11.48357	1014.1
31.05	11.48391	1017.3
34.50	11.48426	1020.6

Figure 4.1 shows a graphical representation of the hoop stress as a function of plug diameter for three different possible specimen inner diameters (IDs). The representative hole sizes that were chosen are the target ID (11.43 mm), the smallest possible ID (11.3792 mm), and the largest possible ID (11.4808 mm). It can be seen that based on these assumptions, even for a plug diameter that barely contacts the largest hole, the hoop stresses would already be much too high for the smaller holes, and it may even exceed the elastic limit of the material. Therefore, more rigorous and accurate calculations were undertaken.

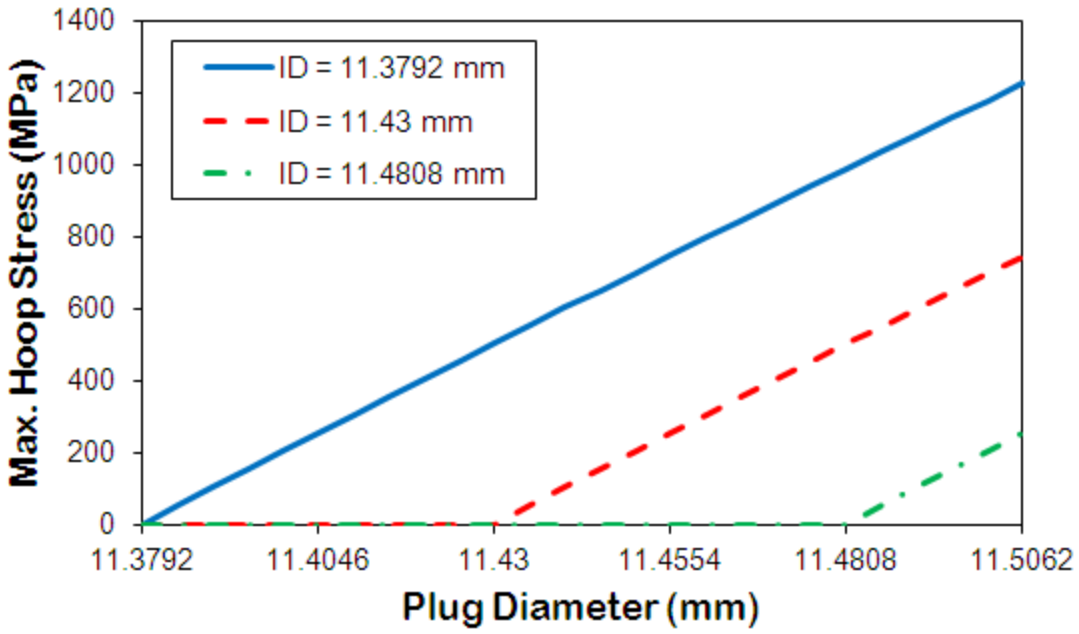

Figure 4.1: Hoop Stress as a Function of Plug Diameter for Different Hole Sizes

4.2.1.4: Calculation Accounting for Deformable Plug

Since the "worst-case scenario" explored above produced a result much worse than expected, a more realistic calculation accounting for the plug's deformation was performed. Equations 4.5 through 4.7 were derived using Hooke's law for two-dimensional plane stress [106]. The plug was taken as the same material as the specimen (PWA 1484) such that $E_s = E_p = E$ and $\nu_s = \nu_p = \nu$. In this case, the contact pressure can be described by Equation 4.5.

$$p = \frac{E\delta_r}{2R_t}\left(1 - \frac{R_t^2}{r_o^2}\right) \tag{4.5}$$

The maximum hoop stress (at the inner radius of the specimen) is given by Equation 4.6.

$$\sigma_{c,max} = p\frac{r_o^2 + R_t^2}{r_o^2 - R_t^2} \tag{4.6}$$

Since the nominal transition radius R_t was not initially known, an iterative approach was used. An expression for the decrease in the radius of the plug is given in Equation 4.7.

$$\delta_p = r_p - R_t = \frac{pR_t}{E}(1-\nu) \tag{4.7}$$

An initial guess for R_t was taken to be the average of the plug radius and the inner specimen radius. After the pressure and hoop stress were evaluated based on this value for R_t, a value of δ_p was calculated, which then led to a value of R_t closer to the actual number. Ten of these iterations were used (which was more than adequate to achieve convergence), and the Goal Seek function in Microsoft Excel was used to find the plug size needed to obtain the desired value of the hoop stress at the final iteration.

Table 4.2 displays the results obtained` using this method. As the calculations were more in-depth, only three representative values of hoop stress were chosen, including a much smaller value (0.345 MPa) than had previously been explored. As before, even with the plug deforming and introducing a smaller stress, the resulting hoop stresses from a plug fit for the largest hole in specimens with the smallest hole is still much too large (and approaching/exceeding yield). In this case, the stresses in small-holed specimens did marginally decrease, but not to the extent of considering this approach to be a viable option. As a result, it was concluded that one plug size could not fit all of the possible hole sizes.

Table 4.2: Results of Hoop Stress Calculations Accounting for Plug Deformation

Hoop Stress for Largest Hole (MPa)	Resulting Plug Diameter (mm)	Resulting Hoop Stress for Smallest Hole (MPa)
0.345	11.48084	865.1
6.900	11.48161	871.6
34.500	11.48486	899.1

4.2.1.5: Calculations with Multiple Plug Sizes

One relatively easy solution was to machine four different plug sizes that would cover the whole range of the hole size tolerance in order to avoid having to machine a different sized plug for each of the specimens. The plug diameters would be 11.4046 mm, 11.43 mm, 11.4554 mm, and 11.4808 mm. The only possible problem would be for a hole diameter exactly at the upper end of its tolerance range (11.4808 mm), which could result in a plug diameter equal to or smaller than the hole diameter. If it were deemed necessary after measuring the holes, another plug with a diameter of 11.5062 mm could have been be machined for such specimens.

Table 4.3 explicitly shows the prescribed plug diameters for each range of hole size within the machining tolerance. The hoop stress accounting for a deformable plug in the smallest hole size within the range was also calculated (for example, the hoop stress applied by the 11.4046 mm plug in the 11.3792 mm hole). Based on the results, the hoop stress in the specimen would stay below 217 MPa if a properly sized plug were inserted.

Table 4.3: Plug Size Prescriptions and Largest Resulting Hoop Stresses

Hole Diameter Range (mm)	Plug Diameter (mm)	Actual Hoop Stress for Smallest Hole (MPa)
$11.3792 \leq 2r_i < 11.4046$	11.4046	216.6
$11.4046 \leq 2r_i < 11.4300$	11.4300	216.4
$11.4300 \leq 2r_i < 11.4554$	11.4554	216.3
$11.4554 \leq 2r_i < 11.4808$	11.4808	216.1

Figure 4.2 shows the hoop stress that would be applied to the inner radius of the specimen for the four different plug diameters, assuming an undeformable plug. Therefore, the stresses shown here are a slight overestimate, and the actual maximum stresses for each plug size are shown above in Table 4.3. With this plug sizing plan, the hoop stresses for all hole sizes within the tolerance would be in an acceptable range.

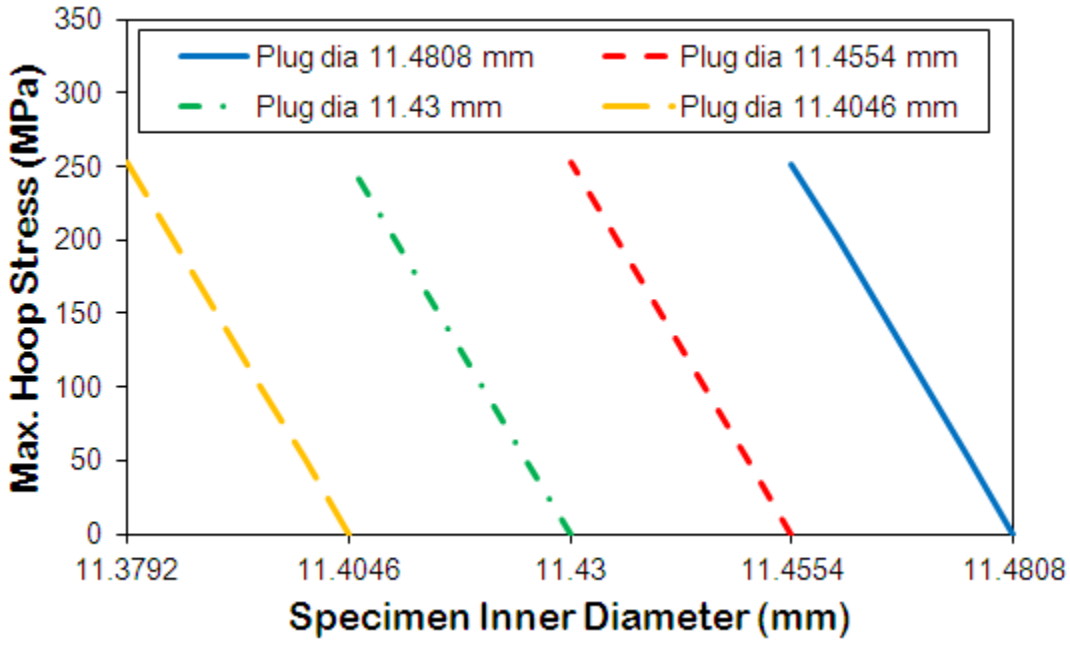

Figure 4.2: Hoop Stress as a Function of Hole Diameter for Four Plug Sizes

4.2.1.6: Revised Calculations After Specimen Measurements

After the specimens were received, the actual inner diameters were measured. It was found that there were only three different hole sizes: 11.4173 mm (12 specimens), 11.4046 mm (2 specimens), and 11.3792 mm (1 specimen). Therefore, according to Table 4.3, only two different plug sizes were needed. Since only three sets of calculations were required, the deformation of the plug was included, and a similar process to that described in section 4.2.1.4 was used. In addition to the maximum hoop stress, the maximum von Mises stress in the specimen was also calculated. The von Mises stress σ_{VM} is defined by Equation 4.8 [107],

$$\sigma_{VM} = \frac{1}{\sqrt{2}}\sqrt{(\sigma_1 - \sigma_2)^2 + (\sigma_2 - \sigma_3)^2 + (\sigma_3 - \sigma_1)^2} \tag{4.8}$$

where σ_1, σ_2, σ_3 are the principal stresses. In this case, since the longitudinal stress is zero, the only two principal stresses are the radial stress (which is equal to the pressure from the interference fit, p) and the hoop stress, σ_c.

Table 4.4 shows the results of the finalized hand calculations for the maximum stresses at the inner surface of the specimen. As planned, all of the resulting stresses are manageable. Fortunately, the majority of the specimens also experience the smallest stresses, and the von Mises stress for all of the specimens is well below the yield stress.

Table 4.4: Revised Calculations for Maximum Specimen Stresses from Shrink Fit

Number of Specimens	Hole Diameter (mm)	Plug Diameter (mm)	Hoop Stress (MPa)	Von Mises Stress (MPa)
12	11.4173	11.4300	108.2	125.0
2	11.4046	11.4300	216.4	250.0
1	11.3792	11.4046	216.6	250.1

4.2.2: Finite Element Analysis

4.2.2.1: General Introduction of Models

In addition to the hand calculations, finite element analysis (FEA) models of the specimen were created in order to check for any large stress concentrations or unwanted stresses in the specimen's gage section resulting from the modified gripping mechanism. For easier visualization of the following models, Figure 4.3 shows a free body cut view of the specimen along its longitudinal axis. Plugs can be seen at each end of the specimen. The axis of symmetry is shown as the dotted yellow line, and the plane of symmetry across the center of the specimen is shown as the dotted red line. Both axisymmetric and three-dimensional models were used for the analysis. The axisymmetric model would be represented by one side of components in the cross-section visible in this figure.

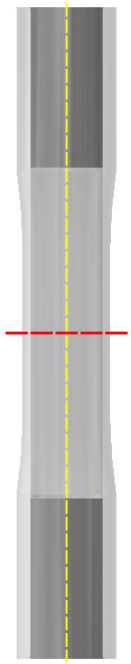

Figure 4.3: View of Free Body Cut of Specimen and Plugs

Figure 4.4 shows the axisymmetric models of the specimen, plug, and adapters that were created in Abaqus. Models with and without a plug present in the end of the specimen were compared. The model of the plugged specimen included two steps: (1) the shrink fit itself, and then (2) the actual application of the gripping force. A symmetric boundary condition was applied at the midpoint of the specimen, and the clamping load was distributed over the outer surface of the collet adapters. For simplicity, only the region of the collet adapters above the end of the specimen and plug was included in the models. The mesh used eight-node axisymmetric quadrilateral elements and was refined until convergence in the stress was achieved, resulting in an element size of 0.127 mm.

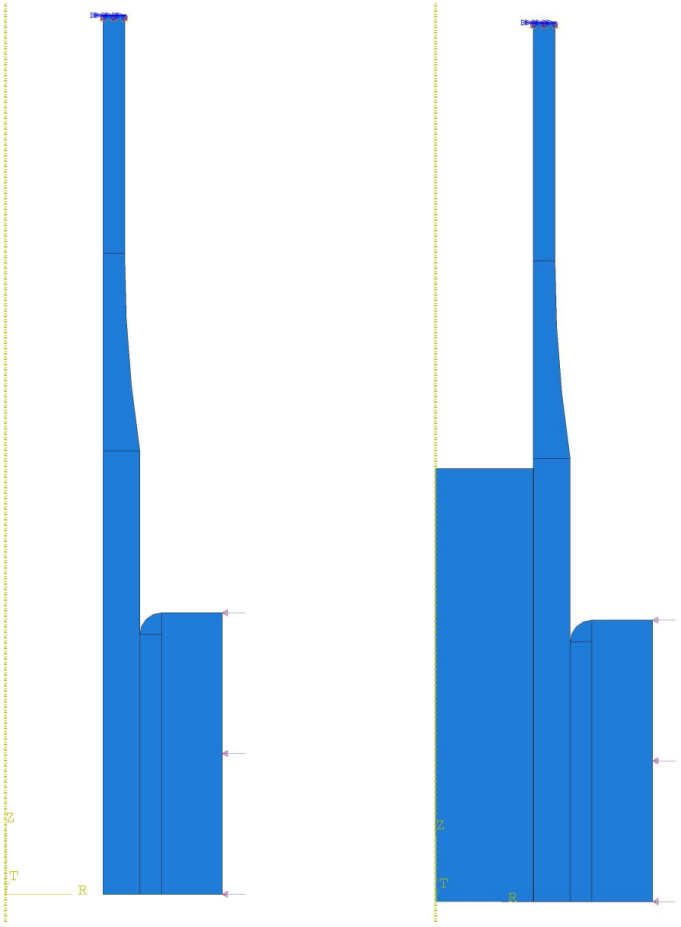

Figure 4.4: Axisymmetric FEA Models without and with a Plug

A full three-dimensional model was also initially created, as shown in Figure 4.5. The left view shows the outer surface of the specimen within the collet adapters, and the right view shows the assembly as translucent so that the whole specimen and the plug are visible. As before (although not shown in the figure), both a plugged and unplugged specimen were modeled. As with the axisymmetric model, only half of the specimen was modeled using symmetry, and the clamping force was applied to the outer surface of the collet adapters, which were modeled in full for this case.

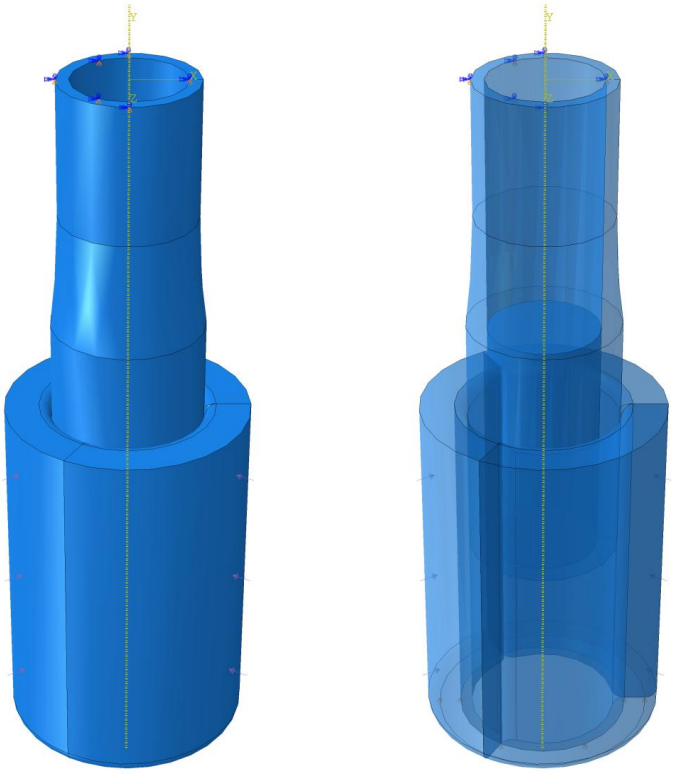

Figure 4.5: Opaque and Translucent View of Three-Dimensional FEA model

Since the results of the three-dimensional model were found to be consistent with the axisymmetric model after mesh refinement, the three-dimensional was abandoned to greatly save time and computational power. Therefore, all of the following FEA results

refer to the axisymmetric models shown in Figure 4.4. As previously mentioned, the elastic modulus and Poisson's ratio for the specimen were input as 127.553 GPa and 0.37, respectively. The plug and collet adapters were assigned a modulus of 200 GPa and a Poisson's ratio of 0.3, typical properties of steels [24]. The specimen inner radius was defined as 5.715 mm, and for the model including a plug, the plug radius was 5.7277 mm so that the maximum possible interference during the shrink fit (0.0254 mm) was modeled. As calculated in section 3.4.3, a clamping pressure of 531.0 MPa was applied. All of the results show the von Mises stress in MPa. For comparison to the stresses, as noted earlier, the yield stress for PWA 1484 at room temperature is 895 MPa.

4.2.2.2: Gripping an Unplugged Specimen

Figure 4.6 shows the FEA results for the gripping of an unplugged specimen including the whole model, while Figure 4.7 shows an augmented view of the stresses in the specimen gripping section. The model predicts a stress concentration at the top edge of the specimen-adapter interface up to 1332 MPa, but during actual testing, no yielding in the specimen or adapters was observed at this point. Ignoring the stress concentration at that point, the maximum von Mises stress on the inner surface of the specimen is predicted to reach 1125.47 MPa with a large portion of the gripping section over the yield stress of 895 MPa. Therefore, it was predicted that the hollow specimen would indeed collapse within the collets, so it was determined that it was necessary to plug the ends to support the gripping section.

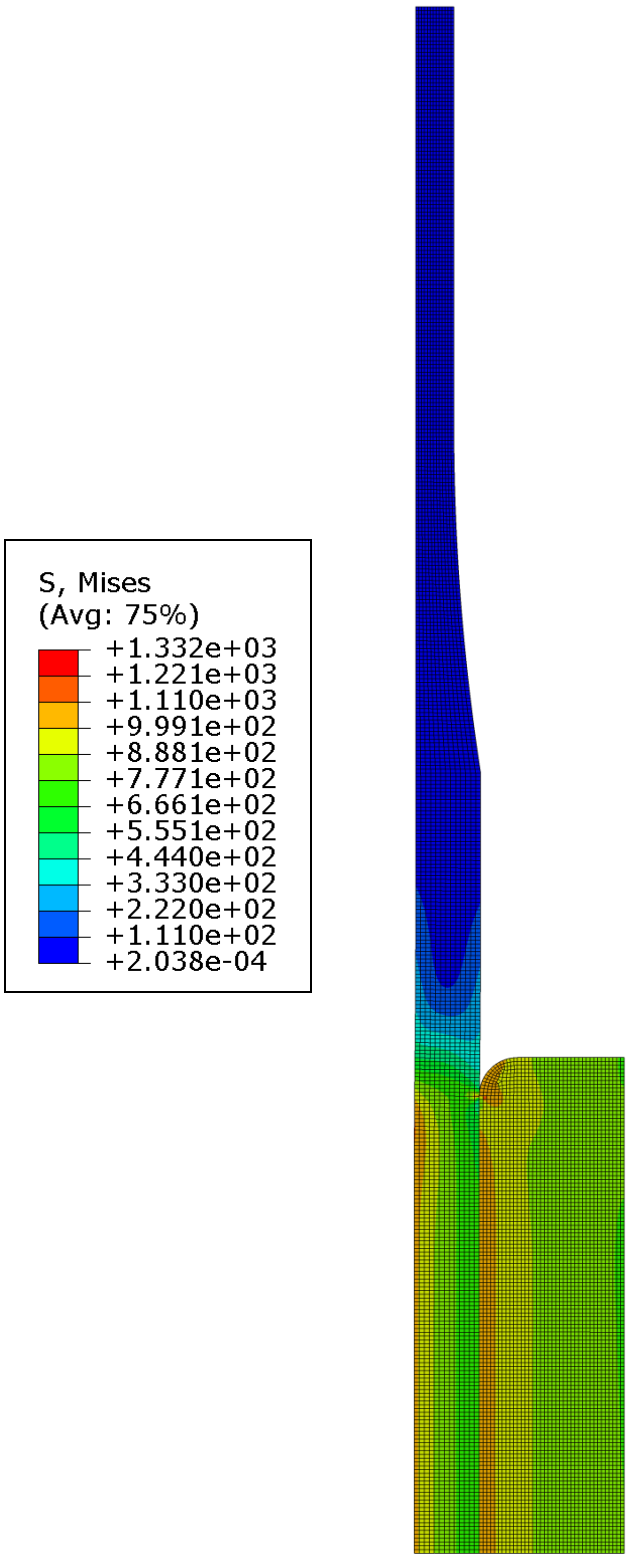

Figure 4.6: FEA Results for Gripping an Unplugged Specimen

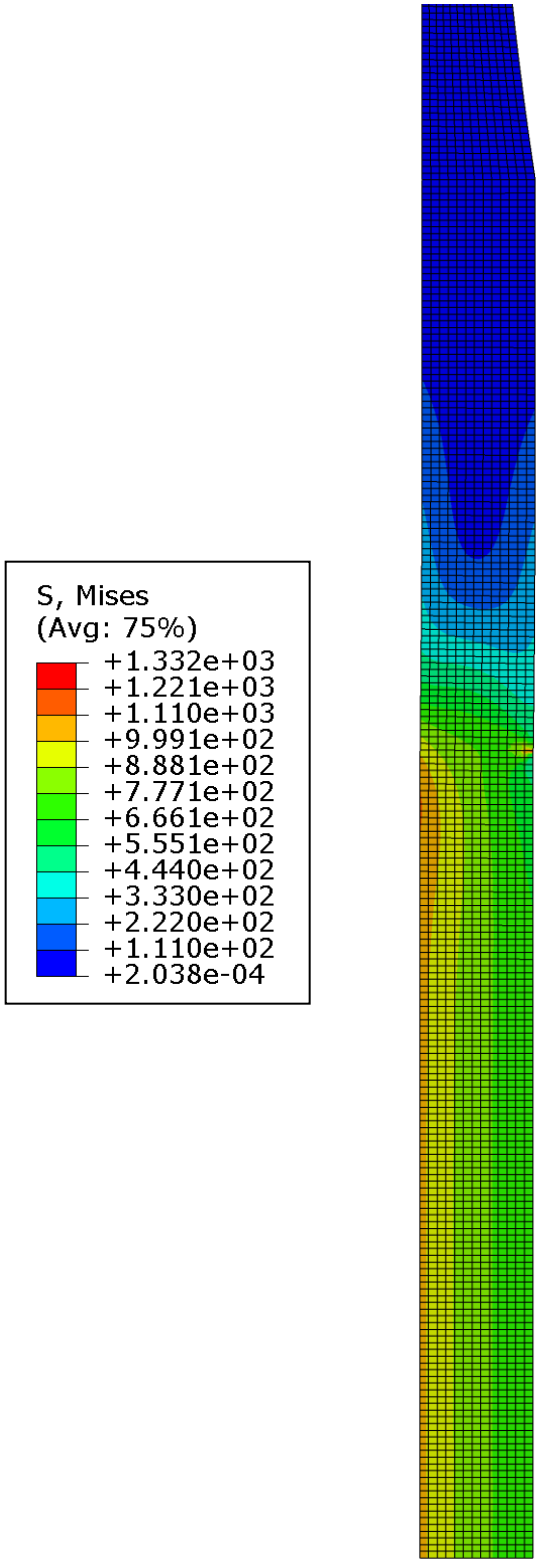

Figure 4.7: FEA Results for Gripping an Unplugged Specimen (Specimen Only)

4.2.2.3: Shrink Fit Step

Figure 4.8 shows the FEA results for the shrink fit step of the plugged model, while Figure 4.9 shows an augmented view of the specimen gripping section only. The highest stress of 458.8 MPa occurs at the top edge of the plug, but the highest stress in the specimen at that point only reaches 294.1 MPa. Away from this slight stress concentration, the stress at the inner surface of the specimen is only about 268 MPa. This result is only slightly higher than the von Mises stress of 250 MPa calculated by hand based on an identical radial interference (see Table 4.4 in section 4.2.1.6) and still well within a tolerable stress range. It can also be seen from the figures that only a negligible amount of stress is generated in the specimen's gage section from the insertion of the plug.

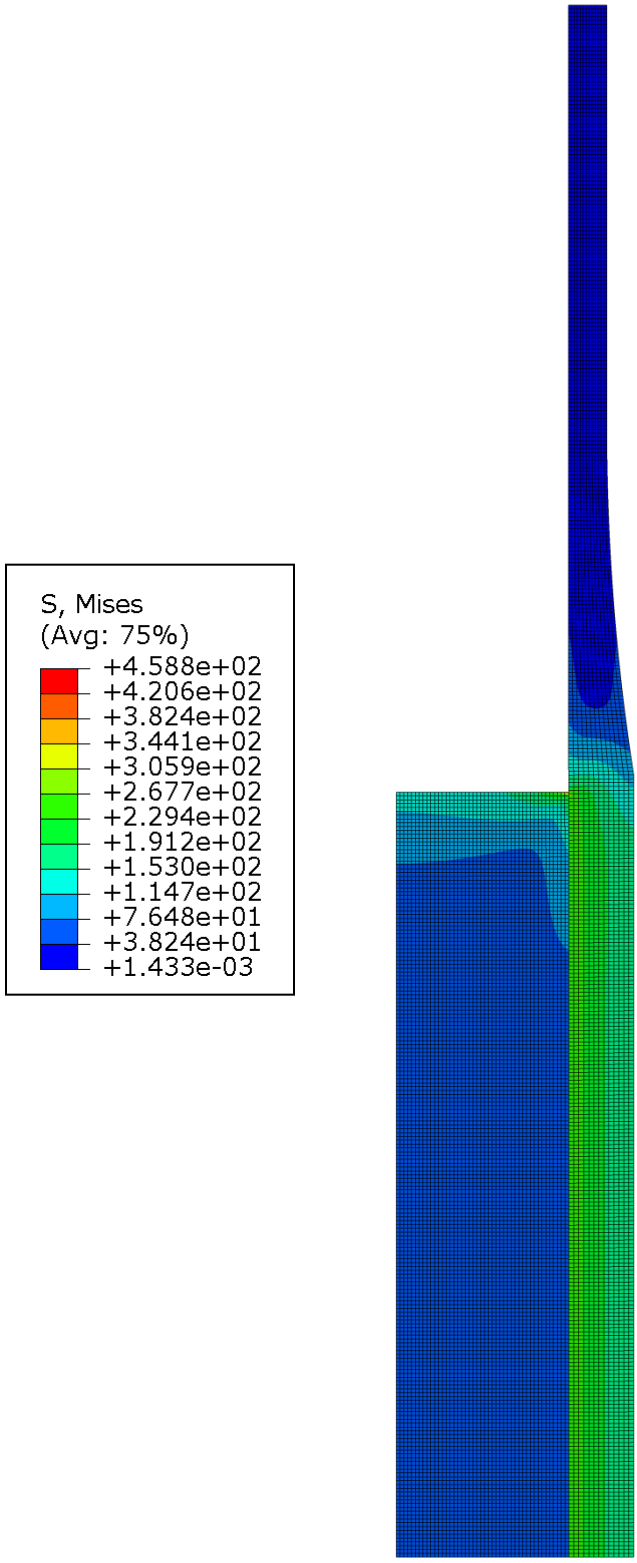

Figure 4.8: FEA Results for the Shrink Fit Step

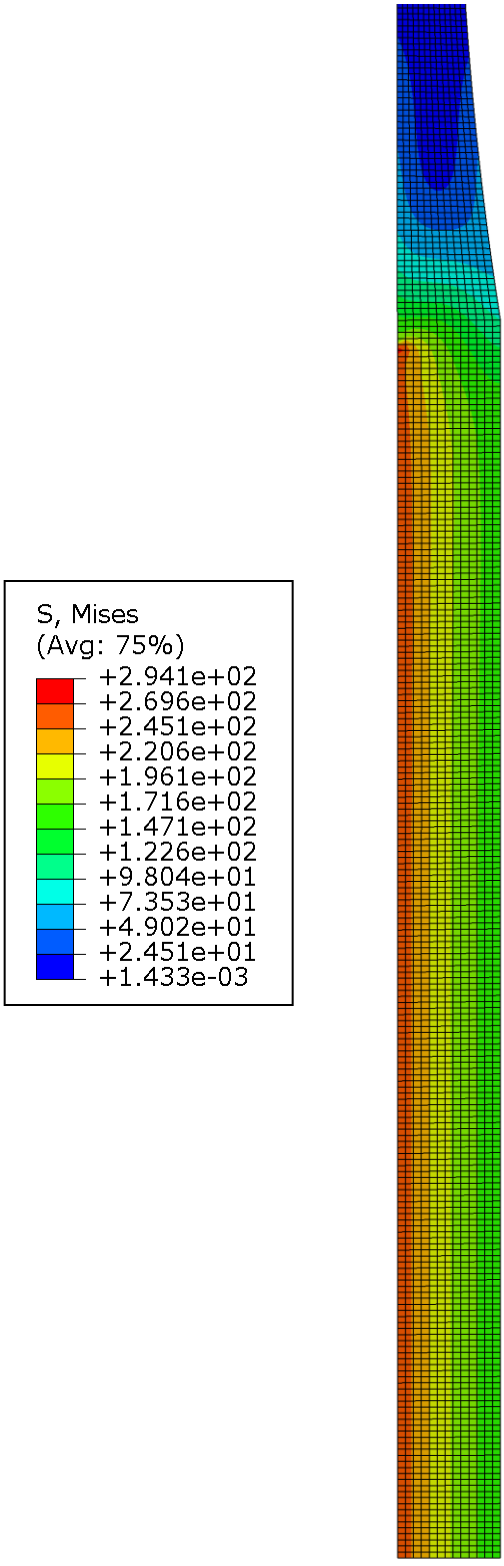

Figure 4.9: FEA Results for the Shrink Fit Step (Specimen Only)

4.2.2.4: Gripping a Plugged Specimen

Figure 4.10 shows the results for the stresses induced while gripping a plugged specimen, while Figure 4.11 shows an augmented view of the stresses in the specimen gripping section. As with the unplugged case, there is an artificially created stress concentration at the upper edge of where the adapter contacts the specimen. Away from this point, the actual maximum stress at the inner surface of the specimen ranges from between 577 MPa and 602 MPa. This is a drastic decrease in stress from the 1125 MPa predicted for the unplugged case, and the gripping should not result in yield. Also, even after gripping, no significant stresses are generated in the specimen's gage section. As a result, it was decided that plugging the specimen was not only necessary but also a stable and non-damaging way of gripping the specimen, and the modified gripping mechanism should have no impact on the TMF test results.

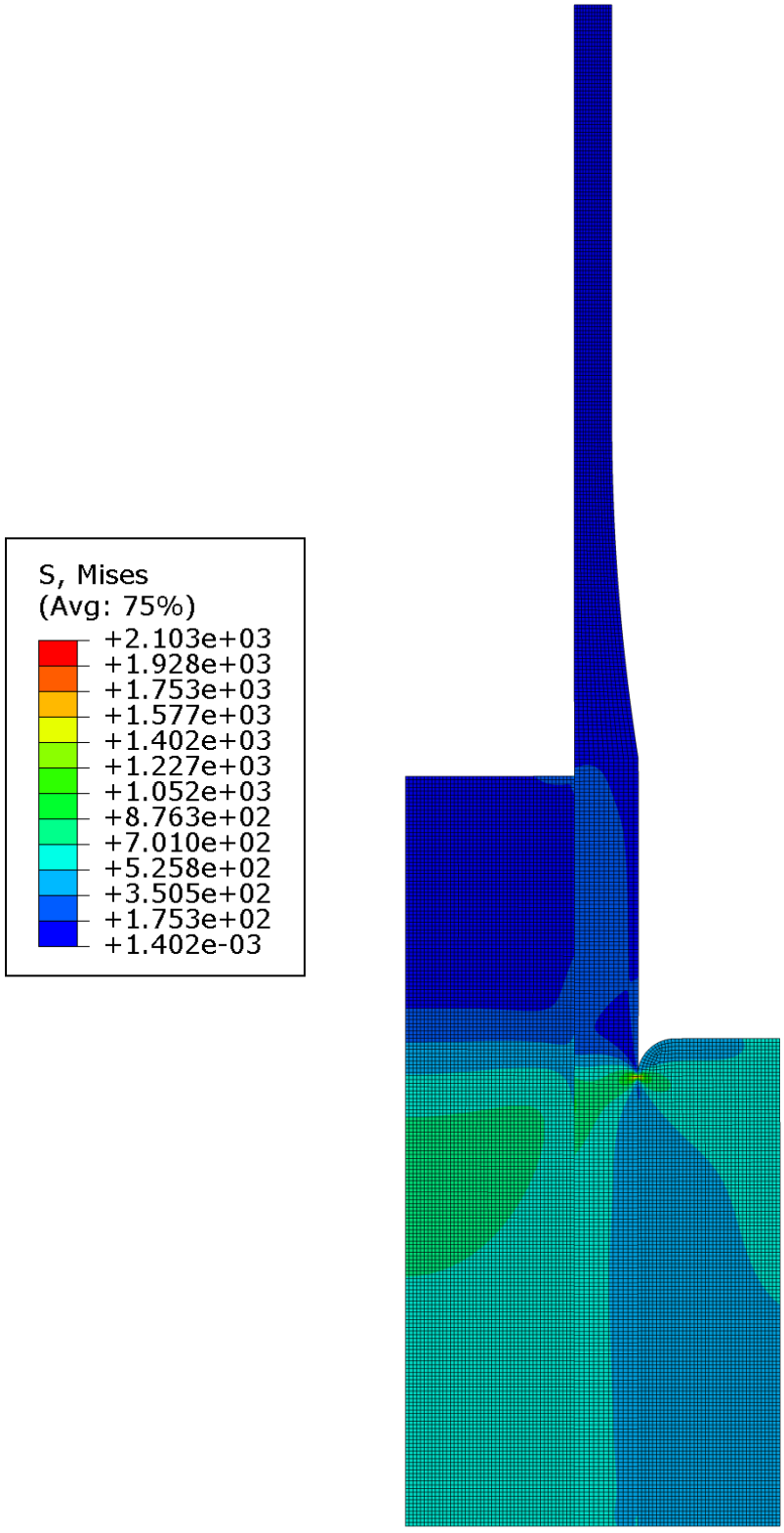

Figure 4.10: FEA Results for Gripping a Plugged Specimen

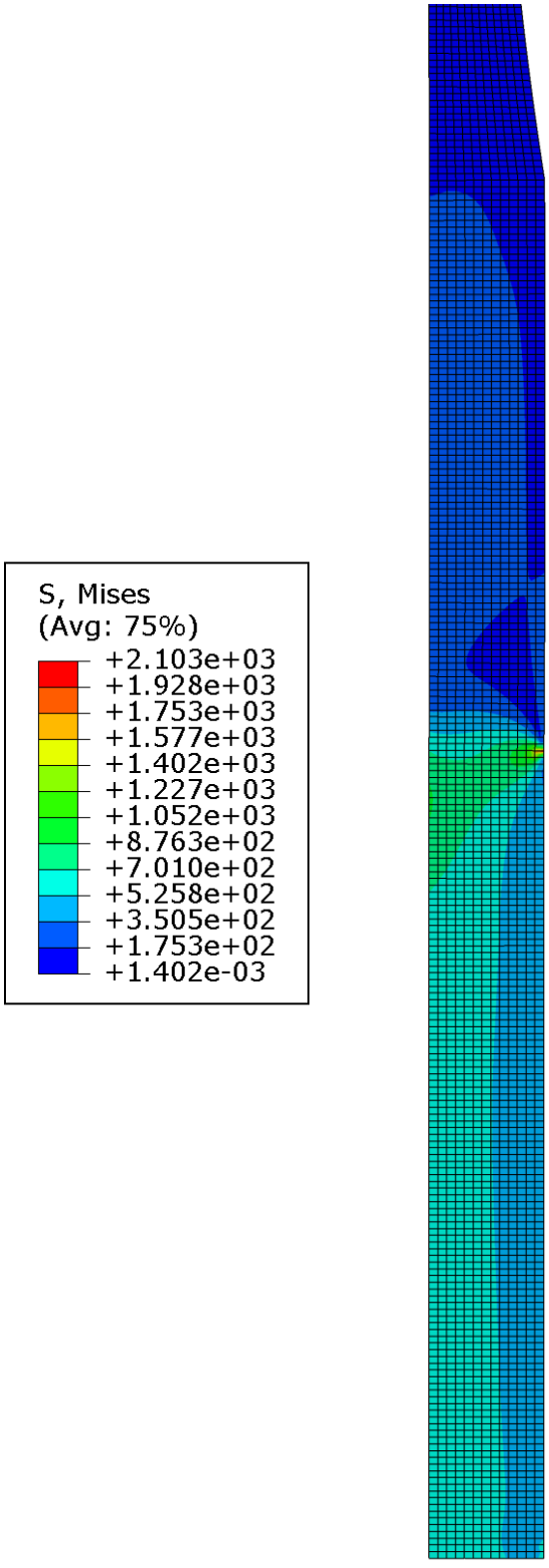

Figure 4.11: FEA Results for Gripping a Plugged Specimen (Specimen Only)

4.2.3: Air Pressure Calculations

If the plugs do indeed make the specimen air-tight, it was thought that the temperature changes of the trapped air could induce stresses in the gage section of the specimen. In order to ensure that the TMF tests essentially remained uniaxial, the pressures and resulting hoop stresses were calculated at the temperature endpoints of the baseline TMF cycle used. To find the pressure, the ideal gas law was used and simplified for a constant volume process, as shown in Equation 4.9 [108].

$$P_2 = P_1 \frac{T_2}{T_1} \tag{4.9}$$

In the above equation, P_1 and T_1 represent the pressure and temperature, respectively, at the beginning state, and P_2 and T_2 represent the pressure and temperature at the second state. For each case, T_1 = 293 K is room temperature, and P_1 = 101.325 kPa is atmospheric pressure.

Once these values were calculated, Equations 4.2 and 4.8 were used to find the resulting maximum hoop stress and von Mises stress, respectively, at the inner surface of the specimen. Inner and outer radii of r_i = 5.715 mm and r_o = 6.985 mm for the gage section of the specimen were used for the calculations. Table 4.5 shows that the resulting stresses in the specimen are essentially negligible, and the differences in pressure between the minimum and maximum temperatures should not be enough to make any significant impact on the test results.

Table 4.5: Results of Air Pressure Calculations

Temperature (°C)	Pressure (kPa)	Max. Hoop Stress (MPa)	Max. von Mises Stress (MPa)
550	284.6	1.44	1.68
1050	457.5	2.31	2.70

4.3: TMF Test Results

4.3.1: Life Results

The TMF life results can be found in Table 4.6 for uncoated specimens and Table 4.7 for coated specimens. All tests were performed with the OP TMF ramp waveform with temperatures ranging from 550-1050°C, a fully-reversed strain ratio of R = -1, and a cycle time of 180 seconds. The measured elastic modulus across the temperature range of the specimens used can be found in Appendix D. The cycles to crack initiation based on a 1% load drop (N_i), cycles to 50% load drop, and cycles to specimen failure or test stoppage (N_f) are reported for each test. Very little difference between the number of cycles to crack initiation and to a 50% load drop was observed, indicating rapid crack growth. On some occasions, the specimen fractured before a 50% load drop was reached. If the test was stopped manually before specimen separation, the lower bounding value for N_f is shown with an indication that the actual fracture cycle would have been greater.

The cycle N_i was determined through a double extrapolation technique. After plotting the stress extrema as a function of cycles, a line was fit to the stabilized linear region of the maximum tensile stress. The crack was said to have initiated after the maximum stress dropped 1% from the fitted line for two consecutive cycles. In this way, crack initiation was distinguished from any material softening behavior.

In all cases, the TMF life decreased with increasing strain range for a given type of specimen. Apart from the $\Delta\varepsilon_{mech}$ = 0.5% condition, the coated specimen exhibited slightly longer crack initiation life than the uncoated specimen at a given mechanical strain range.

Table 4.6: TMF Test Results for Uncoated Specimens

$\Delta\varepsilon_{mech}$ (%)	Specimen Number	N_i (cycles)	Cycles to 50% Load Drop	N_f (cycles)
0.5	5111AA-06-2	7393	7478	7520
0.7	5111AA-06-1	1153	1213	1219
0.8	5111AA-03-1	918	N/A	959
0.9	5111AA-02-1	361	N/A	365

Table 4.7: TMF Test Results for Coated Specimens

$\Delta\varepsilon_{mech}$ (%)	Specimen Number	N_i (cycles)	Cycles to 50% Load Drop	N_f (cycles)
0.5	5111AA-08-1	4464	4531	>4637
0.7	5111AA-08-2	1483	N/A	1517
0.8	5111AA-07-1	1407	1455	>1563
0.9	5111AA-09-2	513	N/A	518

4.3.2: Mechanical Strain Range 0.5%

The results for the $\Delta\varepsilon_{mech}$ = 0.5% tests are displayed below. The maximum, minimum, and mean stress and stress range as a function of cycle are shown in Figure 4.12 (uncoated) and Figure 4.14 (coated), and the stress-mechanical strain hysteresis loops for the first, half-life, and final cycle are shown in Figure 4.13 (uncoated) and Figure 4.15 (coated). In this case, contrary to each of the other results, the uncoated specimen had a considerably longer life. A kinematic hardening effect can be observed at

the beginning of each test, with the stress range staying fairly constant near 500 MPa while the mean stress increased until a stabilized value was reached at about 100 MPa. The stabilized tensile stress on the uncoated specimen was slightly higher, but both specimens exhibited similar first-cycle and stabilized hysteresis loops as well as mean stress and stress range during the progression of the test. Crack propagation occurred for quite a long period of time in each case, and the effect of the large cracks can be seen by the abrupt change of slope in the final cycle hysteresis loops once the load crosses into tension. The coated specimen exhibited an increase in both the maximum and minimum stresses preceding failure; it appears the crack initiated slightly outside of the extensometer rods before propagating in between them.

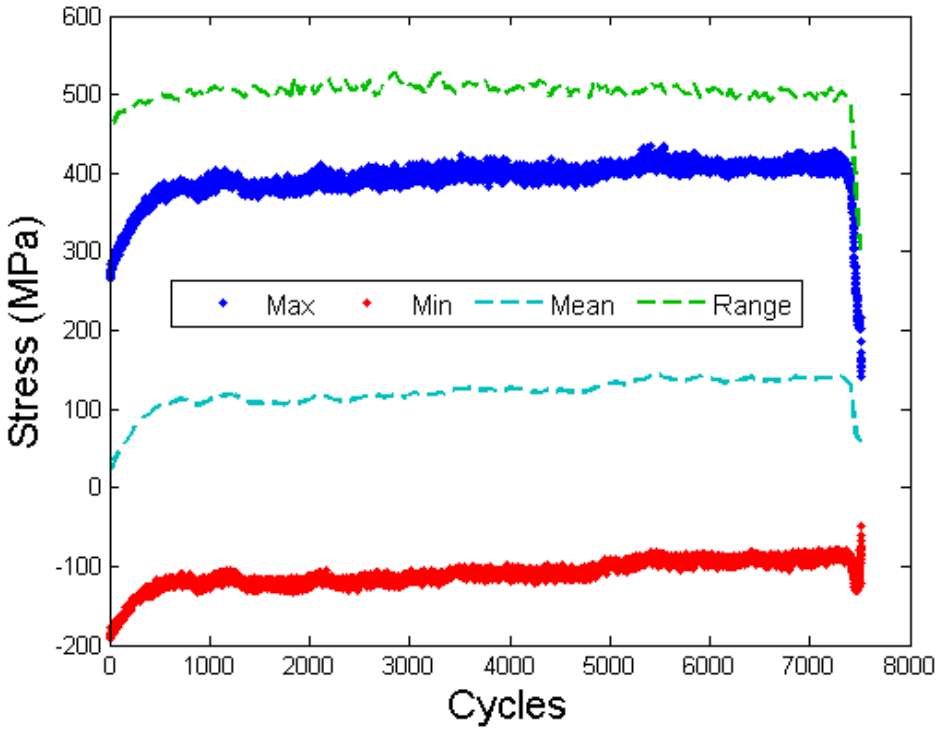

Figure 4.12: Stress History for Uncoated Specimen, $\Delta\varepsilon_{mech}$ = 0.5%

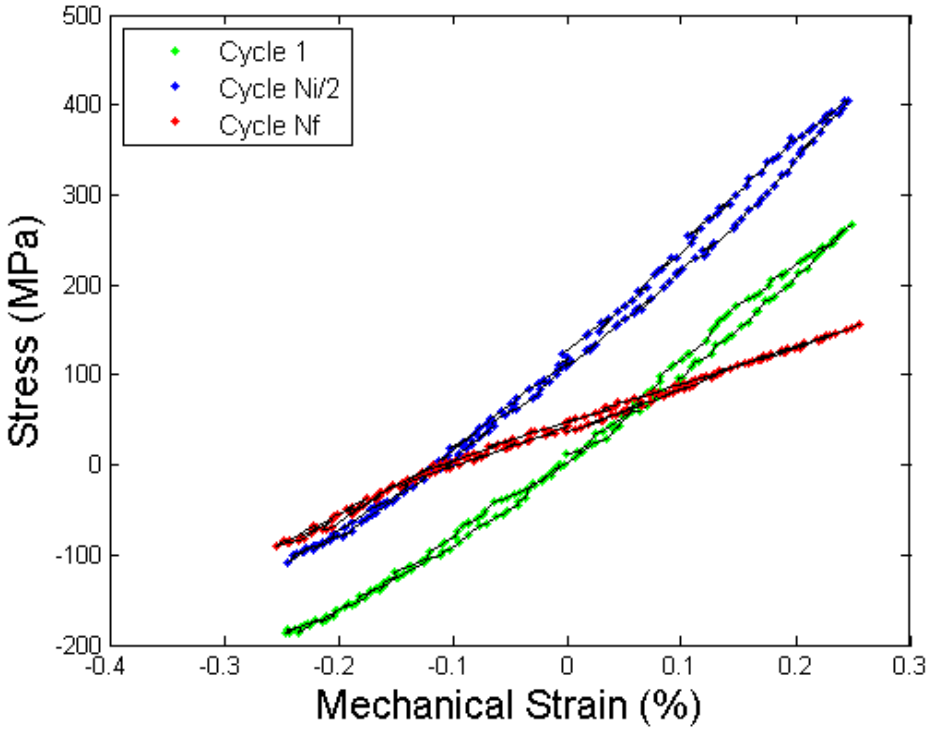

Figure 4.13: Hysteresis Loops for Uncoated Specimen, $\Delta\varepsilon_{mech}$ = 0.5%

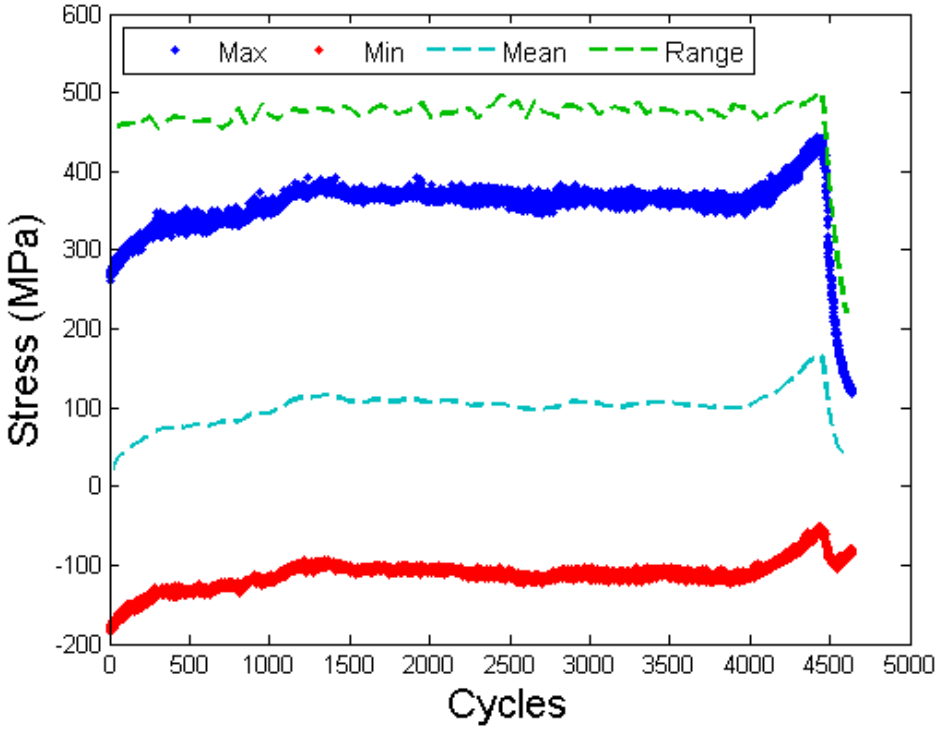

Figure 4.14: Stress History for Coated Specimen, $\Delta\varepsilon_{mech}$ = 0.5%

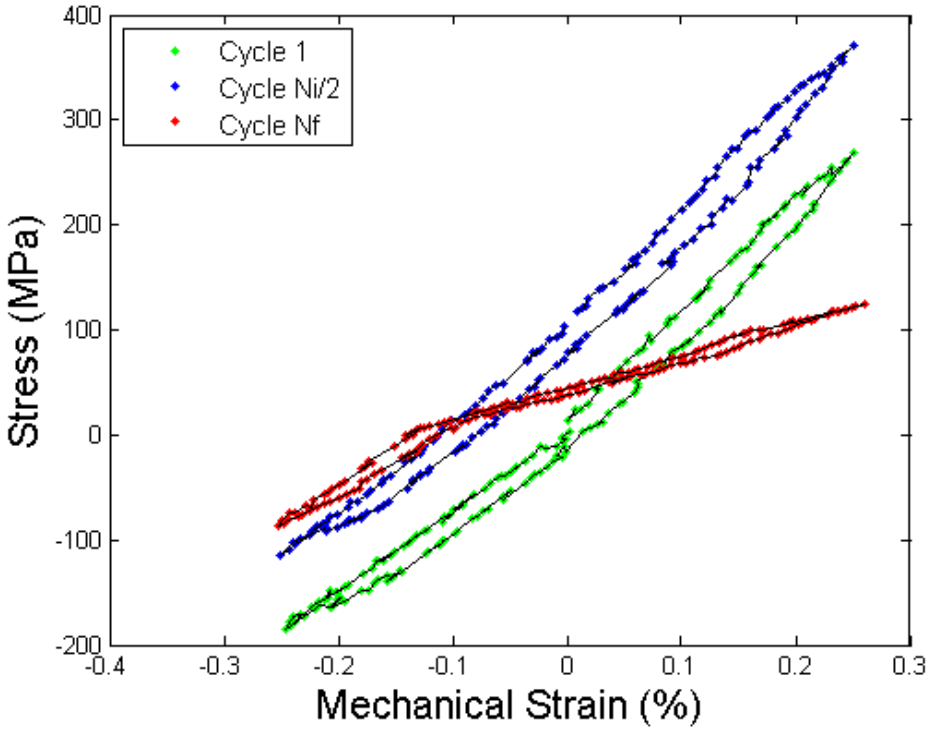

Figure 4.15: Hysteresis Loops for Coated Specimen, $\Delta\varepsilon_{mech}$ = 0.5%

4.3.3: Mechanical Strain Range 0.7%

The stress history and selected hysteresis loops for the uncoated specimen with $\Delta\varepsilon_{mech}$ = 0.7% are shown in Figure 4.16 and Figure 4.17, respectively. Again, a similar hardening behavior to both $\Delta\varepsilon_{mech}$ = 0.5% tests can be seen, and the mean stress stabilized slightly above 200 MPa with a stress range of just under 700 MPa. Crack initiation and propagation was observed from the tensile load drop before the specimen fractured.

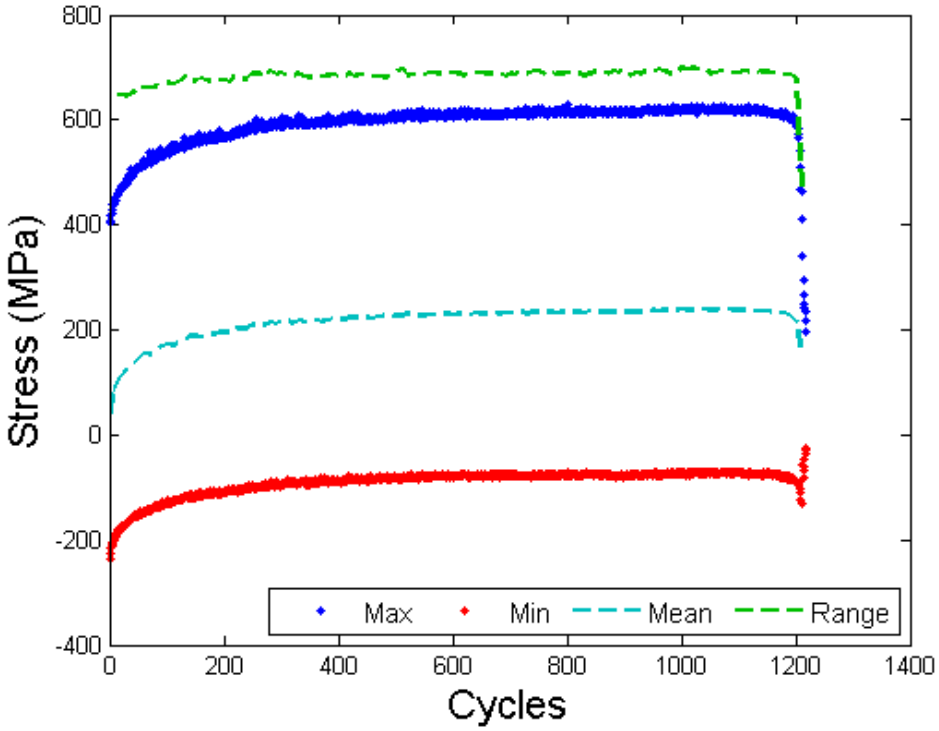

Figure 4.16: Stress History for Uncoated Specimen, $\Delta\varepsilon_{mech}$ = 0.7%

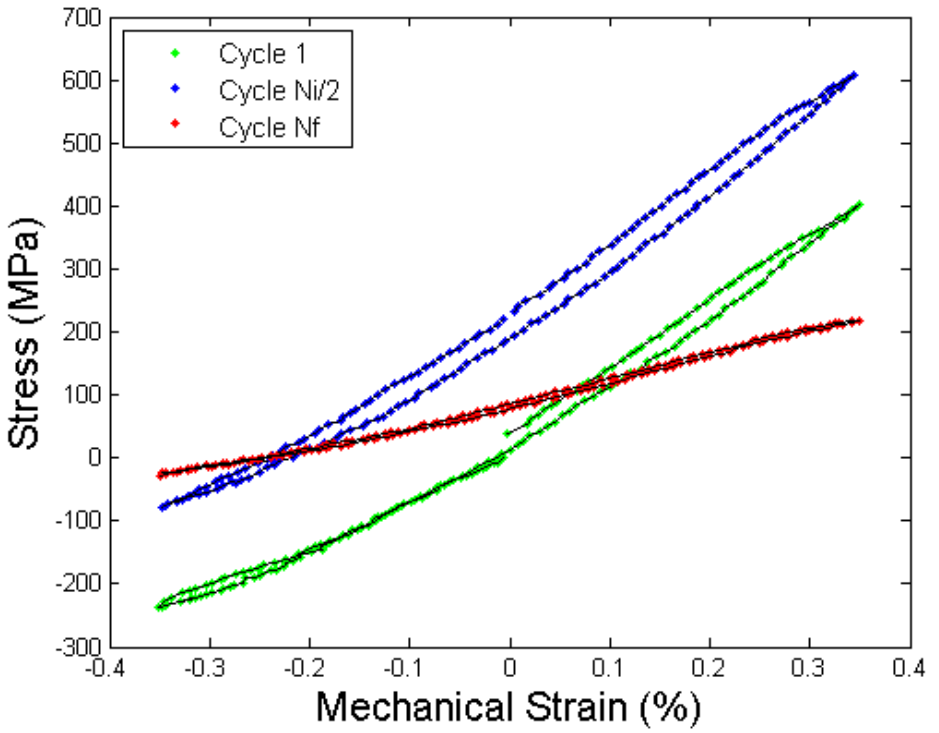

Figure 4.17: Hysteresis Loops for Uncoated Specimen, $\Delta\varepsilon_{mech}$ = 0.7%

The fracture surface of the uncoated specimen was observed using a scanning electron microscope (SEM). Figure 4.18 shows a thumbnail region on the outer surface that is believed to be a possible crack initiation point. A region of the surface exhibiting γ' avoidance is shown in Figure 4.19, indicating that this region of crack extension occurred at intermediate temperatures. An area of the fracture surface that experienced oxidation attack and surface voids can be seen in Figure 4.20, which was most likely exposed to the environment earlier in the crack extension process.

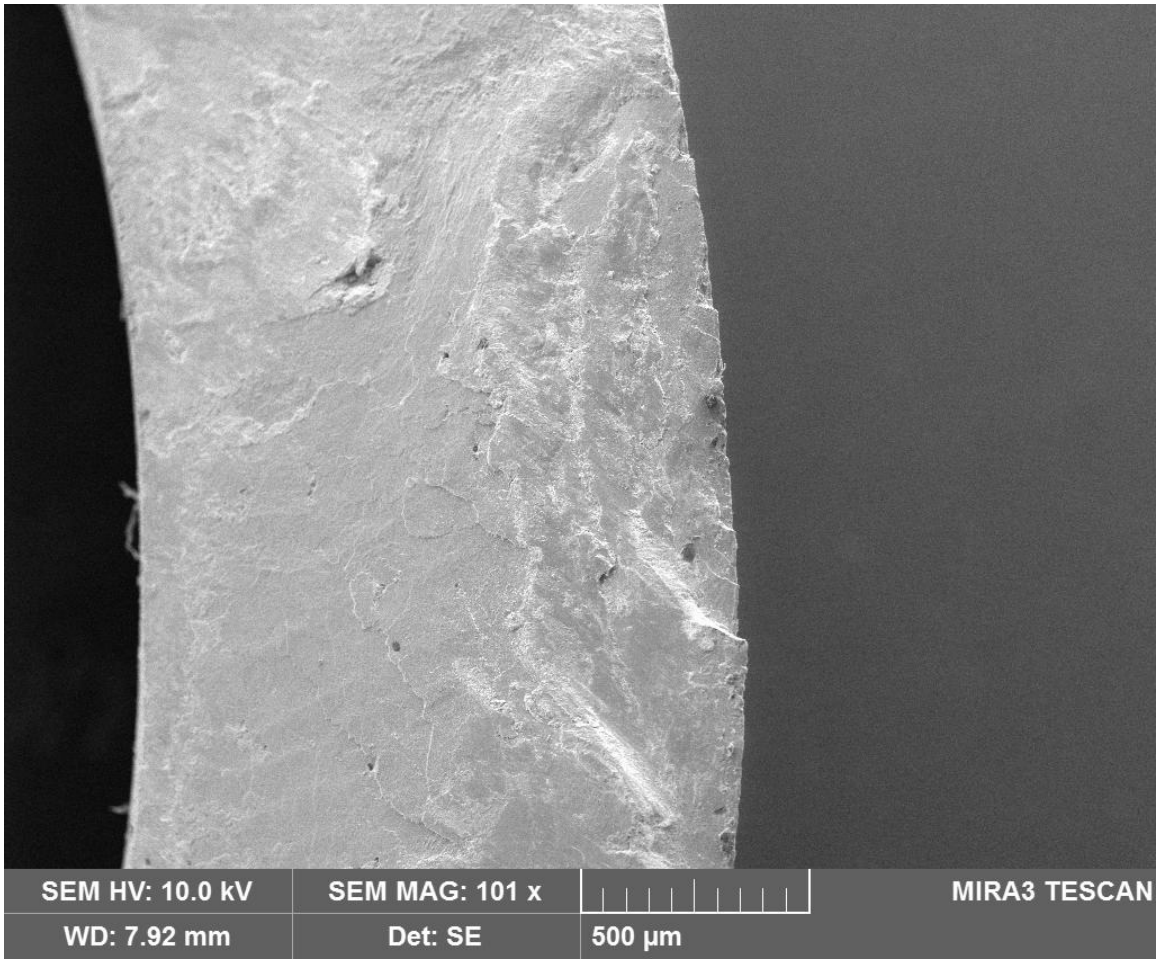

Figure 4.18: SEM Image Showing Possible Crack Initiation Point on the Fracture Surface of Specimen 5111AA-06-1 (Uncoated with $\Delta\varepsilon_{mech}$ = 0.7%)

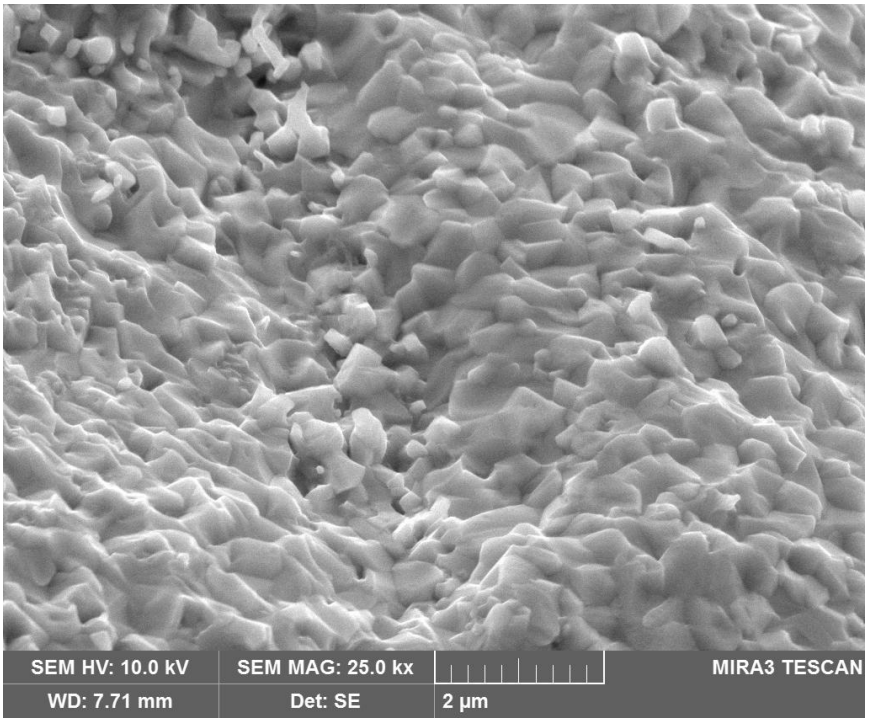

Figure 4.19: SEM Image Showing Gamma Prime Particle Avoidance on the Fracture Surface of Specimen 5111AA-06-1 (Uncoated with $\Delta\varepsilon_{mech}$ = 0.7%)

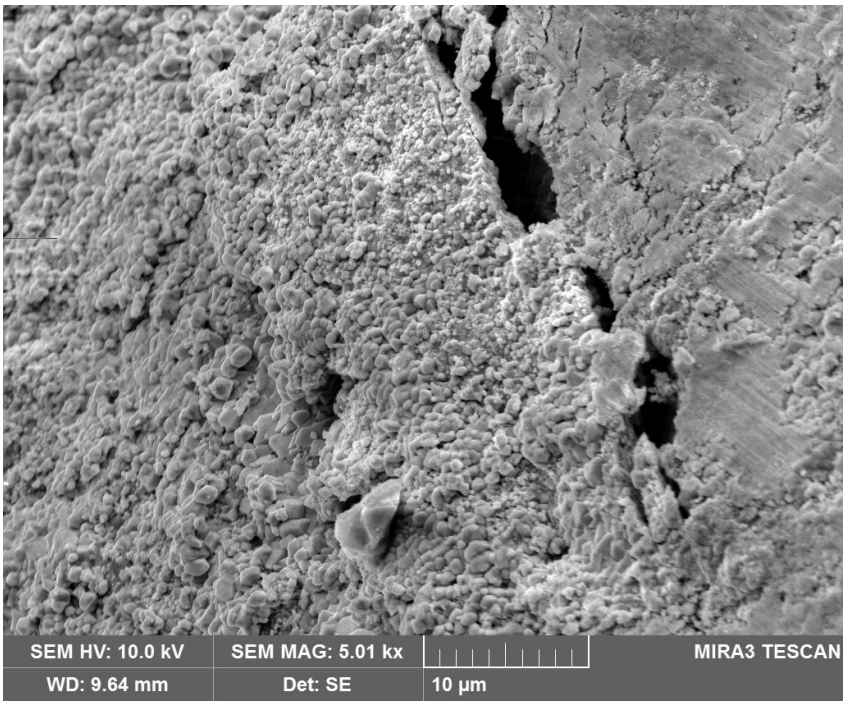

Figure 4.20: SEM Image Showing Regions of Oxidation and Voids on the Fracture Surface of Specimen 5111AA-06-1 (Uncoated with $\Delta\varepsilon_{mech}$ = 0.7%)

The stress history and hysteresis loops for the $\Delta\varepsilon_{mech}$ = 0.7% test on a coated specimen are shown in Figure 4.21 and Figure 4.22, respectively. The stress range was about the same as that of the uncoated specimen, although it did not exhibit as much hardening, so the mean stress throughout the test was lower and stayed around 100 MPa for most of the test. For this mechanical strain range, the coated specimen had a crack initiation life 330 cycles longer than the uncoated specimen, which may be explained by the lower mean stress. As expected for the higher strain range, the hysteresis loops are larger in total height and width than for the $\Delta\varepsilon_{mech}$ = 0.5% case seen in Figure 4.15. The tensile load did not drop as much prior to specimen fracture, so the final cycle loop did not exhibit the same bend as seen before for extensive cracking. Comparing the first cycle and half-life hysteresis loops to those observed in Figure 4.17, it is clear that the different hardening behavior of the coated specimen caused the mean stress to remain lower than that of the uncoated specimen.

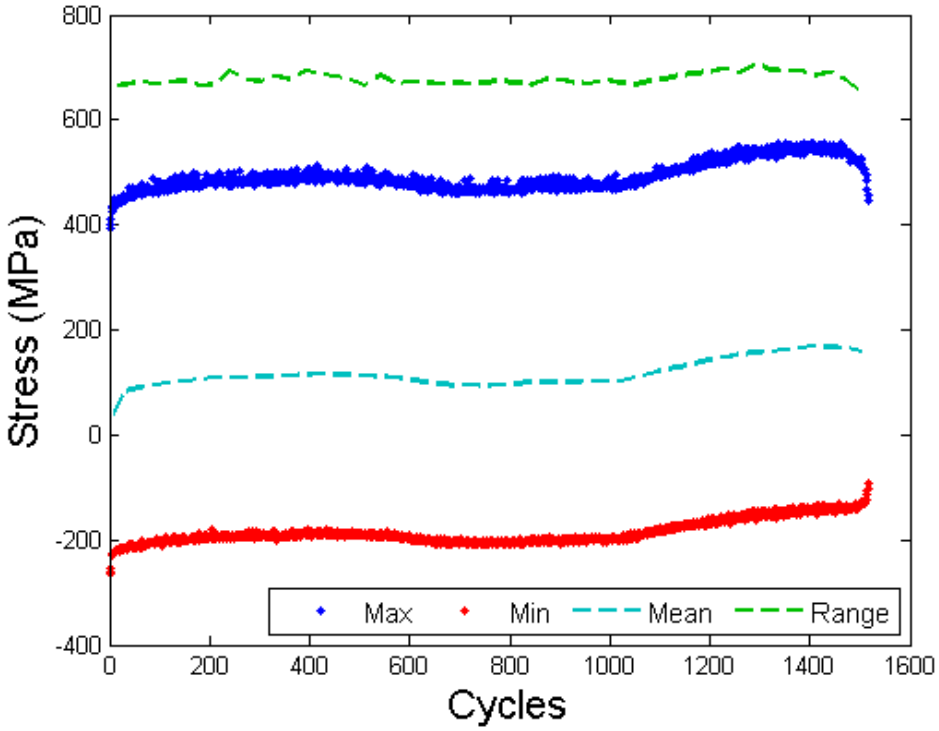

Figure 4.21: Stress History for Coated Specimen, $\Delta\varepsilon_{mech}$ = 0.7%

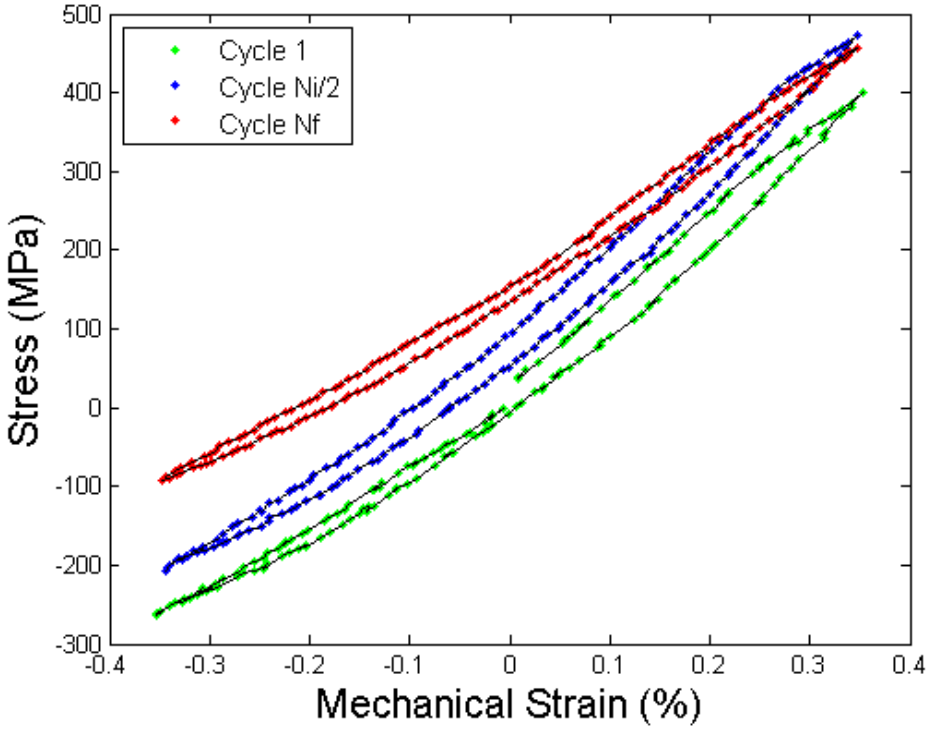

Figure 4.22: Hysteresis Loops for Coated Specimen, $\Delta\varepsilon_{mech}$ = 0.7%

4.3.4: Mechanical Strain Range 0.8%

The stress history and hysteresis loops for the uncoated specimen with $\Delta\varepsilon_{mech}$ = 0.8% are displayed in Figure 4.23 and Figure 4.24, respectively. The stress range remained essentially constant slightly under 800 MPa, while the mean stress slowly increased throughout the beginning of the test to a value near 200 MPa. As seen with the other tests, the hysteresis loop from the first cycle essentially shifted upwards until stabilization before the stress range began to decrease.

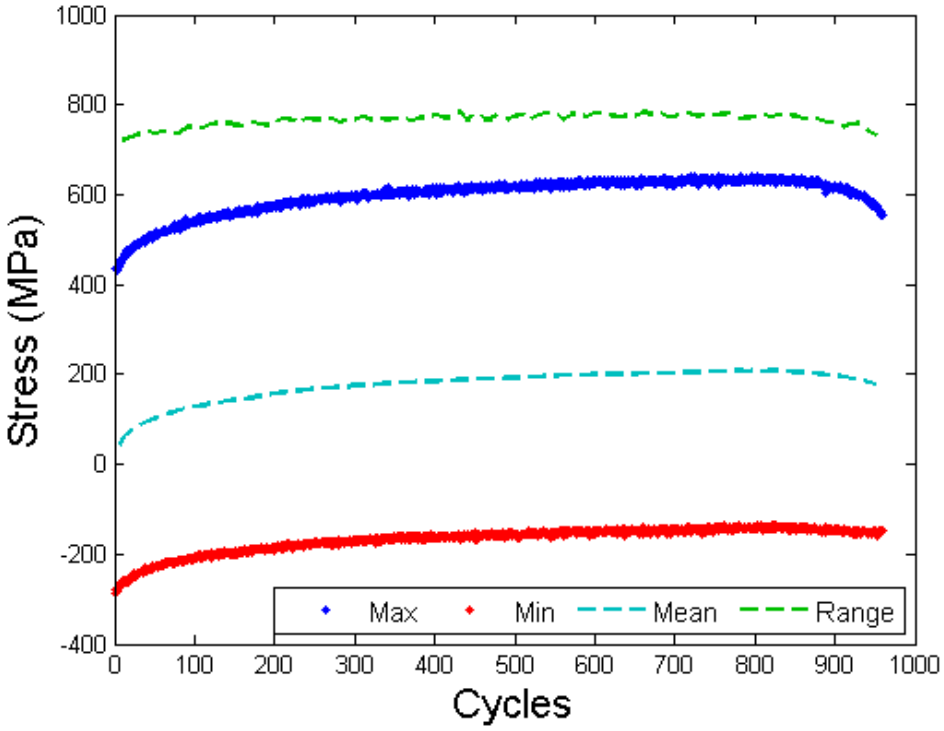

Figure 4.23: Stress History for Uncoated Specimen, $\Delta\varepsilon_{mech}$ = 0.8%

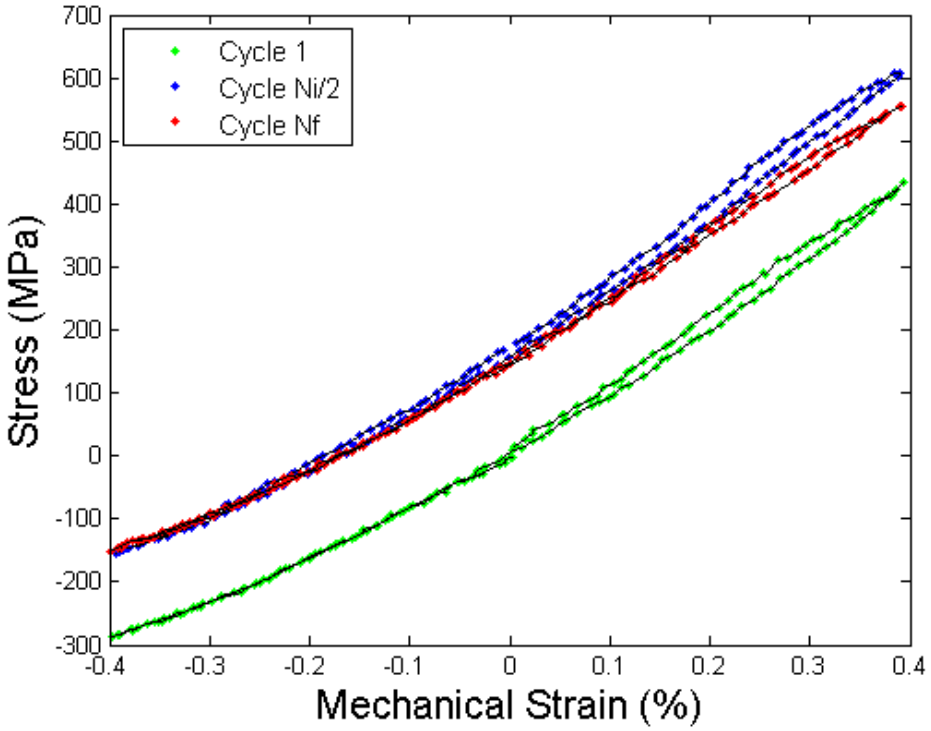

Figure 4.24: Hysteresis Loops for Uncoated Specimen, $\Delta\varepsilon_{mech}$ = 0.8%

Figure 4.25 and Figure 4.26 display the stress history and hysteresis loops for the coated specimen with $\Delta\varepsilon_{mech}$ = 0.8%. Initially, the first-cycle stresses and stress range were the same as those for the uncoated specimen. However, the test stopped and had to be restarted after 240 cycles. The mean stress initially appeared as if it would stabilize near 100 MPa, but after restarting, it stabilized at about 200 MPa. After restarting the test, the stress range was almost 100 MPa higher than the initial value. Overall, the coated specimen lasted 489 cycles longer than the uncoated specimen before crack initiation; however, it must be understood that this data is not truly representative due to the test shut down. As can be seen from the final cycle hysteresis loop, the tensile load-bearing capacity was extremely low due to the very large crack at the end of the test.

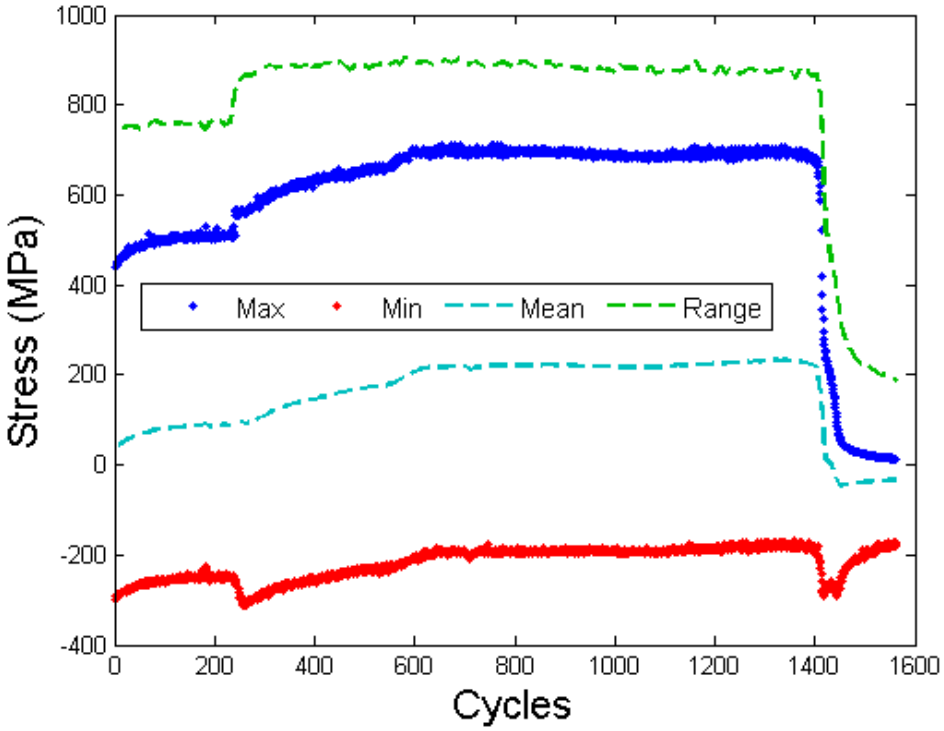

Figure 4.25: Stress History for Coated Specimen, $\Delta\varepsilon_{mech}$ = 0.8%

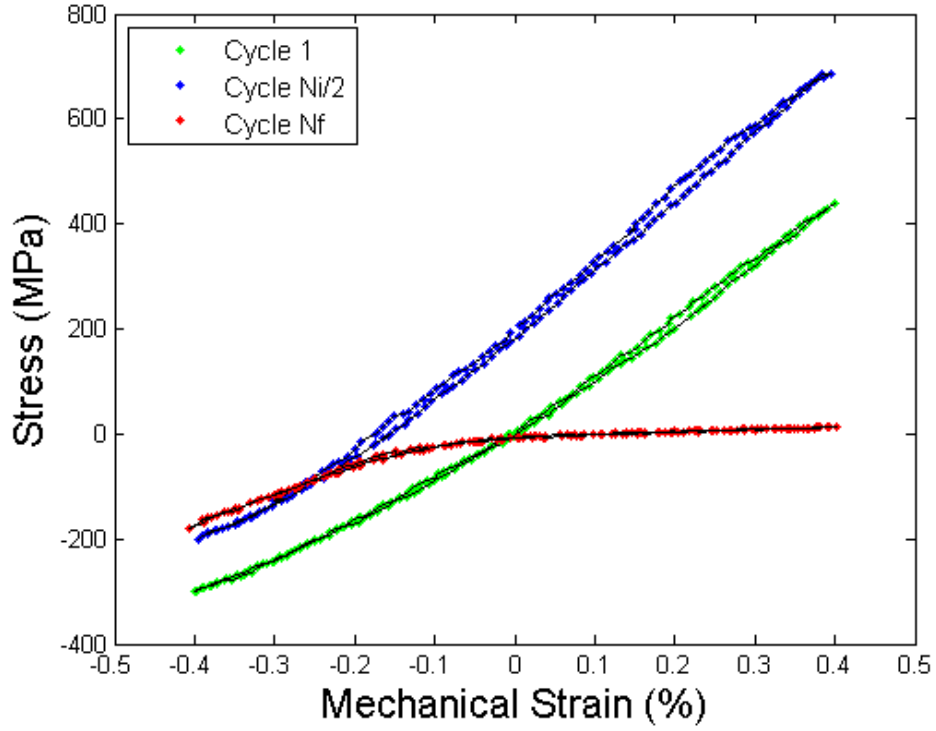

Figure 4.26: Hysteresis Loops for Coated Specimen, $\Delta\varepsilon_{mech}$ = 0.8%

4.3.5: Mechanical Strain Range 0.9%

The stress history and hysteresis loops for the uncoated (Figure 4.27 and Figure 4.28, respectively) and coated (Figure 4.29 and Figure 4.30, respectively) specimens with $\Delta\varepsilon_{mech}$ = 0.9% can be found below. Both tests showed a virtually identical stress evolution with a stress range of about 900 MPa and a stabilized mean stress of about 200 MPa. For the uncoated specimen, the load drop was not captured before fracture, but the time at which crack initiation occurred could be found from the slight jump in tensile load before fracture. This was most likely due to the crack initiation and fracture occurring slightly outside of the extensometer rods. The discontinuities in both first-cycle hysteresis loops indicate that the hardening behavior was accentuated due to the higher applied strain range, so the hysteresis loops shifted upwards faster than those in the other tests. For this mechanical strain range, the coated specimen had a crack initiation life 152 cycles longer than the uncoated specimen.

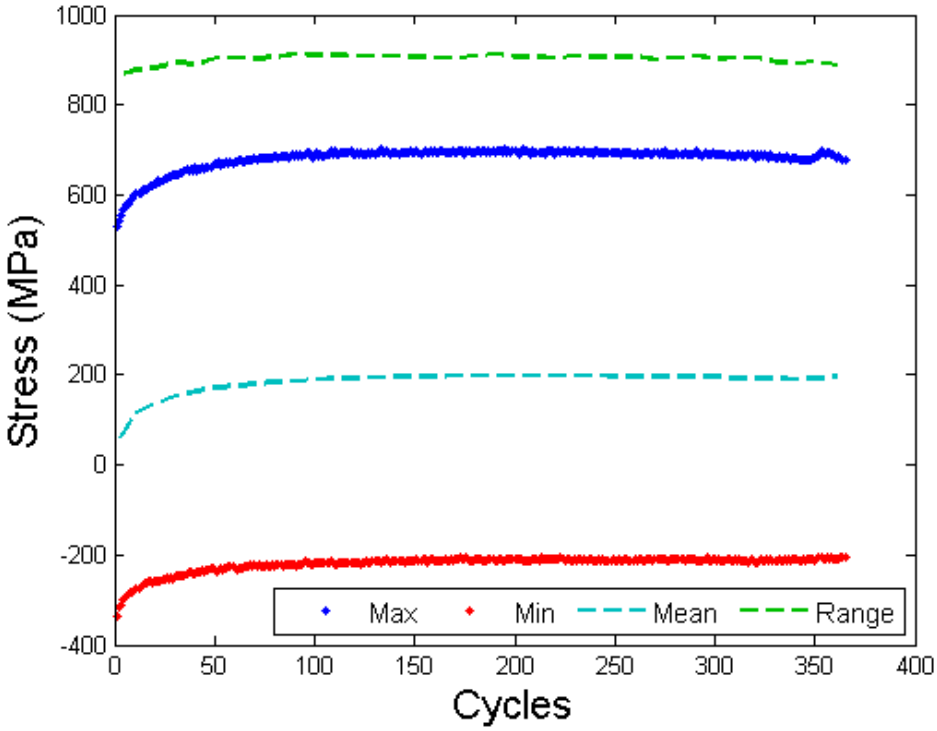

Figure 4.27: Stress History for Uncoated Specimen, $\Delta\varepsilon_{mech}$ = 0.9%

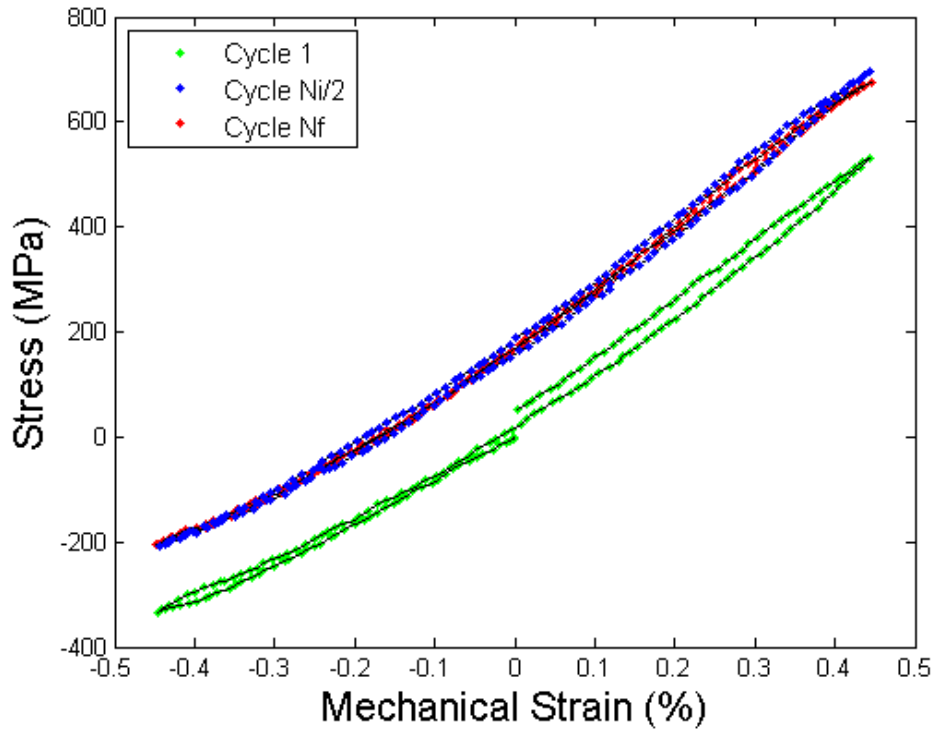

Figure 4.28: Hysteresis Loops for Uncoated Specimen, $\Delta\varepsilon_{mech}$ = 0.9%

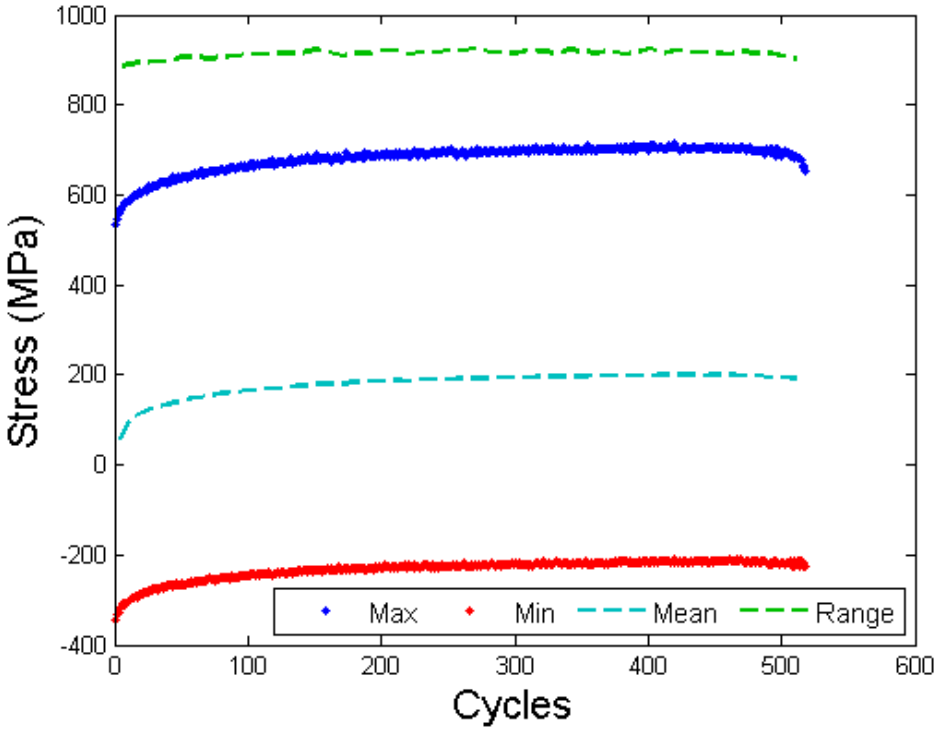

Figure 4.29: Stress History for Coated Specimen, $\Delta\varepsilon_{mech}$ = 0.9%

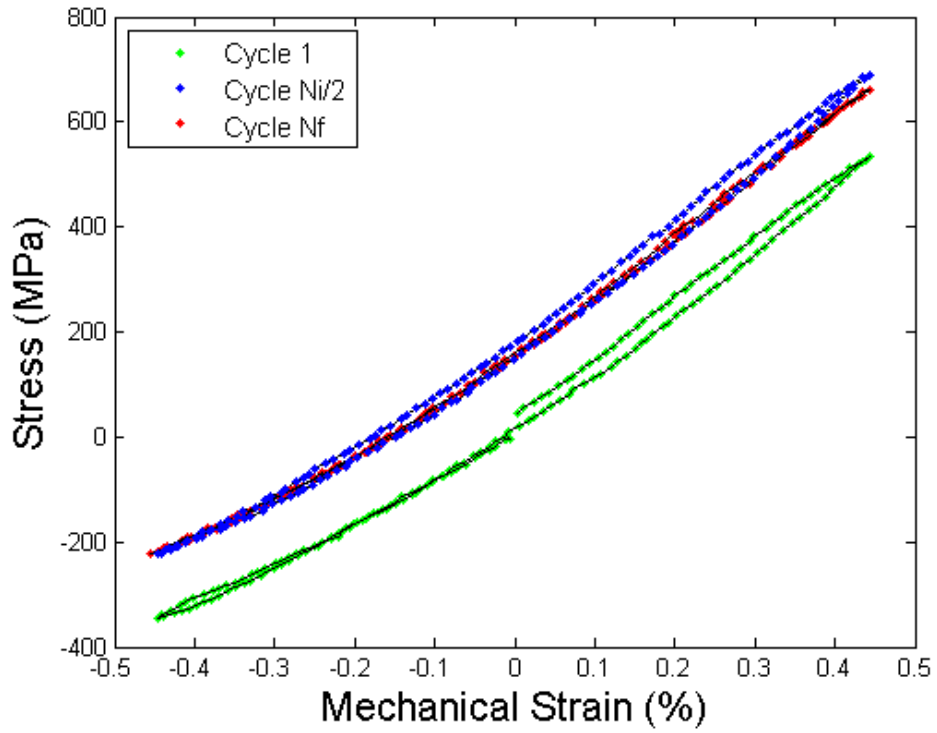

Figure 4.30: Hysteresis Loops for Coated Specimen, $\Delta\varepsilon_{mech}$ = 0.9%

SEM images from the fracture surface of the coated specimen with $\Delta\varepsilon_{mech}$ = 0.9% are shown below. As expected from the very small load drop before fracture, Figure 4.31 most likely shows a large region of fast fracture along crystallographic planes. No clear crack initiation point in the base metal could be found. It is believed the initial crack occurred in many places in the coating before propagating into the alloy. The distinct cracking behavior in the coating on the outer surface of the specimen can be seen in Figure 4.32.

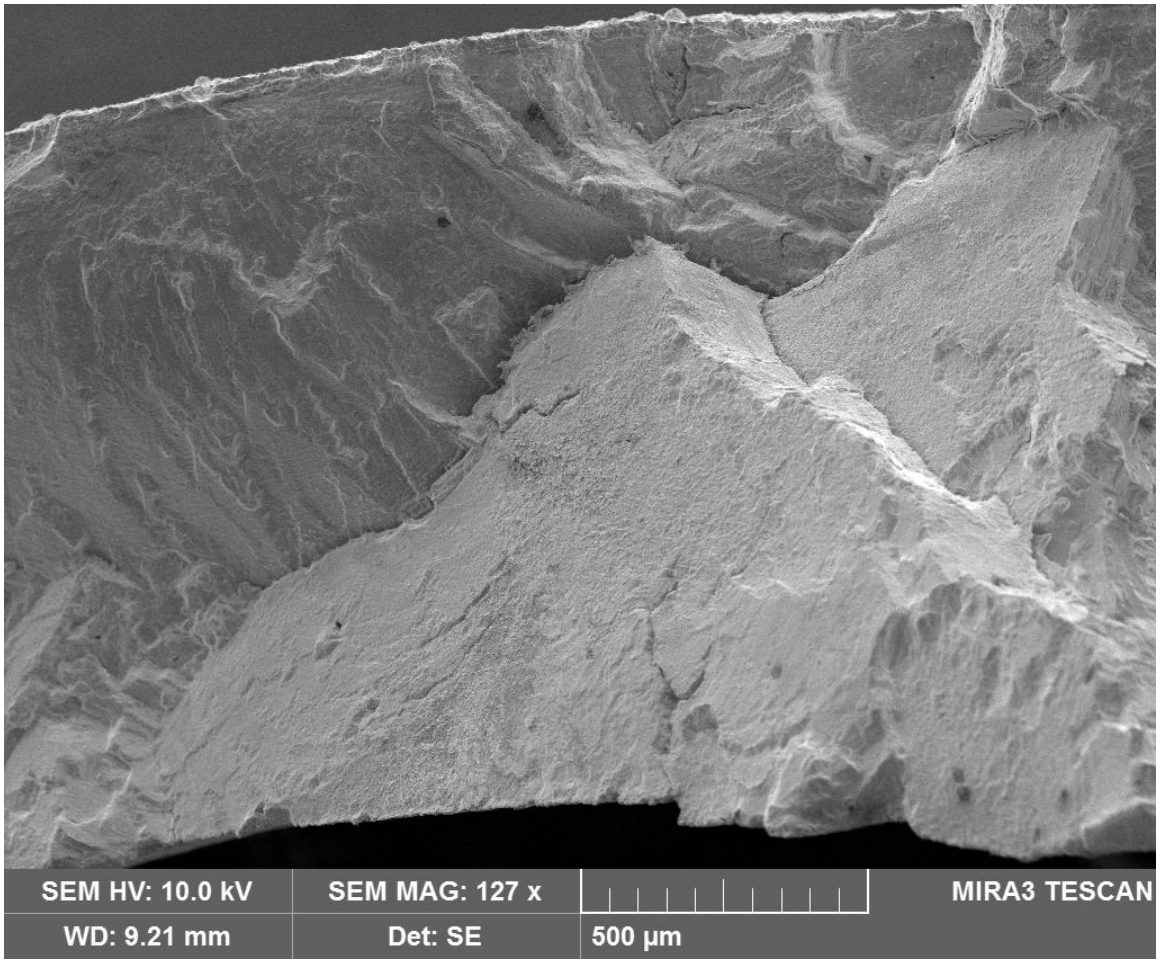

Figure 4.31: SEM Image Showing Crystallographic Fracture Planes on the Fracture Surface of Specimen 5111AA-09-2 (Coated with $\Delta\varepsilon_{mech}$ = 0.9%)

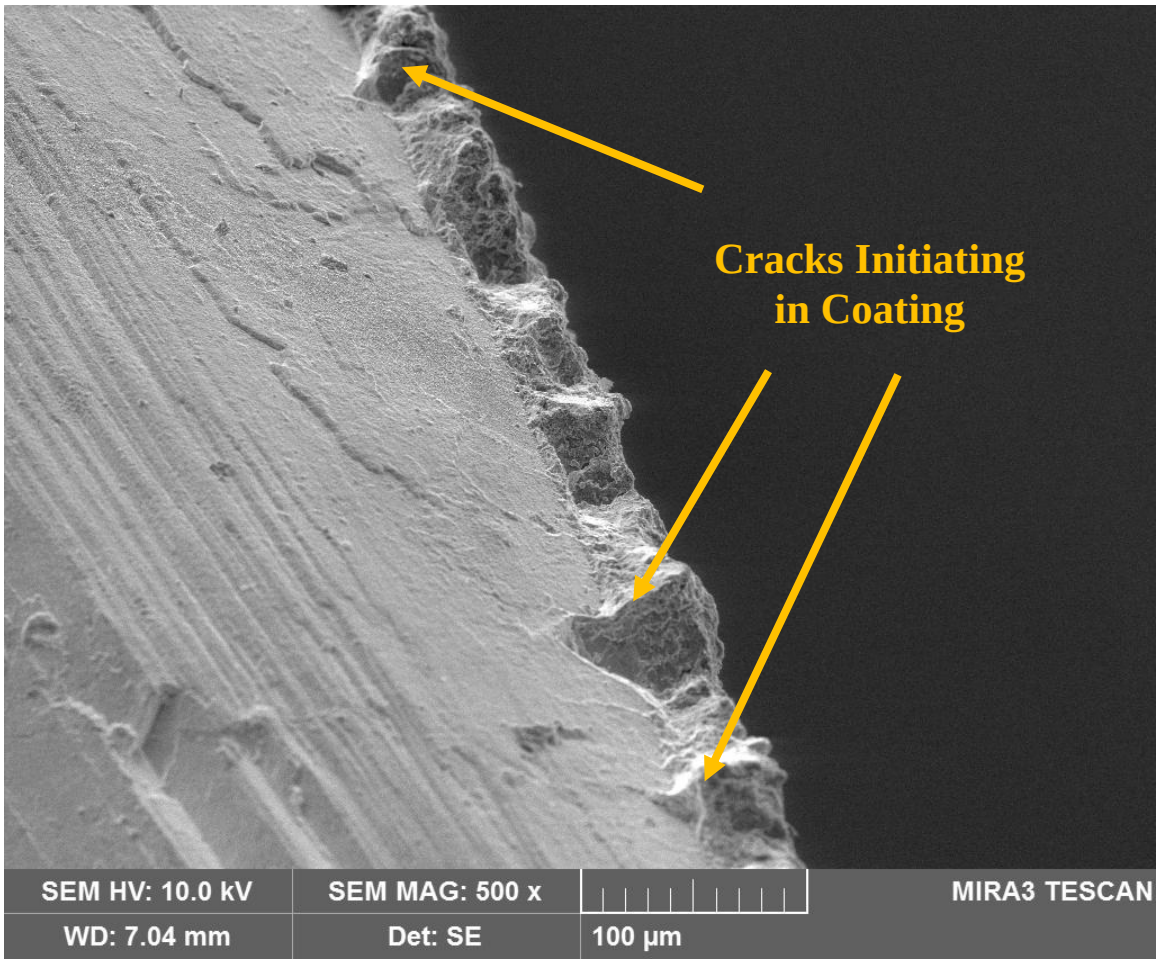

Figure 4.32: SEM Image Showing Cracking Behavior in the Coating of Specimen 5111AA-09-2 (Coated with $\Delta\varepsilon_{mech}$ = 0.9%)

4.3.6: Discussion

The same type of hardening behavior was seen for each test, both coated and uncoated. The mean stress always gradually increased to 100-200 MPa, and the stress ranges were essentially constant throughout the duration of the test before crack initiation, and as expected, the stress range was larger with a larger applied mechanical strain range. In all cases, the stress vs. mechanical strain hysteresis loop essentially shifted upwards with a slowly increasing mean stress until stabilization. Similar stress

evolution behavior was observed by Buchholz *et al*. [85] for OP TMF testing between 750-950°C. When crack initiation occurred, the maximum stress began to shift towards zero. After extensive cracking, a sharp bend in the hysteresis loops occurred at zero load, and very little tensile force was applied to reach the desired positive mechanical strain. It appeared as though the tests with higher mechanical strain ranges were more prone to fast fracture before extensive crack growth occurred.

For the $\Delta\varepsilon_{mech}$ = 0.5% tests, the life results seemed to agree with those found by Tamarin *et al*. [5] in which coated specimens experienced a severely shortened life when compared to uncoated specimens; the lives were at least halved, depending on the type of coating. However, for each of the other mechanical strain ranges, the coating seemed to provide a marginal improvement in TMF life of a few hundred cycles. There is a chance this may just be due to scatter in the data; in either case, the rest of the results seem to agree with those found by Wood *et al*. [3] and Gayda *et al*. [26], where no significant discrepancy in life was observed between coated and bare specimens. Due to the relatively long cycle time, more severe oxidation damage may occur in the uncoated specimens immediately, so the coating may provide a small positive shift in lives despite the early cracking behavior. However, the exact trade-off is not explicitly clear and may be strain-dependent, but the coating does clearly appear to provide some small benefit in life. More testing of both specimen types at identical strain ranges is required to determine the statistical variation in the lives and find if the differences observed here are actually significant.

4.4: Comparison of Results

Figure 4.33 displays a strain-life plot of mechanical strain range vs. cycles to crack initiation (N_i) for the tests described above with the modified hollow specimens, with a comparison to the results obtained by Amaro [14] with solid specimens. All tests shown here were conducted under identical temperature ranges and cycle times. The life for the uncoated hollow specimen at $\Delta\varepsilon_{mech}$ = 0.5% was longer than that obtained for a solid specimen, and the life at $\Delta\varepsilon_{mech}$ = 0.9% was shorter. However, on the whole, the lives for both coated and uncoated specimens lie well within the range that would be expected based on Amaro's data. These results indicate that there is little, if any, effect of the specimen geometry on TMF test results under the conditions explored.

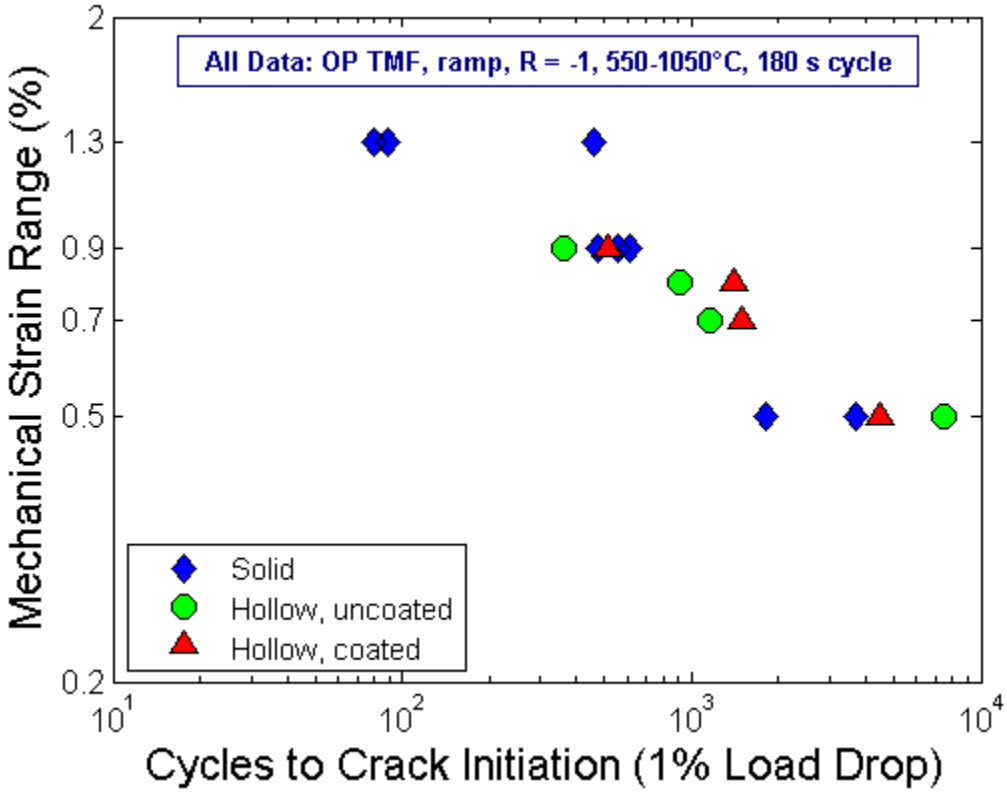

Figure 4.33: Comparison of TMF Lives to Previous Testing with Solid Specimens

Figure 4.34 displays a plot of the hollow specimen strain-life results compared to the typical data ranges obtained by Pratt & Whitney (P&W) for both coated and bare specimens of the same geometry. However, the Pratt & Whitney tests used temperatures of 427-1038°C with a 60 second cycle time. In this case, a 50% load drop is used for the failure criterion; for tests in which this did not occur before fracture, the final cycle count N_f was plotted. For each mechanical strain range, Pratt & Whitney reported longer lives for the uncoated specimens, although there was a slight overlap for $\Delta\varepsilon_{mech}$ = 0.6%. Except for the coated specimen with $\Delta\varepsilon_{mech}$ = 0.8%, each of the other tests performed at Georgia Tech (GT) showed a shorter life than the corresponding Pratt & Whitney data range.

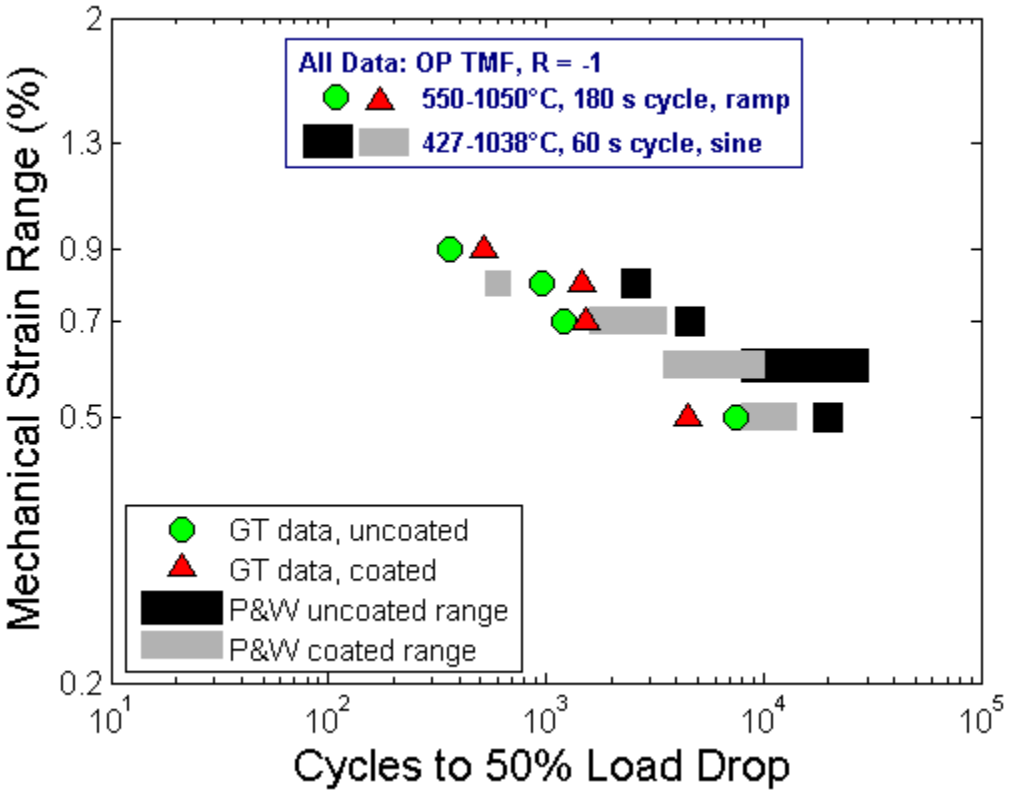

Figure 4.34: Comparison of Hollow Specimen Data to Pratt & Whitney Data

Several possibilities exist for the differences in the data. Since the Georgia Tech testing used a longer cycle time, there was the possibility of more environmental damage during each cycle, which would reduce the overall life; in addition, this would make the coating relatively more beneficial, explaining the absence of the life advantage for uncoated specimens. On the other hand, the faster Pratt & Whitney cycle time may reduce the effects of creep and oxidation, so the early cracking of the coating would clearly cause the lives of coated specimens to be shorter. Testing performed by Andersson and Sjostrom [99] exhibited decreasing life with decreasing heating/cooling rates (meaning increasing cycle time), supporting this hypothesis.

The higher minimum temperature and lower temperature range used for Georgia Tech testing may also cause the life differences. Not only is isothermal fatigue life reduced at higher temperatures, but testing observed by Loveday *et al*. [94], for example, showed an increase in life at increasing temperature ranges. Also, at all times during the test, the temperature for the Georgia Tech cycle would be higher. This would greatly increase the relative rate of oxidation, especially at the low temperature end of the cycle. Regardless, more testing is required to find the exact source of the TMF life discrepancies, but it appears as though the difference in specimen geometry, test machine, and operator have been eliminated.

CHAPTER 5

CONCLUSIONS

5.1: Overall Conclusions

The goal of this research was to investigate the differences in thermo-mechanical fatigue crack initiation lives of PWA 1484 caused by specimen geometry and coating. Previous testing had been performed at both the MPRL of Georgia Tech (with solid specimens, a cycle time of 180 seconds, temperatures 550-1050°C, and a ramp waveform) and Pratt & Whitney (with hollow specimens of a larger cross-sectional area, a cycle time of 60 seconds, temperatures 427-1038°C, and a sinusoidal waveform). Modifications were made to the ends of the specimens and other components were produced to allow the buttonhead specimens to be gripped by collet grips. Hand calculations and finite element analysis were performed to ensure the success of the modified gripping mechanism. Mechanical strain-controlled TMF tests were performed under the previous Georgia Tech cycle conditions on the coated and uncoated modified hollow specimens. The results of the TMF tests were compared to the previous data obtained at Georgia Tech using solid specimens in order to check for internal consistency with varying specimen geometries. The primary conclusions of this research are as follows:

- It was determined the designed gripping method would not damage the specimen or affect test results.
- The modified gripping method proved to provide successful TMF results.

- For the lowest applied mechanical strain range, the coated specimen showed a 40% deficit compared to the crack initiation life of the uncoated specimen. For each of the higher strain ranges, the coated specimens exhibited an improvement between 29% and 53% in life. Not enough data was obtained to say conclusively, but it appears the coating offers a marginal improvement in TMF life for a three minute cycle time.
- For the coated specimens, as predicted, several cracks initiated in the coating before propagating into the base metal.
- The test results for the hollow specimens did not exhibit significant differences from the trends showed by the previous solid specimen testing at Georgia Tech. Therefore, specimen geometry has effectively been eliminated as a primary cause in the differences in life results between Georgia Tech and Pratt & Whitney.
- The hollow specimen test results still showed significant life differences from the Pratt & Whitney data. The root cause of the differences must come from one or more other possible sources.

5.2: Recommendations for Future Work

Additional tests should be run with coated and uncoated specimens of PWA 1484 at identical mechanical strain ranges to further explore the effects of the coating and to determine the main causes of the TMF life differences between Georgia Tech and Pratt & Whitney. Some of this testing is currently ongoing. One testing variable should be changed at a time so that the relative effects can be observed. As the results have been shown to be essentially specimen-independent, these tests may be performed with the

smaller conventional solid round bar specimens used for previous testing to reduce cost, time, and effort in the preparations. The following tests are recommended:

- The 550-1050°C, 180 second cycle with at least two of the mechanical strain ranges examined in this work should be used to get a better idea of the scatter in the TMF data and verify the marginal life benefit provided by the coating that was observed here.
- Tests with a 60 second cycle (if possible) with temperatures 550-1050°C would isolate the effects of cycle time on the TMF behavior.
- Tests with a 180 second cycle with temperatures 427-1038°C would isolate the effects of the different temperature range on the TMF behavior.
- Tests with a 60 second cycle (if possible) with temperatures 427-1038°C should be run to exactly imitate the Pratt & Whitney cycle conditions.

It is unlikely that a 60 second cycle is obtainable while conforming to ASTM standards without internal forced air cooling of hollow specimens. However, a longer cycle time could be used to identify any possible trends in TMF life based on cycle time. In addition, the effects of waveform (ramp vs. sine) on test results should be explored.

Finally, additional microscopy could be conducted on the bare and coated specimens used for testing in this work to determine the exact damage mechanisms that occurred for each strain range and gain a better understanding of the relative influences of creep, oxidation, and fatigue. Similar microscopy should also be conducted on any future testing to determine the effects of cycle time, temperatures, and/or waveform on the damage mechanisms.

APPENDIX A

PART DRAWINGS IN ENGLISH UNITS

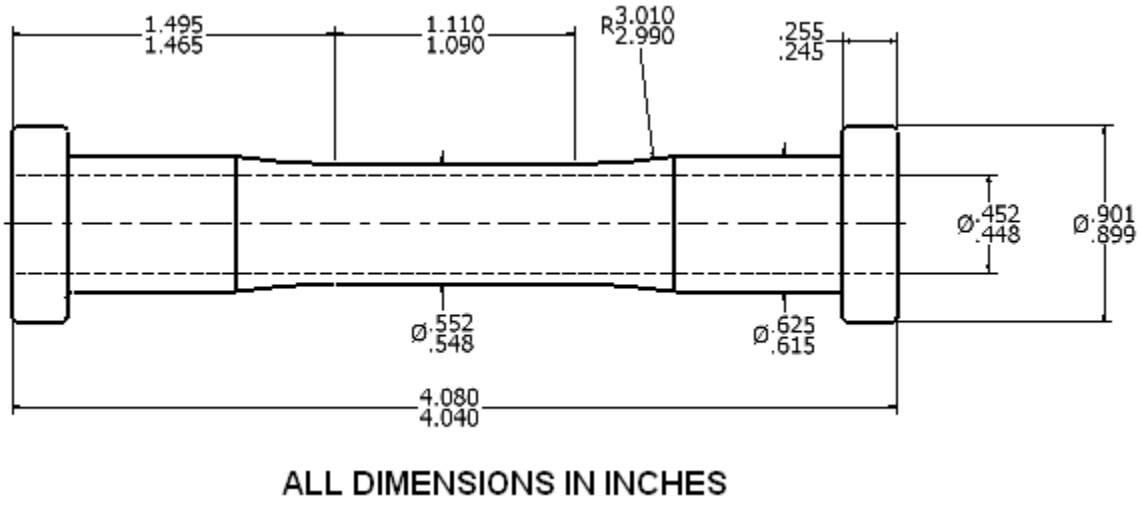

Figure A.1: Drawing of the Original Specimen with Critical Dimensions (Inches)

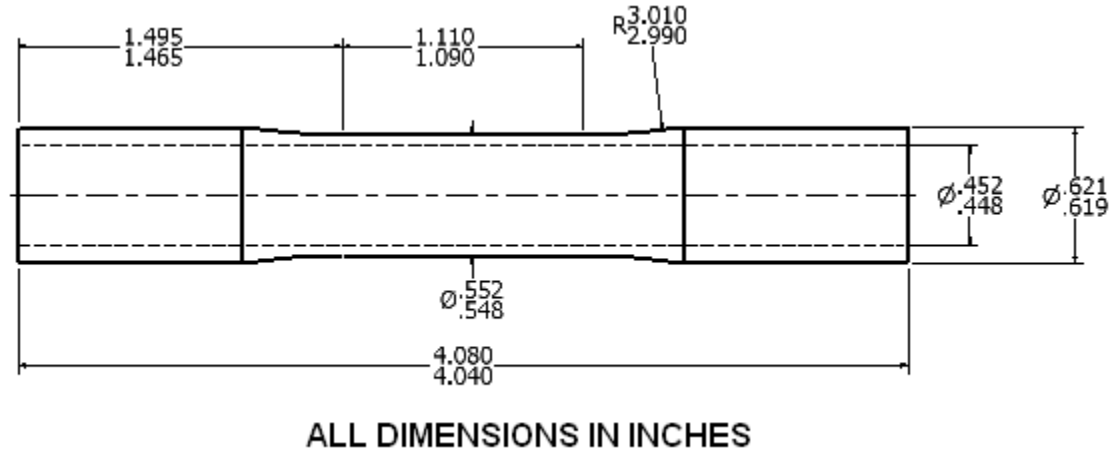

Figure A.2: Drawing of the Modified Specimen with Critical Dimensions (Inches)

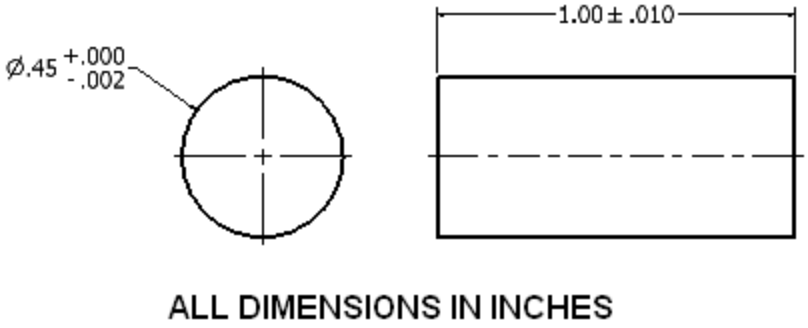

Figure A.3: Drawing of a Plug (Dimensions in Inches)

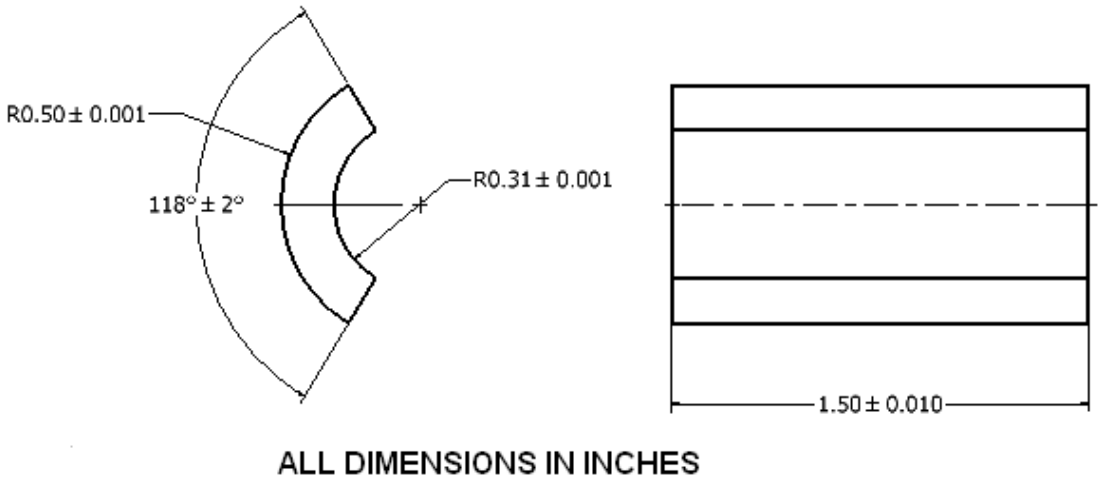

Figure A.4: Drawing of a Collet Adapter (Dimensions in Inches)

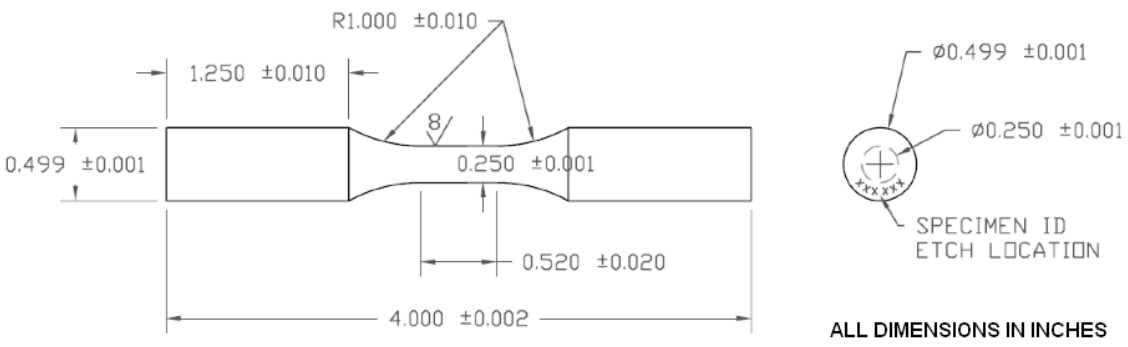

Figure A.5: Drawing of Solid Cylindrical Specimens Used for Previous Testing [14]

APPENDIX B

SPECIMEN QUALITY INSPECTIONS

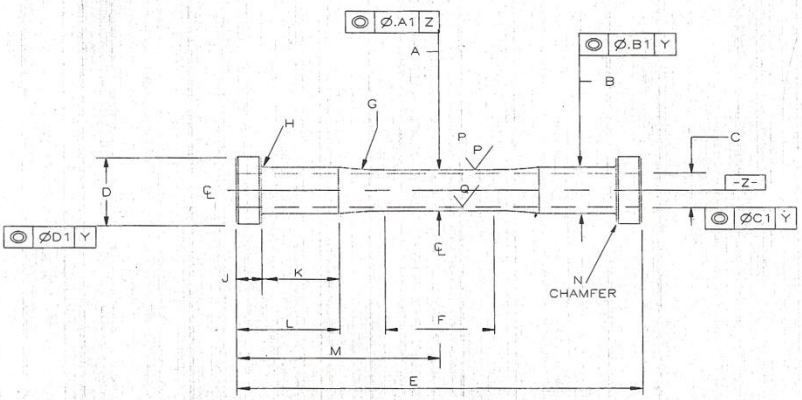

METCUT RESEARCH
CINCINNATI, OH

Job Number:
760-92992-10-128-02-02

Drawing Number:
MT 41 UNCOATED

Material:
PWA 1484 Single Crystal

Insp C. Brick

Date: 13-Sep-12

Total Lot Size	Inspection Lot Size
15	15

Spec. Serialized: YES

Finish Inspected: 100

Test at Metcut: NO

Amt. of Nonconforming
NONE

Page 1 of 3

form : 65-03-01

Specimen Number: 5111AA-02-1

Drawing Dimension		Measured Dimension	Out-of-Tolerance
A	.552/.548	As Rec.	
A1	<.0015	As Rec.	
B	.625 / .615	As Rec.	
B1	<.0015	As Rec.	
C	.443 / .441	0.4495	
C1	<.0015	As Rec.	
D	.901 / .899	As Rec.	
D1	<.0015	As Rec.	
E	4.060 +/- .010	As Rec.	
F	1.100 +/- .010	As Rec.	
G	3.000 +/- .010	As Rec.	
H	.020 +/-.005	As Rec.	
J	.250 +/- .005	As Rec.	
K	.773 +/- .005	As Rec.	
L	1.023 Ref.	As Rec.	
M	2.030 Ref.	As Rec.	
N	.025 +/- .005	As Rec.	
P	8 Ra	As Rec.	
Q	8Ra	As Rec.	
Dish		As Rec.	

Comment: Job was MFG to drawing (coated) then returned onMFG to(uncoated)drawing. Spec.'s were peened per drawing.

Revised:12-21-06

Figure B.1: Initial Specimen Quality Inspection (Page 1)

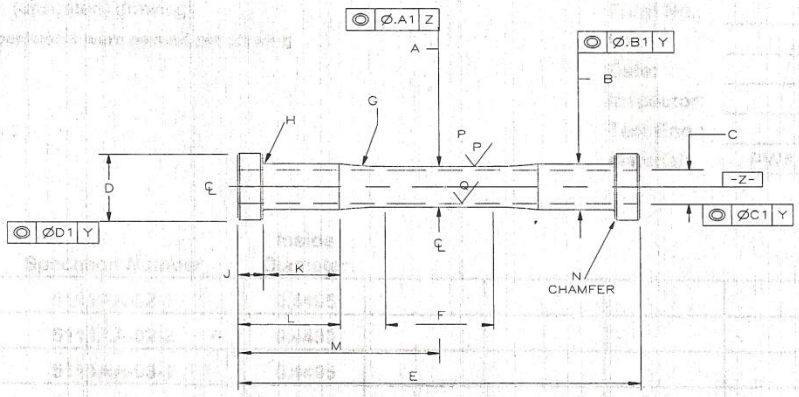

METCUT RESEARCH
CINCINNATI, OH

Job Number:
760-92992-10-128-02-02

Drawing Number:
MT 41 UNCOATED

Material:
PWA 1484 Single Crystal

Insp C. Brick

Date: 13-Sep-12

Total Lot Size	Inspection Lot Size
15	15

Spec. Serialized: YES

Finish Inspected: 100

Test at Metcut: NO

Amt. of Nonconforming
NONE

Page 2 of 3
form : 65-03-01

Specimen Number: 5111AA-10-1

Drawing Dimension		Measured Dimension	Out-of-Tolerance
A	.552/.548	As Rec.	
A1	<.0015	As Rec.	
B	.625 / .615	As Rec.	
B1	<.0015	As Rec.	
C	.443 / .441	0.4495	
C1	<.0015	As Rec.	
D	.901 / .899	As Rec.	
D1	<.0015	As Rec.	
E	4.060 +/- .010	As Rec.	
F	1.100 +/- .010	As Rec.	
G	3.000 +/- .010	As Rec.	
H	.020 +/-.005	As Rec.	
J	.250 +/- .005	As Rec.	
K	.773 +/- .005	As Rec.	
L	1.023 Ref.	As Rec.	
M	2.030 Ref.	As Rec.	
N	.025 +/- .005	As Rec.	
P	8 Ra	As Rec.	
Q	8Ra	As Rec.	
Dish		As Rec.	

Comment: Job was MFG to drawing (coated) then returned onMFG to(uncoated)drawing. Spec.'s were peened per drawing.

Revised:12-21-06

Figure B.2: Initial Specimen Quality Inspection (Page 2)

METCUT RESEARCH INC.

QUALITY INSPECTION SUMMARY

Job wasMFG to (coated) drawing then returned to MFG on (uncoated) drawing-

Specimen's were peened per drawing

Job No.:	**760-92992-10-128-02-02**
Form No.:	**65-00-04**
Lot:	**15**
Date:	**13-Sep-12**
Inspector:	**C. Brick**
Test Eng.:	**NA**
Material:	**PWA 1484 Single Crystal**

Specimen Number	Inside Diameter						
5111AA-02-1	0.4495						UC
5111AA-02-2	0.4490						UC
5111AA-03-1	0.4495						UC
5111AA-03-2	0.4495						UC
5111AA-04-1	0.4495						UC
5111AA-04-2	0.4495						UC
5111AA-06-1	0.4495						UC
5111AA-06-2	0.4490						UC
5111AA-07-1	0.4495						C
5111AA-07-2	0.4495						C
5111AA-08-1	0.4495						C
5111AA-08-2	0.4495						C
5111AA-09-1	0.4480						C
5111AA-09-2	0.4495						C
5111AA-10-1	0.4495						C

8 Specimens uncoated + HT + I.D. honed

7 Specimens coated + HT + I.D. honed

Metcut Research Inc. · 3980 Rosslyn Drive · Cincinnati, OH 45209-1196
Tel (513) 271-5100 · Fax (513) 271-9511

Revised : 01/07/98

Figure B.3: Initial Specimen Quality Inspection (Page 3)

element

FINAL INSPECTION REPORT

CUSTOMER	Georgia Tech
CONTACT	Sreve Antolovich
PURCHASE ORDER #	1800103784
MATERIAL TYPE	PWA 1484
DRAWING #	MT-41
MTI JOB #	476-0010-01
QUANTITY	15
DATE	12/4/2012
INSPECTOR	Russ Rathnow
NONCONFORMANCE	No
SPECIMEN #	
NOTIFICATION	

INSTRUMENT USED		1-490	Per Proc.	5-CCM-001
NC	ID#	Diameter 0.620 +/-.005	32 RMS As Ground	CONCENTRICITY Diameter .001
	5111AA-02-1	0.6209 0.6206	✓	✓
	5111AA-02-2	0.6198 0.6201	✓	✓
	5111AA-03-1	0.6197 0.6200	✓	✓
	5111AA-03-2	0.6195 0.6192	✓	✓
	5111AA-04-1	0.6195 0.6194	✓	✓
	5111AA-04-2	0.6199 0.6195	✓	✓
	5111AA-06-1	0.6195 0.6193	✓	✓
	5111AA-06-2	0.6209 0.6202	✓	✓
	5111AA-07-1	0.6205 0.6197	✓	✓
	5111AA-07-2	0.6201 0.6201	✓	✓
	5111AA-08-1	0.6189 0.6185	✓	✓
	5111AA-08-2	0.6183 0.6186	✓	✓
	5111AA-09-1	0.6207 0.6205	✓	✓
	5111AA-09-2	0.6196 0.6205	✓	✓
	5111AA-10-1	0.6203 0.6205	✓	✓

COMMENTS:

Figure B.4: Quality Inspection for Specimen Gripping Diameter Modification

APPENDIX C

DETAILED TMF TESTING PROCEDURE

The following lists contain the finalized testing procedure (both start-up and shut-down) used to perform the OP TMF experiments with a ramp waveform and a three-minute cycle. Especially important steps are emphasized in bold red lettering. This procedure is very specific to the test frame, computer, and software used for these tests.

TMF Test Start-Up Procedure

- Prepare specimen
  - Measure dimensions
  - Mark location for the thermocouple (1.45" from the end)
  - Spot weld thermocouple wires to the marked location (if necessary, gently sand off small spot to expose specimen surface)
    - Welder settings: switch to high, #1 button, knob to 1:00 position
  - Clean the ends with ethanol
  - Mark grip locations (0.65" from ends)
- Clean grips
  - Wipe down the insides of collets with ethanol
  - Clean surfaces of collet adapters with ethanol (if necessary, first smooth out the surfaces with sandpaper)
- Start up machine
  - If necessary, turn on main hydraulic pump (first turn to low, then wait about 30 seconds, then turn to high)
  - Open Station Manager (2013_1_9_withvirtual.cfg: nickel_super_alloy_9_12)
  - **Set interlocks**
    - **Force: upper = 500 lb, lower = -500 lb**
    - **Displacement: upper = 0.75", lower = 0.1"**
  - **Set control mode to CLC Axial**
  - Turn HPU and HSM controls to low, then to high after a few seconds
  - Warm up machine - use Basic TestWare (file: **warm_up.tst**)
    - **CLC Axial** control mode, setpoint = 0.4", amp. = 0.28", freq. = 0.5 Hz, sine waveform
    - Run for at least approximately 10 minutes

- Insert specimen
  - Set lower grip displacement to 0.7" (**CLC Axial**)
  - If necessary, unlock the upper grip, raise it up, and lock again
  - Hold 3 adapters in upper collet grip by hand, and put specimen between them into the upper grip
  - Tighten upper grip by hand
  - Set lower grip displacement to 0.2" (**CLC Axial**)
  - Put 3 adapters in lower collet grip
  - Unlock the upper grip, and lower with the specimen through the coil until the specimen is inserted into the lower grip
    - Make sure to maintain alignment of adapters and constantly check the force meter (should read about -100 lb while upper grip is unlocked)
  - Lock the upper grip and reset the Program interlock
  - Tighten lower grip by hand
  - Pressurize upper and lower grips (close the release knobs, then open the pressure knobs)
    - Inside the box: top gauge should read about 5500-6500 psi, lower gauge (near knob) should read just below 40 psi
  - **Set control mode to Force, set to 0 lb**
  - Center coil around specimen
  - Plug thermocouple into temperature controller
  - **Set interlocks**
    - **Force: upper = 5,000 lb, lower = -5,000 lb**
    - **Displacement: upper = 0.35", lower = 0.15"**
- Attach extensometer
  - Calibrate extensometer if necessary
  - Adjust position of the support if necessary (need enough spring force)
  - Install the extensometer (using the gage block for spacing)
    - Make sure rods are centered horizontally on the specimen
    - Gently use fingers try to wiggle the rods (horizontally, vertically, and twisting) and make sure they don't move
  - Attach screen to front of test fixture to shield the specimen from air moving within the laboratory
  - Zero strain (then record the offset)
  - Make sure extensometer is seated well (**file: extensometer_check.tst**)
    - Run a force control test (fully elastic range) at a faster frequency than during the actual test
    - **Force** control, setpoint = 0 lb, amp. = 2000 lb (may need to lower for coated specimens), freq. = 0.1 Hz, ramp waveform
    - Scope: time plot of Axial Force and Axial Strain 1 – strain should cross 0 at the same time as the force
    - Let it run for about 20 cycles, until satisfied

- Check room temperature modulus
  - Run modulus check test (file: **modulus_check.tst**)
    - **Force** control, setpoint = 0 lb, amp. = 2000 lb for uncoated specimens or 800 lb for coated specimens, freq. = 0.03 Hz, sine waveform
      (if results are unsatisfactory, increase frequency to up to 0.167 Hz)
    - Run for 3 cycles
    - Scope: X/Y plot, Y = Axial Force, X = Axial Strain 1
  - Copy data to Excel file (modulus_check.xlsx)
  - Record modulus from linear fit of stress-strain plot
- Increase the temperature and check the modulus (at least at the minimum, mean, and maximum test temperatures should be checked)
  - **Turn on water to grips and induction heater**
  - Turn on the temperature controller and set mode to Auto
  - Turn on heater and hit start button (after letting water flow for a bit)
  - Increase temperature to the desired temperature (file: **temp_set.tst**)
    - **Temp FDBK** control mode, ramp to desired temp in 90 seconds
    - **Force** control, ramp to 0 lb in 90 seconds
  - Run modulus check test (file: **modulus_check.tst**)
    - **Force** control, setpoint = 0 lb, amp. = 2000 lb for uncoated specimens or 800 lb for coated specimens, freq. = 0.03 Hz, sine waveform
      (if results at temperature are unsatisfactory, increase to 0.167 Hz)
    - Run for 3 cycles
    - Scope: X/Y plot, Y = Axial Force, X = Axial Strain 1
  - Copy data to Excel file (modulus_check.xlsx)
  - Record modulus from linear fit of stress-strain plot
  - Repeat for all desired temperatures
- Perform thermal strain fit
  - If necessary, set the temperature to the mean temperature (file: **temp_set.tst**)
    - **Temp FDBK** control mode, ramp to mean temp in 90 seconds
    - **Force** control, ramp to 0 lb in 90 seconds
  - Record the total strain, and then zero it (also record the new offset)
  - Run thermal cycling test (file: **thermal_cycling.tst**)
    - Adjust temperature setpoints (and tune controller if necessary) so that end points are correct
    - **Temp FDBK** control mode, freq. = 0.333 cpm, ramp waveform
    - **Force** control, setpoint = 0 lb, amp. = 0 lb, freq. = 0.333 cpm
    - Perform about 10 cycles to ensure a stable hysteresis loop
    - Scope: X/Y plot, Y = TC_CONTROL, X = Axial Strain 1
  - Copy data to Excel file (TC_DATA_MATLAB.xlsx)
  - Run MATLAB code (ThermalStrainFourier.m – also need Fseries.m and Fseriesval.m to be present in the folder)
  - Copy parameters into Calculation Editor (must be in Configuration mode)

- Check the accuracy of the fit (file: **thermal_fit_check.tst**)
  - **Temp FDBK** control mode, freq. = 0.333 cpm, ramp waveform
  - **MechanicalStrain** control, setpoint = 0 in/in, amp. = 0 lb, freq. = 0.333 cpm
  - Run for 1-2 cycles and examine the resulting forces
  - Calculate upper/lower limits of allowable force
  - If necessary, make adjustments and repeat thermal strain fit

- Start test
  - **Set interlocks**
    - **Force: determined by test loading conditions (usually upper = 12,000 lb, lower = -6,000 lb is good)**
    - **Displacement: upper = 0.35", lower = 0.15"**
    - **Strain: determined by test loading conditions (usually upper = 1.3%, lower = -1.3% is good)**
  - Open Multipurpose Elite and edit test procedure (file: **MechStr _OP_TMF _2**)
    - Set **Tmin**, **Tmax**, **MechStrMin**, **MechStrMax**
    - Check other variables, make sure the desired waveform is correct
  - Create new test run/specimen
  - Hit Run button
  - Scope: X/Y plot, Y1 = Axial Force, Y2 = TC_CONTROL, with X1 and X2 = Axial MechanicalStrain

Shut-Down Procedure (After Test Completion)

- Stop the procedure (unlock) in Multipurpose Elite
- Export the test data
- Set temperature back to room temperature (file: **temp_set.tst**)
    - **Temp FDBK** control mode, ramp to 0 in 90 seconds
    - **Force** control, ramp to 0 lb in 90 seconds
      (if specimen has fractured – use **CLC Axial** control mode with current displacement)
- Turn off induction heater and wait for specimen to cool
- **Set control mode to CLC Axial**
- **Set interlocks**
    - **Force: upper = 500 lb, lower = -500 lb**
    - **Displacement: upper = 0.75”, lower = 0.1”**
- Remove extensometer
- If the hydraulics are off, turn HPU and HSM controls to low, then to high
    - May need to change or override certain interlocks
- Turn off pressure to lower grip (close pressure knob, then open release knob)
- Loosen lower grip by hand
- Unlock upper grip and raise it as much as necessary
- Lock upper grip
- Turn off pressure to upper grip
- Loosen upper grip by hand
- Remove specimen through the coil
- Remove adapters from the collets
- Turn HPU and HSM controls off to turn off the machine
- Turn off water to grips and induction heater
- Turn off the main pump if no other tests are running in the lab

APPENDIX D

TEMPERATURE-DEPENDENT MODULUS DATA

Table D.1 contains the modulus of each specimen used for testing that was measured at room temperature and within the range of test temperatures. The data is shown graphically in Figure D.1, where it is also compared to published data for PWA 1484 [103]. The experimentally measured moduli match up well to the published values, indicating that strain, force, and temperature measurement and control were all accurate during TMF testing.

Table D.1: Temperature-Dependent Modulus Data for All Specimens

	Modulus at Temperature (GPa)						
Specimen	**20°C**	**427°C**	**550°C**	**732°C**	**800°C**	**1038°C**	**1050°C**
5111AA-02-1	133.51	-	-	-	102.18	-	-
5111AA-03-1	126.66	112.30	107.66	97.18	94.10	75.79	74.65
5111AA-03-2	123.07	-	-	-	96.31	-	-
5111AA-04-2	130.01	-	-	-	98.53	-	-
5111AA-06-1	130.39	-	-	-	93.36	-	-
5111AA-06-2	129.93	114.73	110.29	-	97.25	-	77.86
5111AA-07-1	132.49	118.58	113.03	-	98.85	-	78.31
5111AA-08-1	130.94	-	109.88	-	96.25	-	74.52
5111AA-08-2	136.39	-	-	-	97.81	-	-
5111AA-09-2	135.70	-	-	-	99.17	-	-

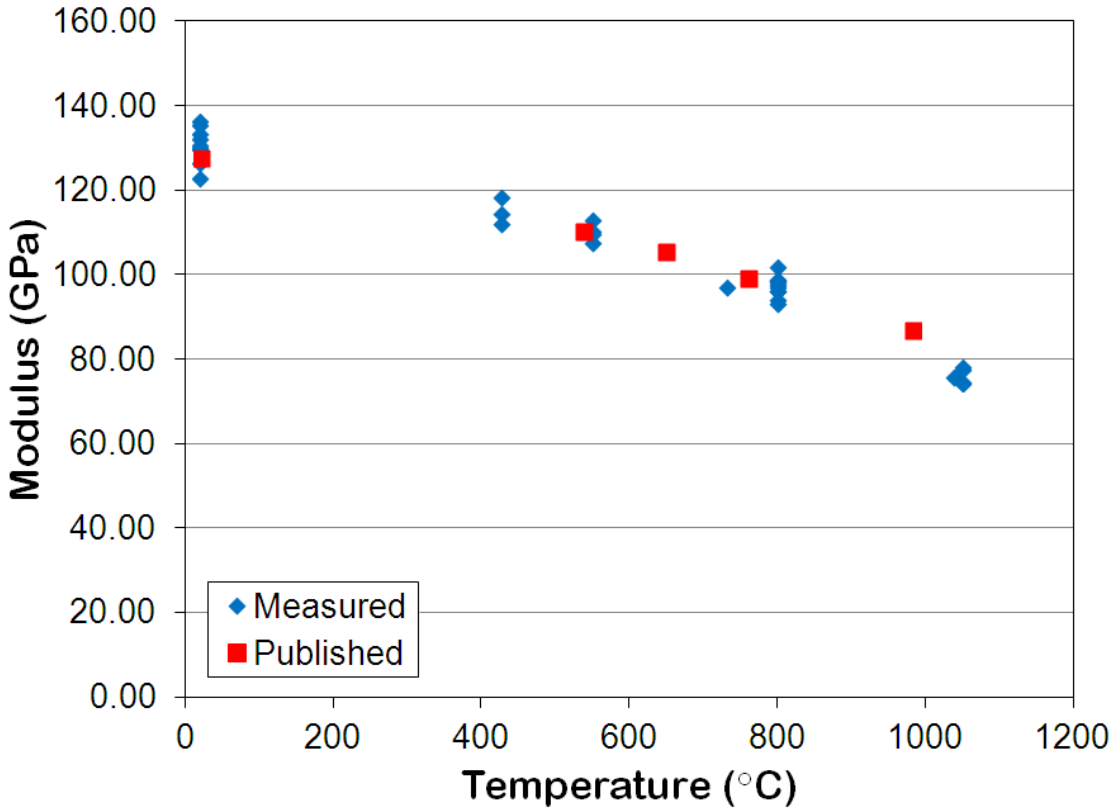

Figure D.1: Measured Modulus as a Function of Temperature for All Specimens, Compared to Published Data

REFERENCES

[1] R.C. Reed, *The Superalloys: Fundamentals and Applications*. 2008, Cambridge: Cambridge University Press.

[2] N.K. Arakere and G. Swanson, *Effect of Crystal Orientation on Fatigue Failure of Single Crystal Nickel Base Turbine Blade Superalloys.* Journal of Engineering for Gas Turbines and Power, 2002. **124**(1): p. 161-176.

[3] M.I. Wood, D. Raynor, and R.M. Cotgrove, *Thermomechanical Fatigue of Coated Superalloys*, in *Life Assessment of Hot Section Gas Turbine Components*, R. Townsend et al., Editor. 2000, The Institute of Materials: London. p. 193-207.

[4] Y. Tamarin, *Protective Coatings for Turbine Blades*. 2002, Materials Park, Ohio: ASM International.

[5] Y.A. Tamarin, V.G. Sundyrin, and N.G. Bychkov, *Thermo-Mechanical Fatigue Tests of Coatings for Turbine Blades*, in *High Temperature Surface Engineering*, J. Nicholls and D. Rickerby, Editors. 2000, The Institute of Materials: London. p. 157-169.

[6] N.K. Arakere, *High-Temperature Fatigue Properties of Single Crystal Superalloys in Air and Hydrogen.* Journal of Engineering for Gas Turbines and Power, 2004. **126**(3): p. 590-603.

[7] R.J. Morrissey, R. John, and W. John Porter III, *Fatigue Variability of a Single Crystal Superalloy at Elevated Temperature.* International Journal of Fatigue, 2009. **31**(11-12): p. 1758-1763.

[8] R. Nutzel, E. Affeldt, and M. Goken, *Damage Evolution During Thermo-Mechanical Fatigue of a Coated Monocrystalline Nickel-Base Superalloy.* International Journal of Fatigue, 2008. **30**(2): p. 313-317.

[9] P.K. Wright, M. Jain, and D. Cameron. *High Cycle Fatigue in a Single Crystal Superalloy: Time Dependence at Elevated Temperature*. in *Superalloys 2004*. 2004. Warrendale, PA: The Minerals, Metals and Materials Society.

[10] R.J. Morrissey and P.J. Golden, *Fatigue Strength of a Single Crystal in the Gigacycle Regime.* International Journal of Fatigue, 2007. **29**(9-11): p. 2079-2084.

[11] J.A. Nychka, D.R. Clarke, and G.H. Meier, *Spallation and Transient Oxide Growth on PWA 1484 Superalloy.* Materials Science and Engineering A, 2008. **490**(1-2): p. 359-368.

[12] C.J. Pierce, A.N. Palazotto, and A.H. Rosenberger, *Creep and Fatigue Interaction in the PWA1484 Single Crystal Nickel-Base Alloy.* Materials Science and Engineering A, 2010. **527**(29-30): p. 7484-7489.

[13] L. Li and R.A. Overfelt, *Influence of Directional Solidification Variables on the Cellular and Primary Dendrite Arm Spacings of PWA1484.* Journal of Materials Science, 2002. **37**(16): p. 3521-3532.

[14] R.L. Amaro, *Thermomechanical Fatigue Crack Formation in a Single Crystal Ni-Base Superalloy*, in *George W. Woodruff School of Mechanical Engineering*. 2010, Georgia Institute of Technology: Atlanta, GA.

[15] R.L. Amaro, S.D. Antolovich, R.W. Neu, P. Fernandez-Zelaia, and W. Hardin, *Thermomechanical Fatigue and Bithermal-Thermomechanical Fatigue of a Nickel-Base Single Crystal Superalloy.* International Journal of Fatigue, 2012. **42**: p. 165-171.

[16] R.L. Amaro, S.D. Antolovich, and R.W. Neu, *Mechanism-Based Life Model for Out-of-Phase Thermomechanical Fatigue in Single Crystal Ni-Base Superalloys.* Fatigue and Fracture of Engineering Materials and Structures, 2012. **35**(7): p. 658-671.

[17] S.D. Antolovich, R.L. Amaro, R.W. Neu, and A. Staroselsky, *On the Development of Physically Based Life Prediction Models in the Thermo Mechanical Fatigue of Ni-Base Superalloys.* Key Engineering Materials, 2011. **465**: p. 47-54.

[18] R.L. Amaro, S.D. Antolovich, R.W. Neu, and A. Staroselsky, *On Thermo-Mechanical Fatigue in Single Crystal Ni-Base Superalloys.* Procedia Engineering, 2010. **2**(1): p. 815-824.

[19] R.L. Amaro, S.D. Antolovich, R.W. Neu, and A. Staroselsky. *Physics-Based Modeling of Thermo-Mechanical Fatigue in PWA 1484*. in *Superalloys 2012*. 2012. Seven Springs, PA: The Minerals, Metals & Materials Society.

[20] J.A. Bannantine, J.J. Comer, and J.L. Handrock, *Fundamentals of Metal Fatigue Analysis*. 1990, Englewood Cliffs, N.J.: Prentice Hall.

[21] O.H. Basquin, *The Exponential Law of Endurance Tests.* American Society of Materials and Testing Proceedings, 1910. **10**: p. 625-630.

[22] L.F. Coffin, Jr., *A Study of the Effects of Cyclic Thermal Stresses on a Ductile Metal.* Transactions of ASME, 1954. **76**: p. 931-950.

[23] S.S. Manson, *Behavior of Materials under Conditions of Thermal Stress,* in *Heat Transfer Symposium*. 1953: University of Michigan Engineering Research Institute. p. 9-75.

[24] J.M. Gere and B.J. Goodno, *Mechanics of Materials*. 8th ed. 2013, Stamford: Cengage Learning.

[25] M. Ramesh, H.J. Leber, M. Diener, and R. Spolenak, *Conducting Thermomechanical Fatigue Test in Air at Light Water Reactor Relevant Temperature Intervals.* Journal of Nuclear Materials, 2011. **415**(1): p. 23-30.

[26] J. Gayda, T.P. Gabb, and R.V. Miner, *Isothermal and Bithermal Thermomechanical Fatigue Behavior of a NiCoCrAlY-Coated Single Crystal Superalloy*. 1988, National Aeronautics and Space Administration: Washington, DC.

[27] G.R. Halford, M.A. McGaw, R.C. Bill, and P.D. Fanti, *Bithermal Fatigue: A Link Between Isothermal and Thermomechanical Fatigue,* in *ASTM Special Technical Publication 942, Low Cycle Fatigue, a Symposium, September 30, 1987 - September 30, 1987*. 1987, ASTM: Bolton Landing, NY, USA. p. 625-637.

[28] M.J. Verrilli, *Bithermal Fatigue of a Nickel-Base Superalloy Single Crystal,* in *Technical Memorandum 100855*. 1988, National Aeronautics and Space Administration: Washington, D.C.

[29] Federal Aviation Administration, *Airplane Flying Handbook*. 2004, U.S. Dept. of Transportation, Federal Aviation Administration, Flight Standards Service, Airman Testing Standards Branch: Washington, DC.

[30] C.T. Sims, N.S. Stoloff, and W.C. Hagel, *Superalloys II : High-Temperature Materials for Aerospace and Industrial Power*. 1987, New York: John Wiley & Sons.

[31] M. McLean, *Directionally Solidified Materials for High Temperature Service*. 1983, London: The Metals Society.

[32] N.A. Cumpsty, *Jet Propulsion: A Simple Guide to the Aerodynamic and Thermodynamic Design and Performance of Jet Engines*. 1997, Cambridge: Cambridge University Press.

[33] W. Betteridge and S.W.K. Shaw, *Development of Superalloys.* Materials Science and Technology, 1987. **3**: p. 682-694.

[34] Rolls-Royce, *The Jet Engine*. 4th ed. 1992, Derby, UK: Rolls-Royce.

[35] M. Durand-Charre, *The Microstructure of Superalloys*. 1997, Amsterdam, The Netherlands: Gordon and Breach Science Publishers.

[36] P. Beardmore, R.G. Davies, and T.L. Johnston, *On the Temperature Dependence of the Flow Stress of Nickel-Base Alloys.* Transactions of the Metallurgical Society of AIME, 1969. **245**(7): p. 1537-1545.

[37] B.J. Piearcey, B.H. Kear, and R.W. Smashey, *Correlation of Structure with Properties in a Directionally Solidified Nickel-Base Superalloy.* Transactions of the American Society for Metals, 1967. **60**(4): p. 634-645.

[38] R.G. Davies and N.S. Stoloff, *On the Yield Stress of Aged Ni-Al Alloys.* Transactions of the Metallurgical Society of AIME, 1965. **233**(4): p. 714-719.

[39] A.D. Cetel and D.N. Duhl, *Second Generation Nickel-Base Single Crystal Superalloy*, in *Superalloys 1988*, S. Reichman, D.N. Duhl, G. Maurer, S. Antolovich, and C. Lund, Editors. 1988, The Metallurgical Society: Warrendale, PA. p. 235-244.

[40] M.H. Li, X.F. Sun, J.G. Li, Z.Y. Zhang, T. Jin, H.R. Guan, and Z.Q. Hu, *Oxidation Behavior of a Single-Crystal Ni-Base Superalloy in Air. I: At 800 and 900C.* Oxidation of Metals, 2003. **59**(5-6): p. 591-605.

[41] Z. Yizhou, *Formation of Stray Grains during Directional Solidification of a Nickel-Based Superalloy.* Scripta Materialia, 2011. **65**(4): p. 281-284.

[42] A. Pineau and S.D. Antolovich, *High Temperature Fatigue of Nickel-Base Superalloys - A Review with Special Emphasis on Deformation Modes and Oxidation.* Engineering Failure Analysis, 2009. **16**(8): p. 2668-2697.

[43] M.P. Jackson and R.C. Reed, *Heat Treatment of UDIMET 720Li: The Effect of Microstructure on Properties.* Materials Science & Engineering A (Structural Materials: Properties, Microstructure and Processing), 1999. **A259**(1): p. 85-97.

[44] T. Murakumo, T. Kobayashi, Y. Koizumi, and H. Harada, *Creep Behaviour of Ni-Base Single-Crystal Superalloys with Various Gamma Prime Volume Fraction.* Acta Materialia, 2004. **52**(12): p. 3737-3744.

[45] A. Choudhury, *Vacuum Metallurgy*. 1990, Materials Park, OH: ASM International.

[46] F. Sczerzenie and G.E. Maurer, *Developments in Disc Materials.* Materials Science and Technology, 1987. **3**: p. 733-742.

[47] D. Furrer and H. Fecht, *Ni-Based Superalloys for Turbine Discs.* Journal of Metals, 1999. **51**(1): p. 14-17.

[48] A. Sengupta, S.K. Putatunda, L. Bartosiewicz, J. Hangas, P.J. Nallos, M. Peputapeck, and F.E. Alberts, *Tensile Behavior of a New Single-Crystal Nickel-Based Superalloy (CMSX-4) at Room and Elevated Temperatures.* Journal of Materials Engineering and Performance, 1994. **3**(1): p. 73-81.

[49] R.C. Reed, N. Matan, D.C. Cox, M.A. Rist, and C.M.F. Rae, *Creep of CMSX-4 Superalloy Single Crystals: Effects of Rafting at High Temperature.* Acta Materialia, 1999. **47**(12): p. 3367-3381.

[50] D.M. Shah, S. Vega, W. Woodard, and A.D. Cetel. *Primary Creep in Nickel-Base Superalloys*. in *Superalloys 2004*. 2004. Warrendale, PA: The Minerals, Metals and Materials Society.

[51] N. Matan, D.C. Cox, P. Carter, M.A. Rist, C.M.F. Rae, and R.C. Reed, *Creep of CMSX-4 Superalloy Single Crystals: Effects of Misorientation and Temperature.* Acta Materialia, 1999. **47**(5): p. 1549-1563.

[52] T.P. Gabb, S.L. Draper, D.R. Hull, R.A. Mackay, and M.V. Nathal, *Role of Interfacial Dislocation Networks in High Temperature Creep of Superalloys.* Materials Science and Engineering A, 1989. **A118**(1-2): p. 59-69.

[53] N. Matan, D.C. Cox, C.M.F. Rae, and R.C. Reed, *On the Kinetics of Rafting in CMSX-4 Superalloy Single Crystals.* Acta Materialia, 1999. **47**(7): p. 2031-2045.

[54] J.Y. Buffiere and M. Ignat, *A Dislocation Based Criterion for the Raft Formation in Nickel-Based Superalloy Single Crystals.* Acta Metallurgica et Materialia, 1995. **43**(5): p. 1791-1797.

[55] M. Veron, Y. Brechet, and F. Louchet, *Strain Induced Directional Coarsening in Ni-Base Superalloys.* Scripta Materialia, 1996. **34**(12): p. 1883-1886.

[56] S. Suresh, *Fatigue of Materials*. 2nd ed. 1998, Cambridge: Cambridge University Press.

[57] P. Lukas and L. Kunz, *Cyclic Slip Localisation and Fatigue Crack Initiation in FCC Single Crystals.* Materials Science & Engineering A (Structural Materials: Properties, Microstructure and Processing), 2001. **A314**: p. 75-80.

[58] V. Brien and B. Decamps, *Low Cycle Fatigue of a Nickel Based Superalloy at High Temperature: Deformation Microstructures.* Materials Science & Engineering A (Structural Materials: Properties, Microstructure and Processing), 2001. **A316**(1-2): p. 18-31.

[59] R.P. Dalal, C.R. Thomas, and L.E. Dardi, *The Effect of Crystallographic Orientation on the Physical and Mechanical Properties of an Investment Cast Single Crystal Nickel-Base Superalloy*, in *Superalloys 1984*, R.H. Bricknell, W.B. Kent, M. Gell, C.S. Kortovich, and J.F. Radavich, Editors. 1984, The Metallurgical Society: Warrendale, PA. p. 185-197.

[60] D.W. MacLachlan and D.M. Knowles, *Fatigue Behaviour and Life of Two Single Crystal Superalloys.* Fatigue & Fracture of Engineering Materials & Structures, 2001. **24**(8): p. 503-521.

[61] C.S. Giggins and F.S. Pettit, *Oxidation of Ni-Cr-Al Alloys Between 1000 and 1200C.* Journal of the Electrochemical Society, 1971. **118**(11): p. 1782-1790.

[62] A. Akhtar, M.S. Hook, and R.C. Reed, *On the Oxidation of the Third-Generation Single-Crystal Superalloy CMSX-10.* Metallurgical and Materials Transactions A (Physical Metallurgy and Materials Science), 2005. **36A**(11): p. 3001-3017.

[63] P.K. Wright, *Oxidation-Fatigue Interactions in a Single-Crystal Superalloy,* in *ASTM Special Technical Publication 942, Low Cycle Fatigue, a Symposium, September 30, 1987 - September 30, 1987*. 1987, ASTM: Bolton Landing, NY, USA. p. 558-575.

[64] A.P. Gordon, M.D. Trexler, R.W. Neu, T.J. Sanders, Jr., and D.L. McDowell, *Corrosion Kinetics of a Directionally Solidified Ni-Base Superalloy.* Acta Materialia, 2007. **55**(10): p. 3375-3385.

[65] D.K. Das, V. Singh, and S.V. Joshi, *High Temperature Oxidation Behaviour of Directionally Solidified Nickel Base Superalloy CM - 247LC.* Materials Science and Technology, 2003. **19**(6): p. 695-708.

[66] K. Bouhanek, D. Oquab, and B. Pieraggi. *High Temperature Oxidation of Single-Crystal Ni-Base Superalloys*. in *High Temperature Corrosion and Protection of Materials 4. 4th International Symposium, 20-24 May 1996*. 1997. Switzerland: Trans Tech Publications.

[67] U. Krupp and H.J. Christ, *Selective Oxidation and Internal Nitridation During High-Temperature Exposure of Single-Crystalline Nickel-Base Superalloys.* Metallurgical and Materials Transactions A (Physical Metallurgy and Materials Science), 2000. **31A**(1): p. 47-56.

[68] L.G. Zhao, N.P. O'Dowd, and E.P. Busso, *A Coupled Kinetic-Constitutive Approach to the Study of High Temperature Crack Initiation in Single Crystal Nickel-Base Superalloys.* Journal of the Mechanics and Physics of Solids, 2006. **54**(2): p. 288-309.

[69] S. Dumoulin, E.P. Busso, N.P. O'Dowd, and D. Allen, *A Multiscale Approach for Coupled Phenomena in FCC Materials at High Temperatures.* Philosophical Magazine, 2003. **83**(31-34): p. 3895-3916.

[70] J.E. Heine, J.R. Warren, and B.A. Cowles, *Thermomechanical Fatigue of Coated Blade Materials*, in *Final Report, WRDC-TR-89-4027*. 1989, Wright Research and Development Center.

[71] G.W. Goward, D.H. Boone, and C.S. Giggins, *Formation and Degradation Mechanisms of Aluminide Coatings on Nickel-Base Superalloys.* American Society of Metals - Transactions, 1967. **60**(2): p. 228-241.

[72] H.M. Tawancy, N.M. Abbas, and T.N. Rhys-Jones, *Role of Platinum in Aluminide Coatings.* Surface Coatings Technology, 1991. **49**: p. 1-7.

[73] J.R. Davis, *Handbook of Thermal Spray Technology*. 2004, Materials Park, Ohio: ASM International.

[74] D.H. Boone. *Physical Vapour Deposition Processes*. in *Protective Coating Systems for High-Temperature Gas Turbine Components, 13-14 Nov. 1984*. 1986. UK.

[75] A.R. Nicholl, H. Gruner, G. Wuest, and S. Keller, *Future Developments in Plasma Spray Coating.* Materials Science and Technology, 1986. **2**: p. 214-219.

[76] A.R. Nicholl and G. Wahl, *Oxidation and High Temperature Corrosion Behavior of Modified MCrAlY Cast Materials*, in *Superalloys 1984*, R.H. Bricknell, W.B. Kent, M. Gell, C.S. Kortovich, and J.F. Radavich, Editors. 1984, The Metallurgical Society of AIME: Warrandale, PA. p. 805-814.

[77] B.A. Pint, I.G. Wright, W.Y. Lee, Y. Zhang, K. Pruessner, and K.B. Alexander, *Substrate and Bond Coat Compositions: Factors Affecting Alumina Scale Adhesion.* Materials Science & Engineering A (Structural Materials: Properties, Microstructure and Processing), 1998. **A245**(2): p. 201-211.

[78] J.S. Wang and A.G. Evans, *Effects of Strain Cycling on Buckling, Cracking and Spalling of a Thermally Grown Alumina on a Nickel-Based Bond Coat.* Acta Materialia, 1999. **47**(2): p. 699-710.

[79] J.R. Nicholls, *Advances in Coating Design for High-Performance Gas Turbines.* MRS Bulletin, 2003. **28**(9): p. 659-670.

[80] J.H. Wood and E. Goldman, *Protective Coatings*, in *Superalloys II*, C.T. Sims, S.N. S., and H.W. C., Editors. 1987, Wiley: New York. p. 359-384.

[81] E.S. Huron and S.D. Antolovich, *Observations of High Temperature Tensile and Cyclic Deformation in a Directionally Solidified Nickel-Base Superalloy*, in *Phase Boundary Effects on Deformation*, K.N. Subramanian and M.A. Imam, Editors. 1986, The Metallurgical Society of AIME: Warrendale, PA. p. 185-203.

[82] D. Fournier and A. Pineau, *Low Cycle Fatigue Behavior of Inconel 718 at 298K and 823K.* Metallurgical Transactions A (Physical Metallurgy and Materials Science), 1977. **8A**(7): p. 1095-1105.

[83] H.F. Merrick, *The Low Cycle Fatigue of Three Wrought Nickel-Base Alloys.* Metallurgical Transactions A (Physical Metallurgy and Materials Science), 1974. **5**(4): p. 891-897.

[84] B.A. Lerch, N. Jayaraman, and S.D. Antolovich, *A Study of Fatigue Damage Mechanisms in Waspaloy from 25 to 800C.* Material Science and Engineering, 1984. **66**(2): p. 151-166.

[85] B. Buchholz, H. Harders, and U. Gampe, *Thermo-Mechanical and Low Cycle Fatigue Behaviour of a Nickel-Base Superalloy at Elevated Temperatures.* Materials at High Temperatures, 2013. **30**(1): p. 43-48.

[86] R.V. Miner, J. Gayda, and R.D. Maier, *Fatigue and Creep-Fatigue Deformation of Several NickelBbase Superalloys at 650C.* Metallurgical Transactions A (Physical Metallurgy and Materials Science), 1982. **13A**(10): p. 1755-1765.

[87] R.E. Stoltz and A.G. Pineau, *Dislocation-Precipitate Interaction and Cyclic Stress-Strain Behavior of a Gamma Prime Strengthened Superalloy.* Material Science and Engineering, 1978. **34**(3): p. 275-284.

[88] S.D. Antolovich, S. Liu, and R. Baur, *Low Cycle Fatigue Behavior of Rene 80 at Elevated Temperature.* Metallurgical Transactions A (Physical Metallurgy and Materials Science), 1981. **12A**(3): p. 473-481.

[89] W.W. Milligan and S.D. Antolovich, *Yielding and Deformation Behavior of the Single Crystal Superalloy PWA 1480.* Metallurgical Transactions A (Physical Metallurgy and Materials Science), 1987. **18A**(1): p. 85-95.

[90] N.K. Arakere and J. Moroso, *Fatigue Failure in High-Temperature Single Crystal Superalloy Turbine Blades.* High Temperature Materials and Processes, 2001. **20**(2): p. 117-136.

[91] X. Li and J. Smith, *Development of an Anisotropic Constitutive Model for Single-Crystal Superalloy for Combined Fatigue and Creep Loading.* International Journal of Mechanical Sciences, 1998. **40**(10): p. 937-948.

[92] S.E. Harvey, P.G. Marsh, and W.W. Gerberich, *Atomic Force Microscopy and Modeling of Fatigue Crack Initiation in Metals.* Acta Metallurgica et Materialia, 1994. **42**(10): p. 3493-3502.

[93] B.S. Boursier, *Evaluation of Damage Mechanisms in the Nickel Base Superalloy Rene 80 Under Low Cycle Fatigue in the Temperature Range 75F-1400F*, in *Department of Materials Science and Metallurgical Engineering*. 1981, University of Cincinnati: Cincinnati, OH.

[94] M.S. Loveday, V. Bicego, P. Hahner, H. Klingelhoffer, H.J. Kuhn, and B. Roebuck, *Analysis of a European TMF Inter-Comparison Exercise.* International Journal of Fatigue, 2008. **30**(2): p. 382-390.

[95] S. Pahlavanyali, A. Rayment, B. Roebuck, G. Drew, and C.M.F. Rae, *Thermo-Mechanical Fatigue Testing of Superalloys Using Miniature Specimens.* International Journal of Fatigue, 2008. **30**(2): p. 397-403.

[96] T. Beck and K. Rau, *Temperature Measurement and Control Methods in TMF Testing - A Comparison and Evaluation.* International Journal of Fatigue, 2008. **30**(2): p. 226-233.

[97] H.J. Kuhn, O. Kahlcke, and S. Brookes, *A Practicable Nominal Temperature Tolerance for TMF-Tests.* International Journal of Fatigue, 2008. **30**(2): p. 277-285.

[98] T. Brendel, E. Affeldt, J. Hammer, and C. Rummel, *Temperature Gradients in TMF Specimens. Measurement and Influence on TMF Life.* International Journal of Fatigue, 2008. **30**(2): p. 234-240.

[99] H.C.M. Andersson and E. Sjostrom, *Thermal Gradients in Round TMF Specimens.* International Journal of Fatigue, 2008. **30**(2): p. 391-396.

[100] S. Pahlavanyali, G. Drew, A. Rayment, and C.M.F. Rae, *Thermo-Mechanical Fatigue of a Polycrystalline Superalloy: The Effect of Phase Angle on TMF Life and Failure.* International Journal of Fatigue, 2008. **30**(2): p. 330-338.

[101] ASTM Standard E2368, *Standard Practice for Strain Controlled Thermomechanical Fatigue Testing*. 2010, ASTM International: West Conshohocken, PA.

[102] MTS Systems Corporation, *Series 646 Hydraulic Collet Grips: Product Information*. 2009.

[103] Nickel Development Institute, *High-Temperature High-Strength Nickel Base Alloys: 1995 Supplement*. 1995: Ontario, Canada.

[104] N. Kumar, S.C. Mondal, D.K. Mandal, and S.K. Acharyaa, *Optimum Autofrettage Pressure and Shrink-Fit Combination for Minimum Stress in Multilayer Pressure Vessel.* International Journal of Engineering Science & Technology, 2011. **3**(5): p. 4020-4030.

[105] D.E. Lempidaki, E.P. Busso, and N.P. O'Dowd. *Application of Non-Contact Strain Measurement Techniques to a Single Crystal Alloy at Elevated Temperatures*. in *11th International Conference on Fracture*. 2005. Turin, Italy.

[106] A. Ozel, S. Temiz, M.D. Aydin, and S. Sadri, *Stress Analysis of Shrink-Fitted Joints for Various Fit Forms Via Finite Element Method.* Materials & Design, 2005. **26**(4): p. 281-289.

[107] R.G. Budynas, J.K. Nisbett, and J.E. Shigley, *Shigley's Mechanical Engineering Design*. 2011, New York: McGraw-Hill.

[108] M.J. Moran and H.N. Shapiro, *Fundamentals of Engineering Thermodynamics*. 2008, Hoboken (New Jersey): John Wiley & Sons.